5-2020

Tuning Photocurrent Responses from Photosystem I via Microenvironment Alterations: Effect of Plasmonic Electric Fields and Membrane Confinements

Ravi Pamu
University of Tennessee, rpamu@vols.utk.edu

To the Graduate Council:

I am submitting herewith a dissertation written by Ravi Pamu entitled "Tuning Photocurrent Responses from Photosystem I via Microenvironment Alterations: Effect of Plasmonic Electric Fields and Membrane Confinements." I have examined the final electronic copy of this dissertation for form and content and recommend that it be accepted in partial fulfillment of the requirements for the degree of Doctor of Philosophy, with a major in Mechanical Engineering.

Dibyendu Mukherjee, Major Professor

We have read this dissertation and recommend its acceptance:

Bamin Khomami, Andy Sarles, Benjamin J. Lawrie

Accepted for the Council:

Dixie L. Thompson

Vice Provost and Dean of the Graduate School

(Original signatures are on file with official student records.)

Tuning Photocurrent Responses from Photosystem I via Microenvironment Alterations: Effect of Plasmonic Electric Fields and Membrane Confinements

A Dissertation Presented for the

Doctor of Philosophy

Degree

The University of Tennessee, Knoxville

Ravi Pamu

May 2020

Acknowledgments

There are many people who supported academically and emotionally during my time at UT. I would like to thank my advisor Dr. Dibyendu Mukherjee for his constant support and encouragement. His valuable guidance in research led me to finish the projects mentioned in the dissertation. Moreover, I would like to thank my co-adviser Prof. Bamin Khomami for his precious guidance and critical comments for the betterment of my research.

I also would like to thank Dr. Ramki Kalyanaraman and Dr. Benjamin Lawrie for their support in the collaborative projects. I also thank my committee members for their time and insightful discussion.

I appreciate the assistance provided by V Prasad Sandireddy in Nano-Sphere Lithography for Silver Nanostructures fabrication. I thank Dr. Lawrie Benjamin, Dr. Scott Retterer and other staff at Center for Nanophase Materials Sciences (CNMS) of Oakridge National Laboratory (ORNL) in helping the E-Beam Lithography for nanostructures fabrication and characterization. Special thanks to my friend and colleague Tyler Bennett, for great technical and emotional support throughout the journey. I enjoyed deep conversations with him. I am grateful to have wonderful lab mates Hanieh Niroomand and Erick Ribeiro for their valuable friendship, commiseration, and technical assistance. I also thank the staff of MABE department for their services.

Special thanks to Dr. John Dunlap (Advanced Microscopy and Imaging Center at the University of Tennessee, Knoville) and Dr. Edward wright (Bioanalytical Resources Facility at the University of Tennessee, Knoxville) for their scientific and technical assistance.

Finally, I am thankful to the financial support provided by the University of Tennessee, Sustainable Energy Education and Research Center (SEERC) and a DoE-UT Battelle grant.

Abstract

Robust photoelectrochemical activities of PSI make it an ideal candidate for bio-hybrid photovoltaic and optoelectronic devices. This dissertation focuses on role of microenvironment alterations around PSI in tuning its photocurrent responses when assembled with tailored plasmonic metal nanostructures and biomimetic lipid interfaces. To this end, a series of systematic studies aimed at tuning the plasmon enhanced photocurrent responses from PSI assembled with gold and silver metal nanopatterns tailored for different plasmonic absorption wavelengths. The experimental observation of plasmon-induced photocurrent enhancements in PSI is investigated using Fischer patterns of silver nanopyramids (Ag-NPs) wherein the resonant peaks were tuned to match the PSI absorption peaks at ~450 and ~680 nm. A conservative estimate for the enhancement factors were found to be ~ 5.8 – 6.5 when compared to PSI on planar Ag substrate assemblies. Furthermore, spatially localized and spectrally resolved wavelength-dependent plasmon-enhanced photocurrents from PSI are investigated by specifically assembling the protein units in regions around highly ordered Au (AuND) and Ag (AgND) nano-discs where the dipolar plasmon resonance modes from the respective NDs are tuned to the wavelengths of ~680 nm and ~560 nm, respectively. Specifically, we report plasmon-enhancement factors of ~6.8 and ~17.5 for the PSI photocurrents recorded under the excitation wavelengths of ~680 nm and ~565 nm respectively as compared to PSI assembled on planar ITO substrates. The results indicate: 1) direct correlations between the photocurrent enhancement spectra from the PSI assemblies and the plasmonic resonance modes for the respective nanopatterned substrates, and 2) broadband photocurrent enhancements due to plasmon-coupled photoactivation in the otherwise blind chlorophyll regions of the native PSI absorption spectra.

In our continuing efforts to investigate the alterations in the photoexcitation/dissipation pathways in PSI due to characteristic changes in their optical and structural properties under biomimetic membrane confinements, , the PSI complexes are reconstituted in synthetic lipid membranes of 1,2-diphytanoyl-sn-glycero-3-phospho-(1′-rac-glycerol) (DPhPG) and 1,2-diphytanoyl-sn-glycero-3-phosphocholine (DPhPC). The results presented here from absorption, fluorescence and circular dichroism indicate unique changes around the carotenoid/chlorophyll spectral bands leading to attainment of broad-band light harvesting via enhanced absorption in the otherwise non-absorptive green region (500 – 580 nm) of unconfined PSI absorption spectra.

Table of Contents

List of Figures

Chapter 1

Introduction

Total world energy consumption is around 18 TW-year as estimated by International Energy Agency in 2013 and it is expected to grow every year. Out of which, 80% of the energy is coming from fossil fuel resources such as oil, gas, coal. A meager share of ~17% is coming from renewable energy resources. Dependence on fossil fuels is unsustainable due to limited resources, and the consequential environmental damage. The burning of fossil fuels releases CO_2 that pollutes the air and contribute to the global warming greenhouse gases. Our oil and coal reserves will fulfill the energy needs for another three to four generations at the great cost of environmental damage[2]. On the backdrop of this, there are continuous efforts to increase the utilization of renewable energy resources such as solar, wind. In fact, staggering amount of solar energy (23000 TW every year) reaches the earth [2]. It is 30 times larger than total coal reserves, 100 times larger than oil reserves and 1300 times more than the world energy consumption every year. To convert this vast amount of natural solar energy resources into electricity, photovoltaic technology developed with semiconductor materials such as silicon solar panels has been actively pursued [3]. However, nature has evolved to to develop its own robust photosynthesis mechanism that taps into the vast resources of solar energy by achieving highly efficient (nearly 100% quantum efficient) solar to photo-electrochemical energy conversions in plant leaves, algae, cyanobacteria, etc. Central to this photosynthesis process are the four protein complexes that work in coordination to convert the solar energy into chemical energy, out of which two vital transmembrane photosynthetic protein complexes are Photosystem II (PSII) and Photosystem I (PSI) that remain embedded in the thylakoid membrane housing of cyanobacteria and chloroplasts. Specifically, the PSII uses the photon energy from the sun to split water into protons, oxygen and electrons, whereby the PSI facilitates unidirectional transport of the photo-generated electrons across the thylakoid membranes through a series of redox chemical reactions in the Electron Transport Chain (ETC) that forms the backbone of the photo-electrochemical energy conversion process in PSI. These proteins can be extracted out from their natural thylakoid environment using biochemical extraction and purification steps. In recent years, considerable research has been dedicated toward utilizing the exotic biological photo-engines of PSII and PSI for architecting bio-hybrid optoelectronic devices for sustainable hydrogen and electricity production.

However, the first critical step towards the successful fabrication of such bio-hybrid devices require systematic assembly of oriented and functional PSI onto desired biotic-abiotic interfaces via suitable protein scaffoldings that can mimic the natural thylakoid membrane housing. An optimal design of such interfaces should be able to orchestrate optimal photo-excitations and charge transport across the PSI systems via efficient light absorption and minimal electron recombination losses. The focus of this dissertation is to investigate the integration of cyanobacterial PSI as a biological photodiode and an electron pump in biomimetic organic/inorganic interfaces for the rational design of bio-hybrid photo-electrochemical conversion devices that can enable efficient conversion of solar energy into electrical energy and/or solar fuels. Specifically, this dissertation research will unveil the critical role of microenvironment alterations around PSI through physical and electromagnetic confinements in biomimetic synthetic lipid membranes and plasmonic metal nanostructures in tuning the light activated structure-function relations PSI. The results from the studies presented here can pave the path for unprecedented routes for the smart and rational design of future PSI-based bio-hybrid optoelectronic and quantum devices.

To this end, the current chapter provides an overview on photosynthesis, a background on PSI structure and function, and a literature survey of previous works on PSI-based photochemical devices and strategies to enhance their performances.

1.1 Photosynthesis Overview:

Natural oxygenic photosynthetic processes in cyanobacteria, algae and plants constitute the primary driving forces behind the rise of oxygen levels on the aerobic earth in first place. They convert abundant amounts of solar energy into chemical energy with nearly 100% internal quantum efficiency due to evolutionary processes developed over the billions of years[4]. Unlike anaerobic photosynthetic organisms where no oxygen is released due to the cyclic electron flow, the non-cyclic photosynthetic electron chain in oxygenic photosynthesis utilizes sunlight to split water to produce protons and electrons while releasing oxygen as a byproduct[5, 6]. Overall, oxygenic photosynthesis process uses the photon energy from sunlight to convert atmospheric CO_2 and water into usable chemical energy stored in the form of carbohydrates, sugars etc.

$$nCO_2 + nH_2O \xrightarrow{light} n(CH_2O) + nO_2$$

Typically, photosynthesis process involves two stages: 1) light dependent reactions, 2) light independent reactions. It is in the second stage where the CO_2 is reduced to carbohydrates through the Calvin cycle which requires the participation of ATP and NADPH outside the protein housing. However, the light dependent reactions in the first stage are responsible for the generation of ATP and NADPH. The light-induced electron transport chain in PSI transports the electrons generated from the water splitting step all the way up to the terminal step of reducing the $NADP^+$ to NADPH. The overall equation for the light dependent reaction is as follows:

$$2H_2O + 2NADP^+ + 3ADP + 3P_i + light \rightarrow 2NADPH + 2H^+ + 3ATP + O_2$$

The detailed trails for the electron and proton transport pathways are shown in Figure 1.1 as the blue and red dotted paths respectively. The process begins with PSII where the absorbed photon energy is employed to oxidize water into oxygen, protons, and electrons. Here, the proton gradient across ATP synthase produces the ATP at the stromal side of the membrane. On the other hand, the electrons released from the water splitting in PSII travels to PSI unit through a series of biochemical reactions assisted by plastoquinone, cytochrome and luminal protein plastocyanin[7]. When a photon hits the PSI, the excited reaction center P700 initiates a charge separation within the PSI. Mediated by plastocyanin and/or cytochromes, the electrons from the PSII unit are shuttled from the luminal side to the stromal side of the PSI membrane scaffold. The ferredoxin

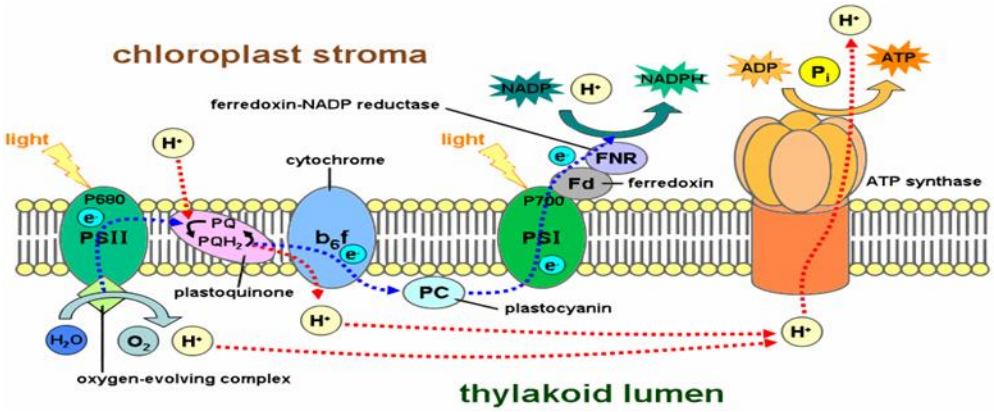

Figure 1.1 Light dependent reactions of oxygenic photosynthesis process comprising photosynthetic reaction center based protein complexes, PSI and PSII along with cytochrome b6f and ATP synthase enzyme that are confined in native environment of thylakoid lipid membrane.[8]

shuttles the electrons from the PSI terminal stromal side while the plastocyanin charge neutralizes the P700 by supplying new electron. The transported electron will be used in reducing the $NADP^+$ to NADPH at the stromal side of the membrane. From an engineering standpoint, here the PSI essentially acts as biological photodiode, enabling light-induced unidirectional electron transport from the luminal side to the stromal side of the PSI unit.

The electron transfer pathway from water splitting to the $NADP^+$ in the oxygenic photosynthesis can be depicted from the perspective of a Z-scheme energy diagram as shown in Figure 1.2. The vertical axis of the energy levels represents the redox potential or reducing capacity of the molecule. The electron easily transfers from top to bottom while the uphill transfer from lower to upper energy state molecules in the diagram requires external energy stimulations[9]. The overall electron transfer is essentially an uphill process that requires light excitations of the reaction centers (RC) P680 and P700 of PSII and PSI, respectively. The RC (P700) in PSI is a special pair of Chlorophyll a (Chla) dimers which act as the primary electron donors in the ETC

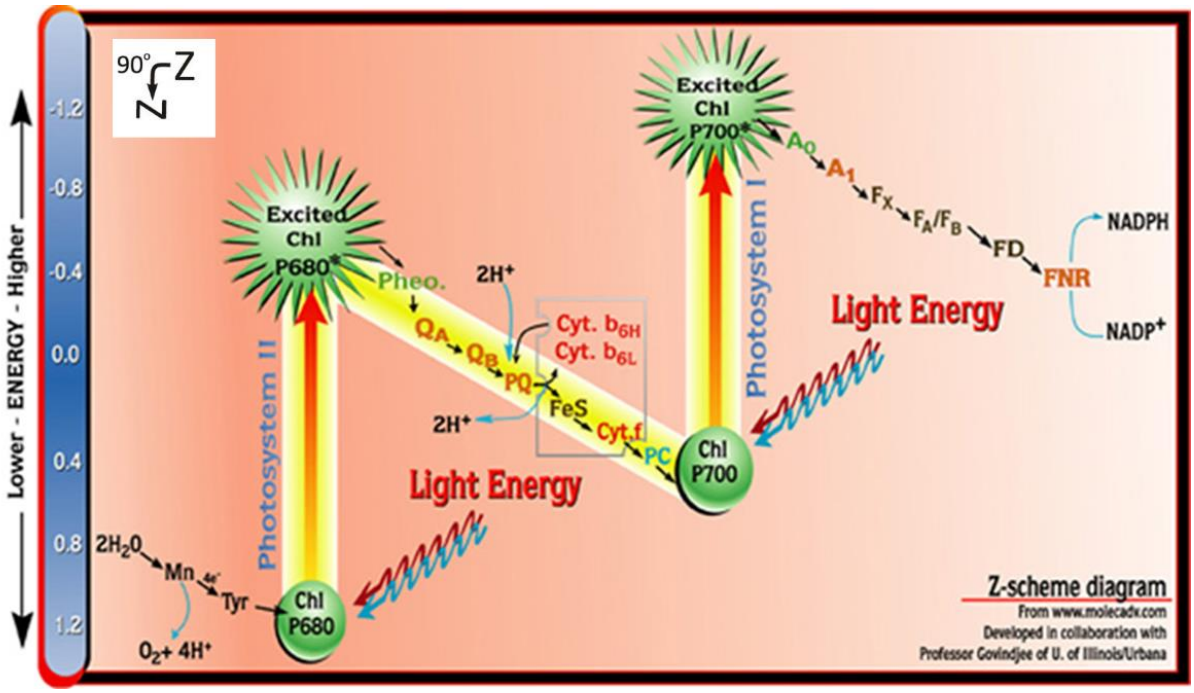

Figure 1.2 Electron transfer pathway from left to right and increasing reducing energy of molecules from bottom to top.[1]

of PSI. The downhill reactions from the excited $P700^*$ to F_A/F_B occurs within the PSI protein complex. The detailed structural information for PSI and the role of its cofactors are provided in the next section.

1.2 PSI Overview:

The PSI is extracted from *Thermosynechococcus Elongatus (T. Elongatus)*, a thermophilic cyanobacterium. The PSI is a supramolecular transmembrane protein unit that exist in a trimeric form. It weighs 1068 kDa with the physical dimensions of 22 nm in diameter and 9 nm thickness (see Figure 1.3) [10]. Detailed 2.5 Å resolution X-ray crystallography studies on the thermophilic cyanobacterial PSI has already revealed the three-dimensional structures of its cofactors [11]. Each PSI monomer contains 12 protein subunits, 96 chlorophylls, 2 phylloquinone, 3 Fe_4S_4 clusters, 22 carotenoids, and 4 lipids. The protein subunits non-covalently bound to other cofactors and function as binding blocks to stabilize all the cofactors and maintain its structural integrity. The 90 chlorophyll molecules and 22 carotenoids act as the light-harvesting antenna system. When a photon hits on the antenna system, the excitation energy funnels to the RC chlorophyll dimer P700 through singlet-singlet energy transfer among neighboring chromophores in the PSI unit[12]. The proposed Forster Resonance Energy Transfer (FRET) for this process is known to be

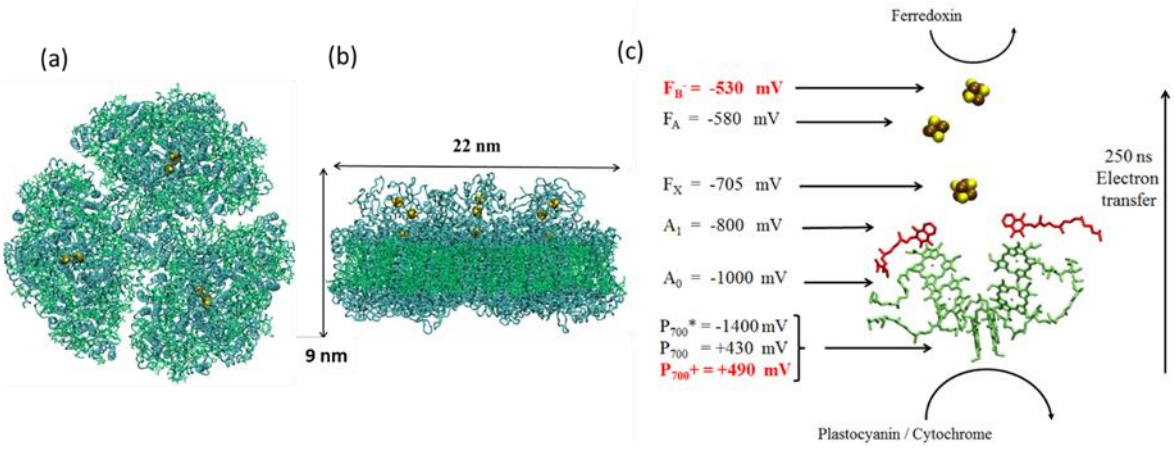

Figure 1.3 (a) Cyanobacterial trimeric PSI in top-view, (b) The trimeric PSI in side-view and its physical dimensions, (c) Electron transport chain existing within PSI with its energy levels.

extremely sensitive to the distance of separation and orientation of the interacting chromophores[13, 14]. This excitation energy transfer (EET) through the chromophore networks initiates the charge separation at P700 which then travels all the way from the excited $P700^*$ to the terminal iron-sulfur clusters (F_A/ F_B/ F_X) mediated by thermodynamically favored redox reactions. The ETC comprises chlorophyll pairs (A_0), phylloquinones (A_1) and 3 Fe_4S_4 clusters (F_x, F_A, F_B) within the PSI (Figure 1.3(c)). This unidirectional electron transfer is extremely fast (a total of 250 ns with the initial charge separation happening at an unprecedented ~2- 25 ps timeframe) across a potential difference of ~1V between the F_B (E_m = -530 mV vs NHE) at the stromal side and the P700 (E_m = +430mV vs NHE) at the luminal side[15]. Subsequently to complete the charge transport cycle, the plastocyanin/cytochrome donates the next incoming electron to the oxidized $P700^+$, while the ferredoxin accepts the electron from the terminal reduced F_B^-.

1.3 Application of PSI toward Bio-Hybrid Photovoltaic Device Fabrications:

The PSI is vital protein complex that catalyzes the initial steps of oxygenic photosynthesis in plants, algae, and cyanobacteria. It harnesses solar power and undergo charge separation which results in unidirectional electron transfer from luminal side to stromal side [16] of thylakoid membrane with 100% internal quantum efficiency. The light capturing is performed by large antenna system of chlorophylls and carotenoids in PSI [10]. Upon photon excitation, the electron transfer within PSI in few hundred nanoseconds posits expected theoretical photocurrent densities in mA/cm^2 based on a PSI monolayer loading of 0.5 pMol cm^{-2} [15, 17]. In fact, incredible photo voltages (~50 V) leading to internal electric fields as large as 100 $kVcm^{-1}$ have been reported for PEG-treated PSI crystals immobilized onto ITO coated glass slides, which is the highest reported for any inorganic materials[18].

Such robust structural and photoelectrochemical properties of the cyanobacterial PSI[19] have inspired many attempts in integrating it into solid-state bio-electronic devices,[20-23] bio-hybrid photovoltaic devices[24, 25]. However, the first critical step towards this is the immobilization of densely packed monolayer of PSI on conducting surfaces along with its electron path vector orientation. In this regard, several works has studied the monolayer formation of PSI on hydroxyl terminated alkane thiolate self-assembled Monolayer (SAM) on gold substrates that has indicated a 70% upward orientation [26-28]. The SAM on gold is possible due to the strong covalent bonding

of sulfur in alkane thiolate to the Au [29] and the hydrogen bonds via hydroxyl termination of the alkane brushes provide suitable interface for the immobilization of PSI [26].

Our research group has previously successfully demonstrated techniques for creating dense monolayers of active wild-type cyanobacterial PSI on self-assembled alkane thiolate (SAM) on Au substrate [27, 28, 30]. These studies suggest that aggregation of PSI in the solution due to protein-protein interactions is the bottleneck for the monolayer deposition on SAM/Au [27]. Lowering the PSI concentration in buffer solutions coupled with detergent-mediated colloidal chemistry have been effective tools in inducing de-aggregation and yielding uniform PSI monolayer in solution-phase deposition techniques. Due to the net positive charge on PSI, our group has previously employed electric field assisted deposition as an effective way for de-aggregation and surface deposition of PSI in which the applied electric field breaks the aggregates and drives single trimeric PSI complexes to the electrode surface (SAM/Au) to create dense monolayer [27]. The study of detergent-PSI interactions in buffer solution [30] has also revealed that surfactants play a major role in PSI solubilization and de-aggregation. For a fixed PSI concentration, the onset of PSI solubilization at lower n-Dodecyl-β-Maltoside (DM) concentrations had suggested that DM is a more robust and better detergent as compared to Triton X-100. For a fixed ≤0.4CMC (Critical Micellar Concentration) of DM concentrations, the PS I aggregation enhances with increasing PSI concentrations. However, at high PSI concentrations (≥ 2.8×10^{-4} mM), inter PSI distances are greatly reduced such that it prevents any rotational diffusion of PSI complexes, thereby inhibiting aggregation and leaving them in a jammed suspension that yields dense monolayer formation on the substrates. Moreover, at a fixed DM concentrations (≥ 2.2 CMC), the large number of micelles screen the PSI trimers from interacting with each other for a wide range of PSI concentrations. Thus, solution phase colloidal chemistry was used to create solution-phase jammed suspensions of PSIs in high DM concentrations (≥ 2.2 CMC) that had yielded uniform dense monolayer of PSI on SAM/Au. Furthermore, our previous works have also used confocal fluorescence microscopy test to reveal that electric field assisted deposition yielded directional attachment of PSI with its luminal side on the anodic electrode[28]. Our studies on the temperature effects during solution-phase depositions had also suggested complete phase separation of lipids and possible denaturation of PSI at temperatures ≥ 60^0C. Additionally, studies on the effects of pH showed that pH = 7 is suitable for monolayer formation on SAM/Au systems

[28]. Even though, such understanding of immobilization and colloidal phase chemistry played significant roles in achieving uniform and functional PSI assembly on active electrode surfaces, the photocurrent measurements from these PSI assemblies were largely limited by very low light absorption due to the thin-film cross-sections of ~9 nm as well as weak quantum efficiencies for the EET process in these systems as compared to the promised efficiencies of the natural membrane-bound PSI. Such observations had confounded our group for a while that ultimately serves as the motivation for the current dissertation work.

To address these issues, various strategies have been employed by several groups towards improving the photocurrent generations from PSI assembled systems while advancing the knowledge of PSI functionality under novel organic/inorganic interfacing. Initial studies had predicted the enhancement of PSI at photocurrents with better orientation of PSI due to the improved unidirectional net flow of electrons. Thus, genetically modified PSIs were employed to achieve PSI immobilization with nearly 100% orientations by using site-specific chemical anchors. To this end, direct chemical binding of PSI to the metal was made possible via cysteine tagging on the luminal side of PS I in which sulfur from the cysteine forms bonded with Au surfaces [23]. Furthermore PSI multilayers were constructed to improve the light absorption cross-sections which, in turn, increased the photocurrent generations[31, 32]. Oriented PSI multilayers fabrication have also been implemented by using cysteine-mutated PSIs along with subsequent platinization on the F_B side [32]. Specifically, in this work, the first monolayer of cysteine tagged PSIs made via the previously described genetic modifications were followed by deposition of Pt nanoparticles by photo reduction on the stromal side. Finally, the second layer of PSIs were deposited via cysteine sulfur-Pt bond and the same procedure was repeated to produce multilayers. But such methods require cumbersome genetic mutation strategies that can impair the natural PSI functionalities. To this end, simple and rapid drop casting methods with vacuum have been able to immobilize randomly oriented PSI multilayers that were able to enhance the effective photocurrents from the system by orders of magnitude as compared to monolayers due to the improved absorptions through micron thick films[31]. In this direction, novel methods for integrating PSI with other biological redox sub-units such as the cytochrome c (Cytc) using DNA scaffolds were able to create multilayered structures for improved photovoltaic properties[33]. The Cytc acted as an electrical wiring network for direct electron shuttling thereby improving the conductivity of the scaffolds, while the DNA residues acted as building blocks to construct thicker layers of PSI

composite films. Among other efforts, an efficient transparent mesoporous hybrid systems of thicknesses as high as 40 μm were also developed by integrating PSI with Cytc and ITO nanoparticles[34].

Later, the PSI immobilization on various other substrates was explored. In fact, the vacuum assisted PSI multilayers deposition was conducted on established silicon semiconductor substrates, that proved two things: the additional PSI layer on silicon can further enhance the photocurrent density & the heavily p-doped silicon is better to interface with PSI [35]. PSI also interfaced with 2D carbon materials such as graphene, carbon nanotubes which has exceptional electronic and mechanical properties[36-39]. Kaniber et. al. demonstrated the cysteine mutated PS I attachment to carbon nanotubes via covalent, hydrogen and electrostatic interactions as well as the controlling the photoconductance properties[36, 40]. While the systematic studies of PSI interfacing with graphene, graphene oxide (GO), reduced graphene oxide (rGO) materials have demonstrated higher photocurrent generation [37-39]. In addition to this, the π-system modified graphene with aromatic compounds proved to be efficient in orientated PSI immobilization and higher photocurrent generations[41-43].

A new attempt of PSI entrapment in conductive polymer was made through electro polymerization from aqueous solution of aniline and PSI [44]. It was also determined the optimal thickness and PSI concentration for better performance of the composite PSI-polyaniline films. Also, a cross linked osmium-modified redox polymer was used as both immobilization matrix and electron donor for PSI that showed improved incident photon to carrier efficiency (IPCE) [45]. An important development is that the PSI was incorporated into solid-state bio photovoltaics comprising organic semiconducting materials trapped in two electrode systems without losing PSI functionality. Interestingly, the PSI was entrapped between two semiconductors of p-doped silicon and ZnO which was achieved through a new deposition method called confined plume chemical deposition for crystalline ZnO coating onto the PSI[46]. Such efforts demonstrated the ability to move towards solid state cells from previously investigated wet PSI-cells.

Some research groups also focused on integrating PSI with novel materials for the end goal of PSI bioelectronic or PSI biohybrid devices for other applications of solar hydrogen production and biosensors[47-50]. Replacing titanium support with PSI for photocatalytic H_2 production from Pt nanoparticles has advantageous due to the lower band gap needed for PSI excitation than the

titanium. This was demonstrated with construction of a bioconjugate PSI/molecular wire/cytochrome c6/Pt nanoparticle for performing better photocatalysis H_2 production from H^+ protons[51]. A stable cell free hydrogen production that is temporally and thermally stable was also demonstrated with platinization on PSI in the presence of ascorbic sacrificial donor in the solution[52]. Interestingly, PSI was coupled with Field Effect Transistors (FET) via reconstituted molecular wire with gold nanoparticle and demonstrated successfully the first bio-photosensor controlling the FET with electrons generated from PSI which can be used as interpreting gradation in images[49]. PSI with glucose oxidase enzyme provides as excellent example of showing wide potential of PSI, where the conjugation was utilized as photo biofuel cells that can be used as glucose sensor using solar energy while generating electrical power[53]. Although such efforts are significant advancements in demonstrating PSI ubiquitous nature by integrating with versatile materials, the knowledge gap exists in ways of utilizing the full potential of PSI for efficient light harvesting and charge separation for solar energy conversion. Even after genetic modifications of photosystem offers preferential orientation, it often significantly reduces the functionality of PSI Even though the overall photocurrent output is significantly enhanced especially through the PSI multilayer systems of huge thickness, there is neither clear understanding of the random oriented PSI system, nor the evidence of improving the efficiency of individual PSI units. One needs to note that in all these works, the PSIs were devoid of their natural thylakoid membrane housing that often results in non-native conformational changes and alter membrane protein functionalities in undesirable ways.[54-56] In fact, none of these engineering constructs could unleash the full potential of photocurrent generations expected from a ~100% QE photon-to-electrochemical energy conversion promises for natural membrane bound PSI.

1.4 Microenvironment Alterations for PSI Assembly at Biotic-Abiotic Interfaces:

To address the aforementioned challenges faced so far by the photosynthetic research community in creating robust and functionally efficient PSI-based systems, recently our group has specifically focused on the use of microenvironment alterations around the PSI to investigate the functional role of the natural membrane scaffolds of PSI in tuning its optoelectronic and chemical properties. To this end, our group has now reported a series of works demonstrating the unique and intriguing effects of PSI confinements in various inorganic/organic scaffolds on its optical and photocurrent generation characteristics. PSI confinements in highly porous and robust metal organic framework (MOF) structures had revealed the structural and functional stability of PSI

even under harsh exposures to denaturing surfactants and organic solvents [57]. Even though, the various strategies were effective in advancing the performance of the PSI towards bio-hybrid and bio-catalytic device fabrications, the role of microenvironment alterations arising from the native membrane housing of PSI in orchestrating its photoactive functionalities remains elusive! Such investigations require systematic reconstitution of naturally extracted PSIs into synthetic lipid membranes that can mimic its native membrane-bound state. To this end, recently our group has demonstrated the successful reconstitution of PSI into biomimetic synthetic lipid membranes through detergent mediated solubilization of 1,2-diphytanoyl-sn-glycero-3-phospho-(1′-rac-glycerol) (DPhPG) liposomes[58, 59]. The photocurrents measured from these membrane-confined PSI systems had revealed a surprising ~4-5 fold enhancements [60]. The PSI-DPhPG proteoliposome absorption shows significant blue shift of absorbance peaks in blue region and red region compared to unconfined PSI indicating the microenvironment modification around PSI[59]. Also, clear indication for successful incorporation of PSI into lipid membranes was obtained through cryo-TEM measurements where the lipid bilayer thickness increased from 3.3 ± 0.37 nm to 9 ± 0.91 nm upon PSI incorporation[60]. Finally, a direct evidence was observed through liquid AFM topography mapping of PSI-DPhPG liposome showing both parts of lipid and protruded PSI units coming out from the lipid bilayer[60].

Motivated by these studies, the current thesis will specifically focus on the effects of microenvironment alterations in PSI systems based on two types of confinements: 1) Localized Surface Plasmon Resonance (LSPR) mediated electromagnetic fields and 2)biomimetic synthetic lipid membranes with different stiffness and charged head groups. LSPs are coherent localized

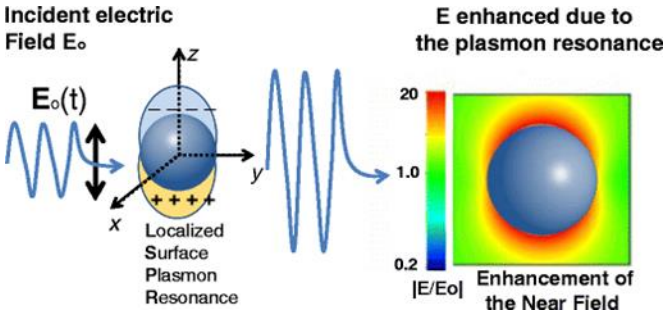

Figure 1.4 Schematic representation of LSPR effect of enhanced electric field around nanosphere upon light excitation [61]

oscillations of electrical charge on metallic nanoparticles and nanostructures upon light excitations[62]. This occurs when the nanoparticles are comparable or less than the size of the incident light wavelength. This phenomenon is due to the interaction of incident light with the conduction band electrons on the metal surface[63]. The LSPs have two important effects: 1) Enhanced localized electric field near the surface, and 2) Absorption of nanoparticle system with maxima at the resonant frequency. The resonance or LSPR from plasmonic metal structures at a particular incident light wavelength manifests itself due to an enhancement in the light trapping and near-field amplitudes that appears as maxima in the absorption spectrum of the metal nanoparticles/nanostructures. The LSPR absorbance spectra and resonance peak positions depend on various properties of the plasmonic nanostructures involved including material compositions, size, geometry, spatial arrangements of the nanostructures and their surrounding dielectric medium[62-66]. The LSPR electric field intensity drastically decreases with the increasing distance from the metal surface[63].

LSPR of plasmonic metal nanostructures/nanoparticles have been known to modify the optoelectronic properties of the neighboring organic molecules or single fluorophore. Thus, they have been used to enhance the photocurrent generations in organic/dye sensitized solar cells and intensify the detection limits for fluorescence-based sensing in biotechnology[67-72]. However, there exists a lack of detailed systematic investigations into the complex and intriguing effects of LSPR-induced electric fields on a multi-chromophore, bulky (1068 kDa) and transmembrane protein complex such as PSI, where multiple photoactivated cofactors work in highly well-orchestrated fashion to achieve highly efficient light harvesting and excitation energy transfer to its reaction center for charge separation. One can easily surmise that the FRET mechanism among the chromophore networks, commonly hypothesized as the plausible route for the EET process, could be significantly affected and altered by the separation distance between the individual chromophores within PSI and the plasmonic metal surfaces as well the changing orientations of the dipole moments of the chlorophylls[73]. A handful of studies that investigated the plasmonic effects on PSI systems till date have mostly focused on the changes in their optical properties such as absorption and fluorescence characteristics [74-76]. These studies suggested that the plasmon resonances can induce novel pathways for excitations and emissions within the chromophore network[73, 75-77]. However, there is a clear knowledge gap when it comes to a direct

investigation into the effects of LSPR on plasmon-enhanced photocurrent changes in PSIs assembled with plasmonic metal structures. To the best of our knowledge, the only relevant work in this area can be found in a theoretical investigation that clearly posited significant plasmon-enhanced photochemical productions despite the reduced quantum yields due to excitation energy losses[78]. To bridge this critical knowledge gap, extensive and meticulous experimental investigations are much needed to establish the robust relations between plasmonic field enhanced light excitations in PSI and the resultant photocurrent enhancements. Noble metal nanostructures such as Ag and Au have been well-known to exhibit LSPR effects in the visible wavelength range that can effectively couple with PSI's broad absorption over the visible span of the solar spectrum. Herein, one can see ample opportunities for tuning the resulting LSPR peak positions from carefully tailored Ag and Au nanostructures/nanopatterns with controlled design of their sizes, shapes and spatial distributions. Such tunability of the plasmon resonance responses can allow systematic investigation into spectrally resolved plasmonic effects on the photocurrent responses from PSI assemblies.

As part of continuation of understanding the effects of PSI confinement in biomimetic lipid membrane, it becomes imperative to gain mechanistic insights into the dynamic functional role of membrane confinements, beyond being the structural scaffold, in tailoring photoexcitation/dissipation pathways and conformational changes in PSI. The 4-5 fold photocurrent enhancements from PSI-confined supported lipid bilayers as compared to the unconfined PSIs[79] that could be attributed to better protein orientations, conformational changes, and/or coherent interactions among PSI chromophores architected by the membrane environments. However, since mere orientations cannot explain such large photocurrent enhancements, we posit that conformational and structural changes in PSI in conjunction with altered protein-membrane interaction dynamics could have played major roles in tuning the photocurrent responses which, in turn, itself becomes a critical area of investigation. The structural, conformational and functional changes in PSI need to be investigated to explain the 4-fold enhanced photocurrent and gain fundamental insights into the role of lipid confinement of PSI, the. The intrinsic interactions among cofactors can be changed due to such microenvironment alterations that can be inferred through tracking the spectroscopic property changes.

Motivated by the aforementioned challenges and a lack of fundamental understanding in this area, the current studies in this thesis aims to systematically investigate the role of

microenvironment alterations, architected via plasmonic and lipid confinements, in altering the photoexcitation pathways and optical properties of PSI. From an engineering perspective, this in turn allows us to tune and orchestrate the ensuing photocurrent generations and enhancements from PSI systems assembled with suitably fabricated plasmonic metal nanopatterned structures and biomimetic lipid membranes. The hypothesis behind the electromagnetic confinement is that the additional plasmon induced resonance energy transfer (PIRET) will result in enhanced photocurrent generations in PSI through the dipole-dipole coupling between PSI and plasmon. The LSPR method of photocurrent enhancement strategy is versatile which can be coupled with other enhancement strategies mentioned previously for greater PSI performance in variety applications of PSI based bio-hybrid photovoltaic, photocatalytic and biosensor devices. This method will improve the functionality of individual PSI that is confined under the localized plasmon electric field through the improved excitation rates of charge separation. The optical absorption can be finely tuned to both overlap and supplement the PSI absorption using the microenvironmental alterations around the PSI. Furthermore, the current study will shine light on a more fundamental understanding of the intrinsic inter-chromophore energy transfer mechanisms, interactions and protein conformational changes in PSI that can be tuned as desired with well-designed plasmonic resonance modes and lipid membranes.

To achieve the aforementioned research objectives of this thesis work, the current dissertation will be present the following research directions in the ensuing chapters:1) First ever experimental observation of plasmon enhanced photocurrent in photosystem I, for which Fischer nanopatterns of plasmonic silver nanopyramid structures were tuned to couple the LSPR with absorption bands in PSI (Chapter 2) [80].

2) Role of the specific plasmon resonance peak positions of gold and silver nano discs structures that are fabricated using high precision Electron Beam Lithography on tuning the excitation pathways in PSI (Chapter 3).

3) Systematic investigation of conformational, structural and functional changes of cofactors in PSI due to the synthetic lipid membrane confinement and determining the correlation between the aforementioned changes to the ionic and stiffness of designed phospholipids (Chapter 4).

Chapter 2

Plasmon Enhanced Photocurrent from Photosystem I Assembled on Ag Nano-Pyramids

This chapter is based on the published paper.

"Plasmon-Enhanced Photocurrent from Photosystem I Asssembled on Ag Nanopyramids" Ravi Pamu, V Prasad Sandireddy, Ramki Kalyanaraman, Bamin Khomami and Dibyendu Mukherjee, The Journal of Physical Chemistry Letters (2018) 9, 970-977.[80]

2.1 Introduction

Natural photosynthetic processes harness solar energy with nearly 100% quantum efficiency. Central to this process is the supra-molecular protein, PSI which acts as a biological photodiode and undergoes photochemical charge separation resulting in unidirectional electron transfer across the membrane bound protein[81, 82]. It is commonly proposed that the antennae chlorophylls and carotenoids in PSI channel the excitation energy to the reaction center chlorophyll pair (P700) via the Forster resonance energy transfer mechanism[83] that initiates the electron transport pathway to the PSI acceptor terminals[10, 47, 84]. The robust structural and photoelectrochemical properties of cyanobacterial PSI[11] have inspired recent attempts in integrating it into solid-state bio-electronic devices,[20-23] bio-hybrid photovoltaic, solar H_2 production, and bio-sensor technologies[24, 25, 47-49, 53, 85-87]. To this end, a well-studied construct based on PSI immobilization on alkanethiolate hydrophilic self-assembled monolayer substrates that can allow optimal electron tunneling pathways has been developed[22, 26-28, 88, 89]. More recent efforts has been directed to tune the photo response and photocurrent generation from PSI constructs confined in designer lipid bilayer membranes and conducting polymer scaffolds that mimic the natural thylakoid membrane housing of PSI[58, 59, 86]. But, the low light absorption capacities of these thin films prevents significant photocurrent generation from PSI monolayers[49, 90]. A plausible strategy to circumvent such problems is to integrate PSI with plasmonic metal nanoparticles[91]. LSPR-induced collective oscillations of surface electrons of

the nanoparticles create highly localized electric fields and make absorption possible at resonant frequencies.

Localized Surface Plasmon Resonance (LSPR) in noble metal nanostructures are known to modify emission and excitation rates in neighboring organic dyes and biomolecules,[92] and enhance photocurrents in dye-sensitized[71, 72, 93-95] and organic solar cells[96, 97]. Moreover, plasmon enhanced photocurrents have been observed with other bacterial light harvesting complexes[98, 99]. However, the few studies conducted on plasmonic interactions of Au and Ag nanostructures with multi-chromophores coupled PSI[73-78, 91, 100, 101] have mostly focused on their unique effects on absorption and fluorescence emission characteristics. An interesting observation from these studies is the blue shift in the fluorescence emissions of PSI chromophores due to plasmonic interactions with red-light excitation. Additionally, enhanced fluorescence in the 698-710 nm wavelength ranges of the PSI emission profile indicate fluorescence deactivation of higher energy antenna chlorophylls. This should imply a reduction in energy transfer efficiency between chlorophyll antennae and P700 responsible for charge separation and photocurrent generation. But, such high-energy emissions being virtually absent without plasmonic interactions might also lead to activation of novel plasmon-induced pathways for chromophore-chromophore interactions and new energy transfer pathways[73, 75, 77]. Such complex and intriguing photo physics of PSI coupled with plasmonic nanostructures underscores the critical yet unanswered questions regarding the alterations in photocurrent generations from plasmon-coupled PSI systems! Although, the plasmon-enhanced photocurrents in PSI has not been measured; prior theoretical studies based on highly simplified photo physics of the process have suggested such enhancements[78]. Specifically, a prior study indicating enhanced photocurrents from PSI deposited on gold nanoparticle clusters has mostly ascribed the effect to the enhanced surface area from the nanoparticle clusters[101]. In fact, the aforementioned theoretical model for PSI coupled with Ag and Au spherical nanoparticles and nano shells has revealed that, despite a reduced quantum yield, plasmon-induced electron production rates could undergo 6 to 15-fold enhancements for the various Ag, Au nanostructures at the resonant frequencies[78].

This work, not only provides experimental proof of LSPR enhanced photocurrents from cyanobacterial PSI, assembled on plasmonic structures made out of Ag nano-pyramids (Ag-NPs),

but also confirms that relatively simple models of the photo physics of the system can indeed provide correct order of magnitude enhancement of the photocurrent.

2.2 Experimental Methods

Sample Preparation. Commercial 50-80 nm thick ITO coated sodium lime glass substrates (NANOCS: IT100-111-25) cut into 1cm x 1cm size were first cleaned in RCA with 5:1:1 volume fractions of H_2O:30% NH_4OH:30% H_2O_2 with 15 minutes of sonication to remove the organic residues. The substrates were further sonicated in DI water for 15 min. All solvent and washing agents (NH4OH, H2O2) were purchased from Fisher Chemicals. Planar Ag substrates were prepared by depositing Ag on cleaned ITO substrates in high vacuum (~1 x 10^{-8} torr) by electron beam deposition (Model Mantis QUAD-EV-C) at room temperature. For Ag-NP preparations, 500 nm size polystyrene latex beads in a 2.5 wt% dispersion (Alfa Aesar-42714) were diluted with ethanol in 1:10 volume fractions first. The diluted beads solution was added drop by drop on to the base of the Petri dish glass partially filled (not covering the entire base) with DI water. Each drop pushed close to the Petri dish glass-water-air triple interface. The surface tension gradient forces the beads to migrate to the surface of water in the dish. This process is repeated until the beads cover the entire water surface with high packing density. The Petri dish was then carefully filled with water. The hexagonally packed monolayer of the beads with lowest defects was identified with its interference pattern on the water surface and scooped onto a clean ITO substrate. Following this procedure, 81±4 nm thick Ag was deposited using electron beam deposition method. And finally, the polymer bead mask was removed by sonication in ethanol for less than 1 min, leaving behind the Ag-NP Fischer patterns on ITO.

Each of the ITO, Planar Ag, and Ag-NP/ITO substrates was thiolated by immersing it in 5 mM 6-mercapto-1-hexanol (obtained from Sigma-Aldrich) solution in ethanol for 7 days under N_2 environment and at room temperature. Subsequently, the as-obtained SAM/ITO, SAM/Planar Ag and SAM/Ag-NP/ITO substrates were thoroughly rinsed with isopropanol to remove any unbound thiol molecules. While sonication is a preferred method for ensuring only monolayer formation, such treatments were found to dislodge the Ag-NPs from the ITO surface and hence were not applied here. The PSI complexes from the wild type PCC6803 were acquired from the stock solution that was prepared and reported in an earlier work[102]. For PSI immobilization, the SAM-

coated wafers were immersed in 0.013 μM PSI solution with 0.02% w/v n-dodecyl-β-D-maltoside surfactant in aqueous 200 mM sodium phosphate buffer (pH =7) for 24 hours in dark at room temperature. The PSI/SAM/ITO, PSI/SAM/Planar Ag and PSI/SAM/Ag-NP/ITO substrates were finally thoroughly rinsed with DI water and dried under pressurized N_2.

Sample Imaging. A Zeiss Merlin SEM with accelerating voltage of 3kV was used to image the Ag-NP/ITO electrode surface. Plasmonic resonance peak measurements were obtained via optical transmission spectrum of Ag-NP/ITO electrodes which were measured with an HR2000 + ES spectrometer from Ocean Optics. All surface topography images were collected on an NT-MDT AFM instrument in the tapping mode using silicon cantilever tips compatible with softer biological materials (NT-MDT; Model: NSG03). The tip had a force constant of 0.35-6.1 N/m along with a resonant frequency of 90 kHz.

Electrochemistry measurements. All CA measurements were carried out with an electrochemistry set-up using a potentiostat from Bio-Logic (Model: SP-300) and performed in custom built standard 3-electrode electrochemical cell where ITO, PlanarAg, and Ag-NP/ITO substrates were used as the working electrodes, Pt wire as counter electrode and Ag/AgCl (sat. NaCl) as the reference electrode (BAS Inc.; Model: MF-2052). 1 mM aqueous methyl viologen was used as the soluble electron scavenger along with 100 mM KCl used as the supporting electrolyte. The 4 collimated LEDs purchased from Thorlabs with the nominal wavelengths of 395 nm, 420 nm, 470 nm and 660 nm (model: M395L4, M420L3, M470L3, M660L4) were operated with a power density of 25mW/cm^2 reaching the working area when the solution in the cell was absent. The LED power densities were measured using a power meter purchased from ThorLabs (Model: S302C). All chronoamperometric measurements were performed at open circuit voltage with the on/off light cycles being operated with 2 minutes intervals each and repeated for at least 6 cycles. The results reported are based on averaging the system response over 6 cycles.

2.3 Results and Discussion

Figure 2.1(a) shows the well-known absorbance peaks for colloidal suspensions of cyanobacterial PSI in aqueous solutions, i.e., 439 nm and 678 nm. The plasmonic resonance coupling with PSI requires the plasmon peaks of the fabricated metal nanostructures to overlap

closely with the PSI absorption peaks[78]. To this end, the parameters of the NSL technique were tailored with optimized Ag deposition thickness and polystyrene beads diameter to result in the formation of the desired Ag-NP structures on the ITO wafer with overlapping absorbance at ~ 680 nm (see Figure 2.1). The plasmonic peak positions for the Ag NPs were found to be less sensitive to the thickness changes in the deposited Ag /Ag-NP heights but highly sensitive to the percentage of defects (bow tie-like structures) formed due to imperfect hexagonal packing of the polystyrene beads. It was observed that the Ag deposition thickness of ~81 nm and polystyrene bead diameter of 500 nm results in the optimally designed Ag-NPs with the strongest broadband LSPR peak at ~675 nm that overlaps very closely with the PSI absorption peak at 678 nm (Figure 2.1). Additional lower intensity absorption peaks centered at 447 nm and 360 nm are also observed for the Ag-NP plasmonic structures, as seen from Figure 2.1(a). The 447 nm plasmonic absorption spreads over 410 - 485 nm; hence it overlaps closely with the PSI broadband absorption peak at 439 nm in the violet-blue region. The as-fabricated Ag-NP structures are also visualized with scanning electron microscopy as shown in Figure 2.1(b) depicting the regular Ag-NP triangular structures on ITO.

For direct comparison reported here for PSI on Ag-NP structures, control substrates of planar Ag on ITO with no plasmonic effects were also prepared. Planar Ag substrates are highly

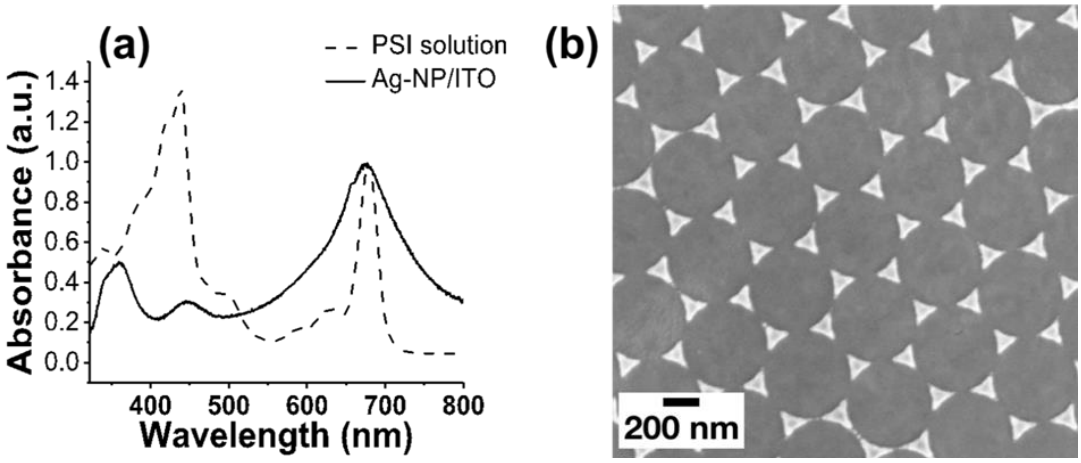

Figure 2.1 (a) UV-Vis absorbance spectra for PSI in solution and Ag Nano Pyramids (Ag-NP) on ITO substrate. (b) SEM image showing Fischer patterned Ag-NP structures prepared via NSL technique.

reflective with the transmission spectrum confirming the absence of any plasmonic peak absorptions. Additionally, bare flat ITO was selected as background electrode samples for comparison of measured photocurrents. As detailed in the experimental methods section, all three electrode samples of ITO, Planar Ag and Ag-NP/ITO, coated with SAM of OH-terminated C6 thiol, were incubated in PSI colloidal suspensions containing 0.02% w/v detergent to achieve PSI monolayer immobilization on the surfaces. The specific detergent concentration, resulting in 2.2 times the critical micellar concentration of DM surfactants (2.2CMC), has been shown to create PSI jammed colloidal suspensions that result in PSI monolayer formation during solution phase incubation. The PSI attachment to each of the 3 electrode samples was visualized with atomic force microscope (AFM) before and after PSI/SAM coating.

As shown in Figure 2.2(a), the homogenous and smooth flat ITO substrate, with surface roughness <1 nm, start indicating higher roughness and regular circular patches of densely packed PSI for the PSI/SAM coated ITO substrate shown in Figure 2.2(b) (Inset indicates approximate surface roughness ~ 6 - 7 nm and width of roughness profile ~25 - 30 nm). Similarly, the AFM image in Figure 2.2(c) for the planar Ag electrode surface indicates polycrystalline Ag islands with roughness < 10 nm and width ~ 60 - 100 nm. On the contrary, the PSI assembled on planar Ag substrate in Figure 2.2(d) indicates sparse PSI distribution and cluster formations atop the Ag islands as also indicated by the inset showing line cross-sectional roughness of < 7-8 nm and width of ~25- 30 nm on top of the wider cross-sectional profiles of Ag islands. The lack of visible dense PSI monolayer on this surface as compared to the ones on ITO could be attributed to the relatively. higher surface roughness for the Ag island deposition. In conjunction, the AFM topographical images in Figure 2.3(a) and 2.3(b) for the Ag-NP/ITO substrates along with respective phase images in Figures 2.3(c) and 2.3(d) clearly show the dense PSI monolayer formation on Ag-NP and surrounding ITO areas. The cross-sectional height profiles of Ag-NPs with (~90 nm) and without (~82.4 nm) PSI coatings in Fig. 2.3(a) and 2.3(b) insets also support this (typical PSI trimer height being ~9 nm). The uniform PSI attachments throughout the Ag-NP/ITO substrate is expected since the thiol SAM layer forms both on ITO and Ag surfaces during the incubation step in thiol solution. Finally, the diameter and height of the PSI complexes on all the three electrode surfaces (in Figure 2.2(b), 2.2(d) and 2.3(d)) are in agreement with our previous measurements of PSI monolayer on Au substrates[30, 90].

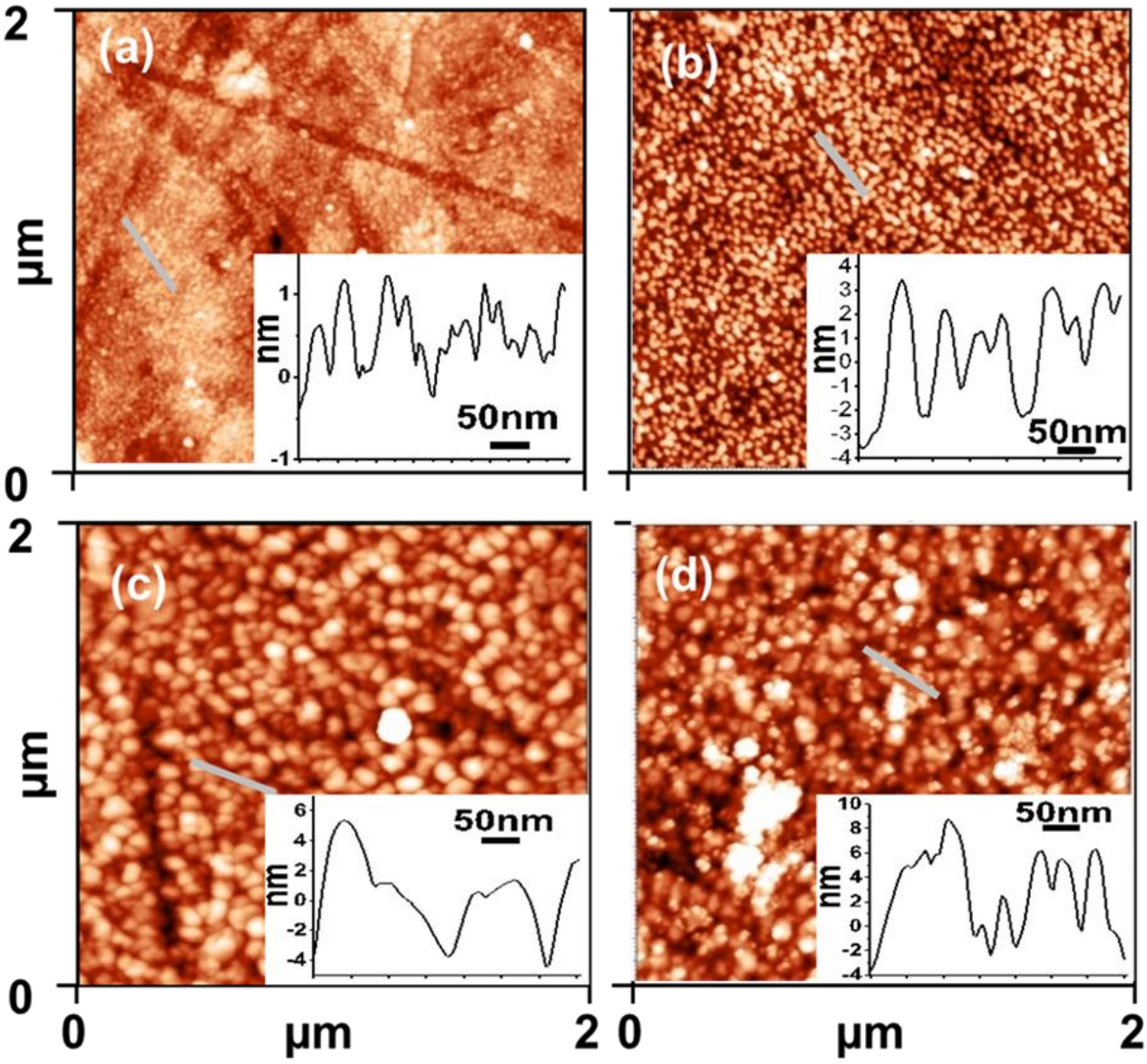

Figure 2.2 Topographical AFM images of flat ITO (a, b) and planar Ag/ITO (c, d) electrode substrates before (a, c) and after (b, d) PSI/thiol SAM assembly respectively.

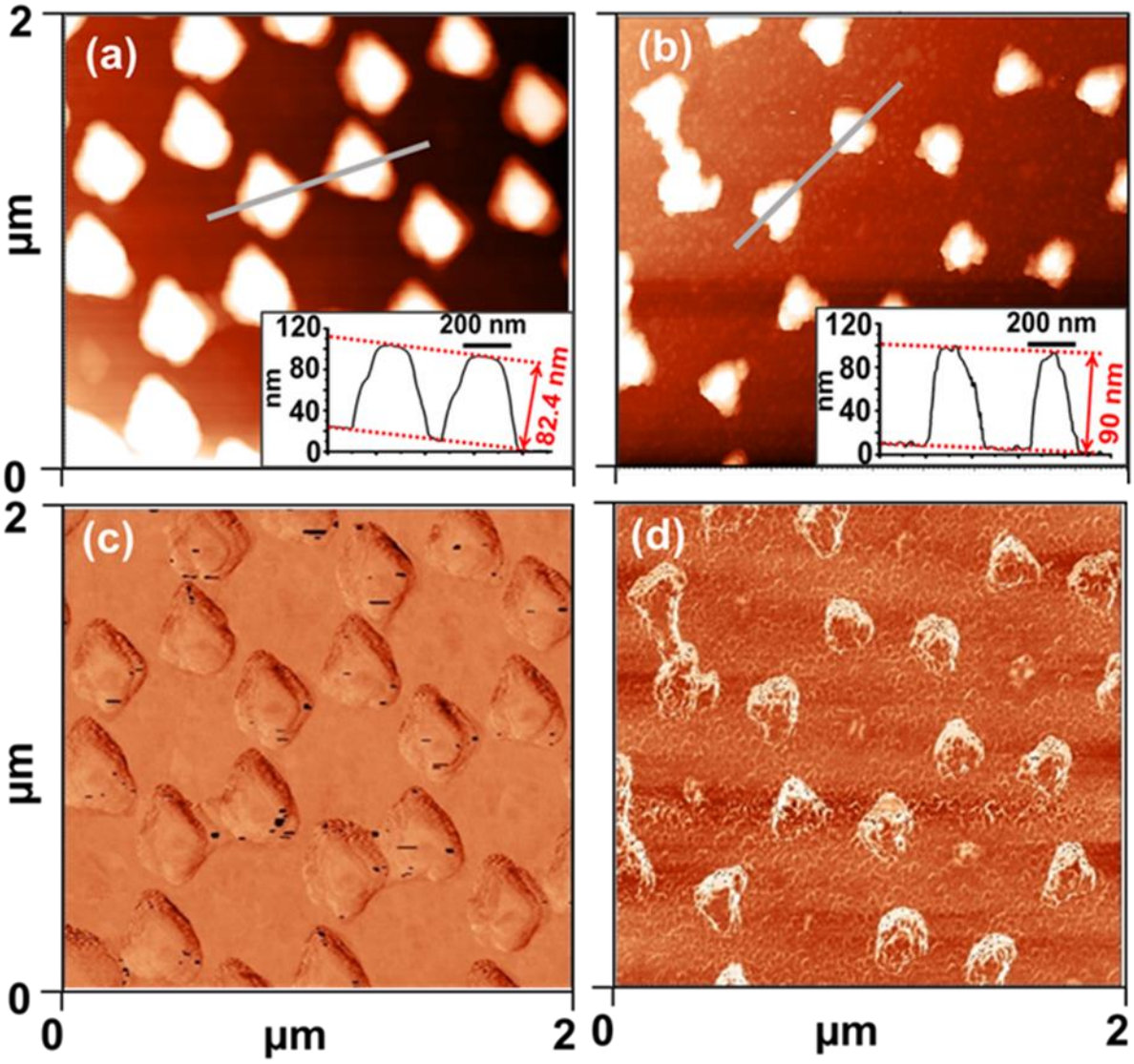

Figure 2.3 AFM images of Ag-NP/ITO substrates before (a) and after (b) PSI/SAM assembly along with the respective phase images for (c) Ag-NP/ITO and (d) PSI/SAM/Ag-NP/ITO substrates. (Insets: Height profiles across sections marked in (a) & (b)).

The wavelength-dependent plasmon-enhanced photocurrents from PSI was investigated using 4 LEDs with peak wavelengths at 395, 420, 470 and 660 nm as excitation light sources and 3 working electrodes of PSI assembled on SAM/X (X= flat ITO, planar Ag and Ag-NP/ITO) substrates. Specific photocurrent contributions from each of these substrates are deduced by subtracting the background photocurrents measured from the respective control SAM/X substrates. Figure 2.4(a) depicts a prototypical Chronoamperometry (CA) data set for 660 nm light excitation indicating the stable photocurrents generated from the PSI/SAM/Ag-NP/ITO and the respective backgrounds from the control SAM/Ag-NP/ITO and Ag-NP/ITO substrates. To provide a clear comparison with respect to photocurrents generated from PSI assembly on planar base substrates (devoid of Ag-NP structures) as the control working electrodes, Figure 2.4(b) also charts the CA data for PSI/SAM immobilized on flat ITO, and planar Ag along with the observed data for PSI/SAM/Ag-NP/ITO. It needs to be pointed out here that the working electrode with an effective 3.1 mm radius circular spot gets exposed to the charge carrier solution in the electrochemical cell. Hence, the nominal working area for the electrodes is 30.19 mm^2. For the results reported in Figure 2.4, this nominal area is taken as the effective working area for all the electrodes. In the case of planar Ag/ITO and flat ITO electrodes, the total exposed area is from the flat Ag surface and the ITO respectively. In the case of Ag-NP/ITO sample, the exposed area comprises a mixture of Ag areas in the form of Ag-NP and the rest of the exposed ITO surfaces. Figure 2.4 clearly demonstrate a distinct increase in the photocurrent generation during the light on period from the PSI/SAM/Ag-NP/ITO substrates as compared to the ones from either the SAM/Ag-NP/ITO (Figure 2.4(a)) or the PSI/SAM/planar Ag (Figure 2.4(b)) electrodes. These observations validate the specific photocurrent enhancements resulting from the presence of surface assembled PSI (Figure 2.4(a)) and more significantly, from the PSI assembly on the Fischer patterned SAM/Ag-NP/ITO substrates (Figure 2.4(b)). The minor photocurrent increases from SAM coating on both planar Ag and Ag NPs by itself (see table AI.1 in Appendix I) can be attributed to work function changes of Ag surface due to the molecular dipole moments of attached thiol as also observed earlier[103-108]. Effective photocurrent contributions from surface assembled PSI on each electrode X, as shown in Figure 2.5(a), are subsequently estimated by subtracting the background photocurrents of SAM/X electrodes from the corresponding values of PSI/SAM/X electrodes (X = flat ITO, planar Ag, Ag-NP/ITO). Except for the PSI assembled on

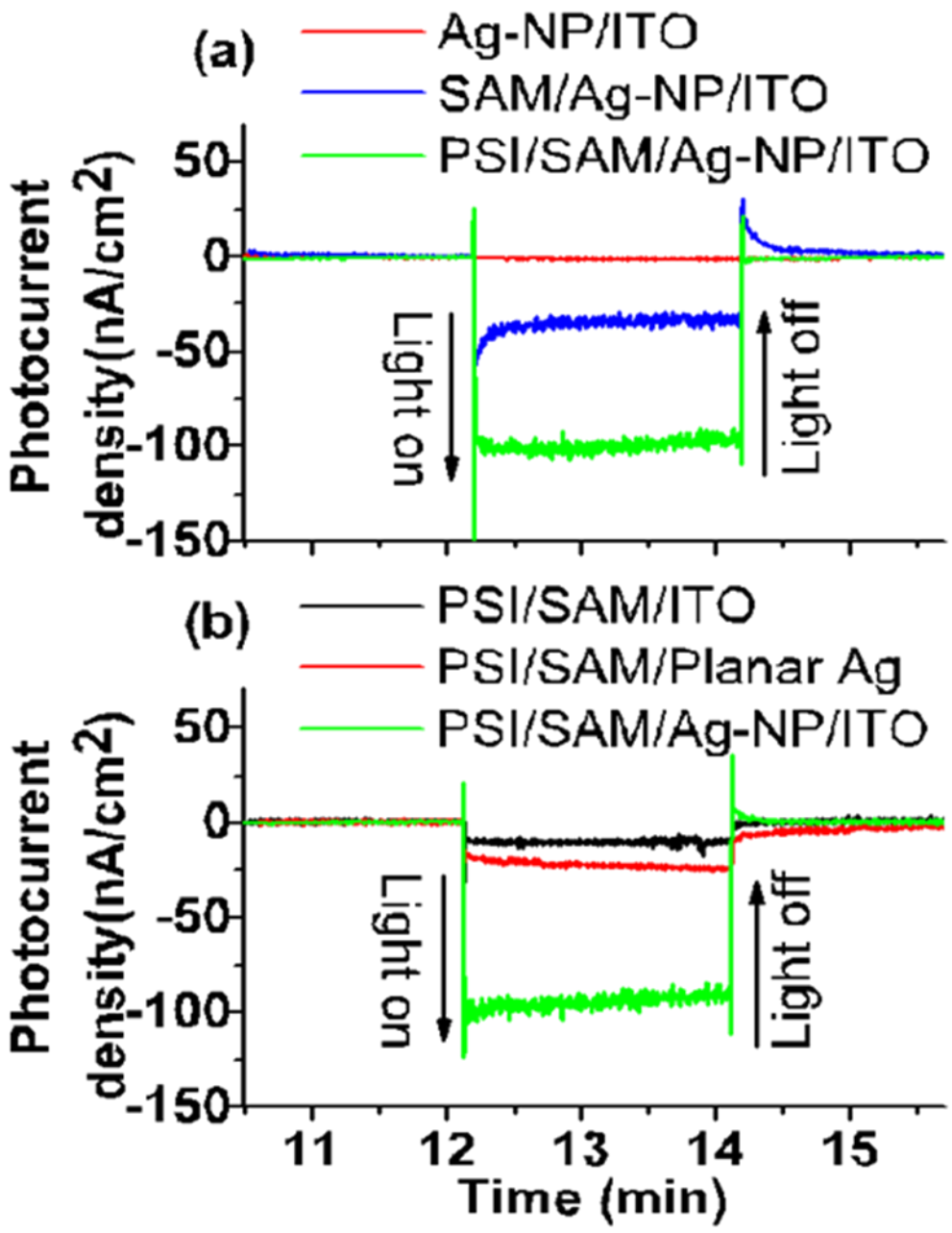

Figure 2.4 Chronoamperometry data of cathodic photocurrents (electron transfer from electrode through PSI to solution mediator) from light on-off experiments on: (a) Ag-NP/ITO, SAM/Ag-NP/ITO and PSI/SAM/Ag-NP/ITO substrates, and (b) PSI/SAM/ITO, PSI/SAM/planar Ag and PSI/SAM/Ag-NP/ITO at open-circuit potential under illumination from l = 660 nm LED (36 mW/cm^2) in aqueous solution carrying 1mM methyl viologen as charge carrier, and 100 mM KCl as supporting electrolyte (Ag/AgCl and Pt wire are used as reference electrode and counter electrode respectively).

Ag-NP electrode, the effective PSI photocurrents show an increasing trend with decreasing wavelengths of the light. This can be attributed to the non-plasmonic effects arising from enhanced photochemistry of surface adsorbed methyl viologen and change of work function of the working electrode has also been commonly observed in earlier studies[109]. This effect is evidently predominant for the planar Ag as compared to the ITO electrodes.

It is also observed that the effective photocurrent for the PSI on Ag-NP/ITO electrode is the lowest at 395 nm excitation and almost close to the value of ITO electrode. In the absence of any plasmonic peak interactions with PSI at 375 nm (see Figure 2.1(a)), this observation can be simply explained by the relatively lower effects of the non-plasmonic initiated photocurrents largely from the PSI covered SAM/ITO surfaces since only 32% of the effective silver are in the form of Ag-NPs on the substrates (see Appendix I). The more interesting observation from Figure 2.5(a) is the trend in the effective photocurrents from PSI on Ag-NP/ITO electrode, when compared to that from PSI on planar Ag electrodes, clearly indicating a drastic increase at 420 nm, 470 nm and 660 nm where the Ag-NP plasmonic peaks overlap with the dominant PSI absorption peaks. Such enhancements can be readily attributed to the localized plasmon-induced electric field enhancements from the Ag-NP structures coupling with the PSI systems to create pathways for enhanced absorption at the resonant frequencies.

Finally, the photocurrent enhancement factor from the LSPR-induced interactions of Ag-NPs with the PSI were calculated based on the photocurrent generation per PSI trimer on each electrode which were deduced from the respective effective photocurrent densities and the PSI trimer number density on each electrode (see Appendix I for detailed calculation). Here, the increased additional surface area of 0.323 times the nominal surface area due to the 3D Ag nanostructures for the Ag-NP/ITO electrodes was accounted for in our calculations (Appendix I). Since the PSI is uniformly distributed on both Ag-NPs and ITO parts of the Ag-NP/ITO electrode surfaces, the photocurrent recorded evidently has contributions from the PSI proteins immobilized on both the ITO and the Ag-NP areas. Here one needs to bear in mind that the electric field generated by LSPR is highly localized and typically undergoes rapid decay with distance from the plasmonic metal structures. Such observations have also been made in earlier studies indicating the rapid decay of evanescent field based on drastic decrease in the incident photon to current efficiency as

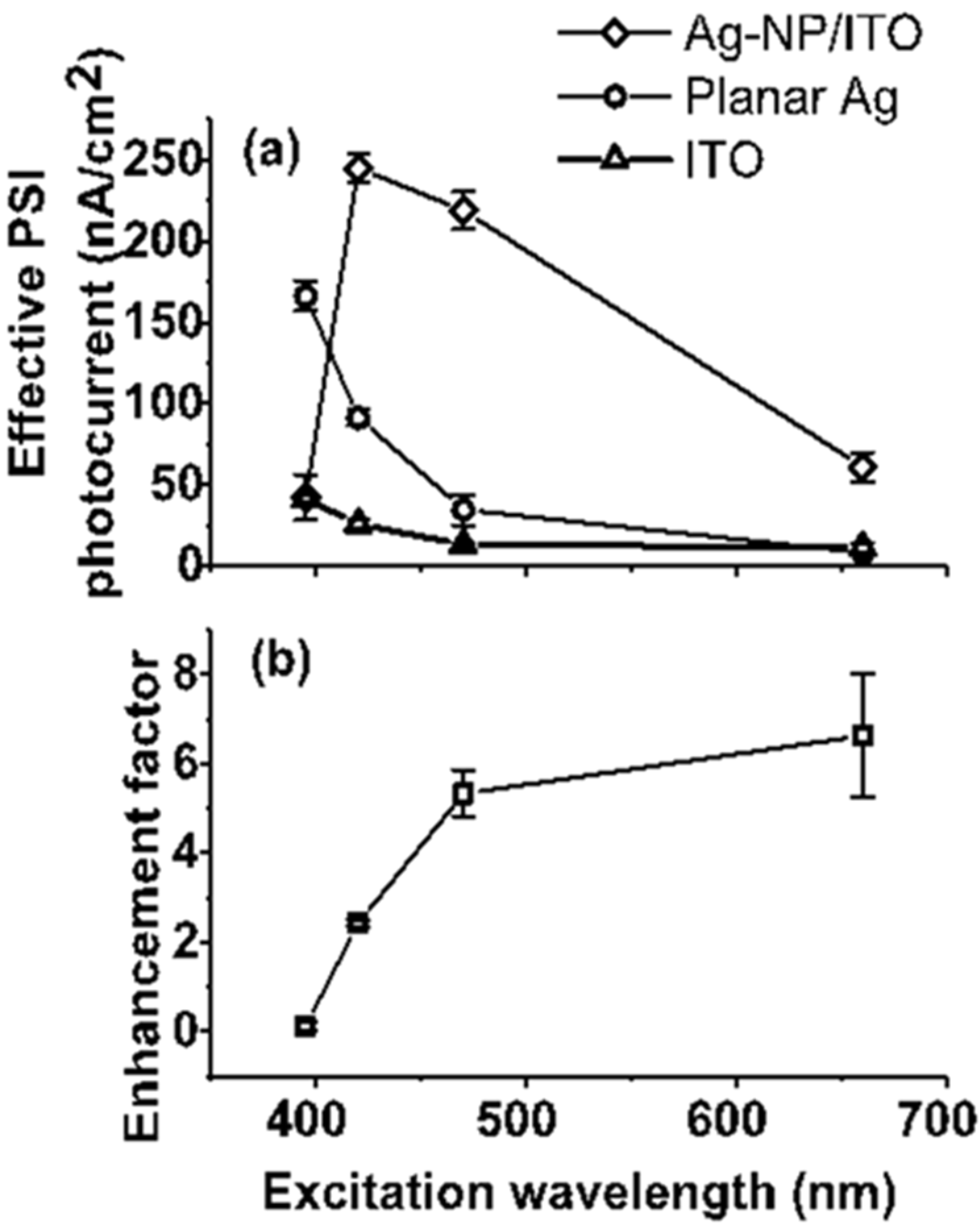

Figure 2.5 (a) Effective absolute value of photocurrents (PSI/SAM/X – SAM/X) from PSI assembly on electrodes where X=ITO, planar Ag, Ag-NP/ITO (b) LSPR-induced photocurrent enhancement factors based on the ratio of effective photocurrents per PSI on Ag-NPs to that from planar Ag.

distance between Ag nanoparticles and dye molecules in DSSC increased from 2 to 8 nm[95]. Since, in the present study, the thickness of PSI/SAM layers on Ag-NP surface is in the range of 8 - 10 nm, one can fairly assume that there will not be any plasmonic effect from the edges of the Ag-NP structures on PSI proteins attached to the ITO surface. Furthermore, since the photocurrent contribution from plain PSI/SAM/ITO electrode is minimal (Figure 2.5(a)), it is reasonable to assume that photocurrent contributions for the PSI/SAM/Ag-NP/ITO data could be decoupled between those from PSI on the ITO surface and PSI on Ag-NP surface to establish the actual plasmon enhanced photocurrents.

To this end, the relative percentages of smooth ITO surface area and Ag-NP surface area are estimated from the SEM and AFM images of the Ag-NP/ITO surface (see Appendix I for detailed calculations of actual surface areas and PSI number densities on the various electrodes, and for the estimation of photocurrent densities per PSI as well as the enhancement factors). Hence, based on these deductions the photocurrent contributions per PSI attached to the Ag-NPs, the final plasmon-induced photocurrent enhancement factors are calculated as the ratio between the effective photocurrents per PSI on Ag-NP and planar Ag electrodes. The detailed geometric and mathematical calculations for the aforementioned estimations can be found in the Appendix I document. Based on these calculations, as seen from Figure 2.5(b), the highest LSPR-induced photocurrent enhancement factor of ~6.5 is observed at the excitation wavelength of red light, λ = 660 nm. This can be clearly attributed to the strong coupling between the LSPR peak of the Ag-NP structures and the PSI absorption peak in the red region, i.e., $\lambda \sim 680$ nm in Figure 2.1(a). It should be noted that the enhancement factors calculated here are conservative estimates since the presence of defects such as bow tie structures, presence of unremoved polystyrene beads, absence of Fischer pattern areas, etc. cannot be accurately accounted for. Such defects arise due to the defects in hexagonal packing of spherical beads and imperfect sonication.

The relatively lower enhancement factors of ~2.4 and ~5.8 at the 420 nm and 470 nm excitations respectively are due to the coupling between the broad Ag-NPs LSPR peak at 410 – 485 and the PSI absorption peak centered at ~450nm. Also, the enhancement factor observed at 470 nm is higher than that at 420 nm due to the relatively higher plasmon resonance at 470 nm. But, the relatively weak increase (5.8 to 6.5) in the enhancement factors while going from 470 nm to 660

nm excitation is more counter intuitive since the plasmonic peak at ~660 nm is more dominant than the peak at ~470 nm for the Ag-NPs. These discrepancies can be rationalized by the observations from past studies that under plasmonic interactions, PSI fluorescence emissions from 470 nm excitation indicate very low excitation energy loss as compared to the fluorescence energy loss pathways from 660 nm excitations[73, 77]. Specifically, plasmon-induced fluorescence enhancement studies at room temperature shows a 200-fold fluorescence enhancement for 640 nm excitation as compared to a 17-fold enhancement with 485 nm excitation[77]. In fact, the distinct blue shift in the fluorescence signature of PSI coupled with plasmonic nano-structures undergoing red light excitation (640 nm, and 680 nm) clearly indicates new excitation transfer pathways between chlorophylls[73, 77]. Hence, the many-fold fluorescence enhancement from higher energy chlorophylls which otherwise could have transferred that energy to P700 reaction center leads to significant reduction in the PSI charge separation efficiency[73, 77]. Thus, photocurrent enhancement for PSI coupled to plasmonic nanostructures is expected to be less efficient with red light excitations. In accord with these observations, Figure 2.5(b) shows that the photocurrent enhancement factor has a relatively weaker increase for the 660 nm excitation than what was expected due to the presence of a stronger plasmonic peak at 675 nm, especially when compared to the enhancement factor for the 470 nm excitation.

To substantiate our hypothesis, regular Ag nano-dot patterns (Ag-ND) were sputter coated on ITO substrates as controls with a broadband plasmonic absorption peak centered at around ~500 nm (Figure AI.2 & AI.3). Unlike the Fischer pattern studies presented earlier, here the plasmonic absorption at ~470 nm was higher than the corresponding absorption at ~660 nm for this control samples. Consequently, similar procedures as reported above for PSI immobilization, photocurrent testing and enhancement factor calculations were followed. In this case, the effective enhancement factor under the nominal excitation wavelength of 470 nm was observed to be higher (almost twice) than the corresponding value with the 660 nm excitation, thereby qualitatively corroborating our earlier hypothesis that the fluorescent emission loss pathways for 470 nm excitation is weaker than the loss pathways for 660-680 nm excitation.

In conclusion, our work here presents the first-ever experimental observation of plasmon-induced photocurrent enhancements in cyanobacterial PSI coupled to Fischer patterns of Ag-NP

structures as a result of plasmon-induced localized electric field. This was achieved by tuning the plasmonic absorption peak of Ag-NPs to the absorption peak of PSI at ~675 - 680 nm wavelengths. A large PSI photocurrent enhancement factor of ~6.5 was noted for λ=660 nm excitation of PSI assembled on Ag-NP/ITO surfaces as compared to PSI on non-plasmonic planar Ag electrodes under similar conditions. The photocurrent enhancement factors only increased slightly from the excitations at 470 nm to the excitation at 660 nm owing to the enhanced plasmon-induced fluorescence emission losses for red light excitations as compared to blue light excitations. The fundamental findings of the current work are crucial in designing rational biotic-abiotic interfaces for future bio-hybrid solar energy harvesting technologies.

Chapter 3

Broadband plasmonic photocurrent enhancement of immobilized Photosystem I on tailored arrays of Au and Ag nanodiscs

3.1 Introduction

Photosystem I (PSI) is one of the vital protein complexes architecting photosynthetic processes in plants, algae and cyanobacteria that harness solar energy and convert it to usable forms for sustaining life on this planet. PSI is a chlorophyll-rich transmembrane protein complex that drives light-activated ultrafast charge separation with ~100% internal quantum efficiency. This enables the subsequent redox-mediated unidirectional electron transport across the electron transfer chain (ETC) from the luminal (P_{700}^{+}, E_m = +490 mV) to the stromal (F_B^{-}, E_m = -530 mV) side of PSI[15, 81, 82]. In the cyanobacterium *Thermosynechococcus elongatus*, the membrane-bound trimeric PSI complex (diameter = 22 nm, thickness = 9 nm) is comprised of an intricate network of chlorophylls and carotenoids that act as light harvesting antennae while the protein conformations of the PSI act as binding blocks to maintain stability and structural integrity among all the cofactors and subunits[10, 11, 110, 111]. It is widely hypothesized that the excitation energy activated by the absorption of photons by light harvesting fluorophores is funneled to the charge separation reaction center P700 through the Forster Resonance Energy Transfer (FRET) mechanism[83]. FRET is extremely sensitive to inter-separation distances and orientations of interacting chromophores[13, 14, 95]. The remarkable photoactivated charge separation properties of PSI, active over broad blue (~ 400-450 nm) and red (~650-700 nm) bands, have resulted in a long history of intense scientific studies to understand its fundamental biophysics as well as to integrate it into bio-hybrid photochemical and optoelectronic devices[24, 47, 112, 113].

Various strategies have been employed in the past to enhance and optimize solar energy conversion pathways in PSI-based photovoltaic systems[23, 31, 32, 57, 60, 80, 90, 114]. Generally, the first step is to deposit the PSI units on a conducting substrate. Initial efforts focused on immobilizing PSI monolayers on surface-functionalized gold substrates by using solution incubation as well as electric-field-assisted methods[27]. Our group has reported on the use of controlled solution-phase experimental parameters such as PSI concentration, detergent

concentration, temperature and pH to obtain dense PSI monolayer deposition by preventing aggregation while maintaining the structural integrity of the protein[27, 28, 30]. Other efforts have included the fabrication of PSI multilayers on electrodes to enhance the optical absorption cross section and, in turn, increase the photocurrent generation efficiency[25, 31]. In line with these efforts, past studies have also attempted genetic modifications in PSI to allow for site-specific tagging that can promote preferential orientations of PSI to facilitate unidirectional flow of charge[32, 102]. In recent years, our efforts have been directed toward tailoring the PSI micro-environment by confining the protein in biomimetic synthetic lipid membranes and metal organic frameworks (MOFs) to tune and enhance its photoactivity and chemical/thermal stability[57, 59, 60]. These efforts were inspired by fundamental interest in the role of the natural thylakoid membrane confinement of the PSI in tailoring its structural stability as well as tuning its photoexcitation pathways. In fact, the focal point of recent studies has been centered around tailoring PSI charge transport properties and environmental interactions to enhance photocurrent generation efficiency and development of PSI-Si bio-hybrid optoelectronic devices[35, 46]. To this end, one might surmise that PSI assembled with plasmonic metal nanostructures might pave the way for developing fundamental understanding of plasmon-induced photocurrent enhancement from PSI and pathways for tuning the excitation energy transfer in PSI under electromagnetic confinement.

Plasmonic nanostructures are well-known to modify the fluorescence of single fluorophore molecules[67, 68, 115]. This effect has been successfully leveraged for increasing molecular fluorescence detection limits in medical diagnosis and biotechnology[69, 70]. Such efforts have also been extended toward enhanced solar energy conversion in dye sensitized solar cells[71, 72]. These studies have demonstrated that the plasmonic enhancement of optoelectronic properties is highly dependent on the spatial location of dye molecules with respect to metal surfaces[95, 116]. Further efforts at incorporating hybrid systems of Light Harvesting Complex II (LHCII) with plasmonic nanostructures in established organic photovoltaics and TiO_2 semiconductors have demonstrated enhanced optical absorption and photoconversion efficiency[117, 118]. Photocurrent enhancement was also observed in in the proton-pump photocycle of bacteriorhodopsin photosynthetic proteins integrated with plasmonic Au and Ag nanoparticles[99, 119]. In fact, a 2.5-fold enhancement in photoelectron transfer rate was reported upon integrating the Light Harvesting

Complex I (LHCI) reaction center of photosynthetic purple bacterium with rough Ag surfaces. [98] But, to the best of our knowledge, few studies have systematically investigated spatially and spectrally resolved plasmonic control of the optoelectronic properties of a supramolecular (~1068 kDa weight) multi-chromophore photoactive protein such as PSI. to this end, prior studies have shown that plasmonic nanoparticles can couple with the intrinsic light harvesting antennae in PSI to enhance the absorption of PSI-nanoparticle hybrid systems[74, 91]. Furthermore, it has also been shown that the fluorescence emission pathways and intensities in PSI can be significantly affected by plasmonic nanoparticles[73, 75-77, 100, 120]. In fact, theoretical investigations that modeled a hybrid system of PSI and spherical metal nanoparticles revealed plasmon enhanced excited electron generation in PSI that clearly suggest strategies for enhancing the photocurrent generation from such hybrid systems[78]. Inspired by these studies, our recent work reported the first experimental verification of plasmon-enhanced photocurrents from PSI, where Fischer nano-patterns of Ag nano-pyramids (Ag-NPs) were tuned to the PSI absorption peaks of ~440 nm and ~680 nm[80]. Our results from these PSI assemblies demonstrated significant photocurrent enhancement factors of ~6.5 and ~5.8 at the excitation wavelengths of ~660 nm and ~470 nm respectively. Although such studies have paved the way for future mechanistic studies of these interactions, open up the path for intriguing research in this field, our study was largely limited to ensemble plasmonic effects due to inherent NP shape/pattern defects arising from the nanosphere lithography technique used that resulted in lack of control over the spatial distribution of PSI complexes and the specific localized surface plasmon resonance (LSPR) modes that resulted in a highly conservative estimate of the ensuing photocurrent enhancement. Interestingly, other groups have made subsequent efforts at correlating plasmon enhanced photocurrents from PSI with surface plasmon generation efficiency via plasmonic nano-slits[121].

To address the obstacles to plasmonic control of PSI photoexcitation pathways, this work resorts to a rational design and controlled fabrication of plasmonic Au and Ag nanodiscs whose sizes, shapes and patterns are specifically tailored to tune their absorbance peaks. This allows us to implement spatially directed assembly of PSI complexes onto specific areas of the nanodiscs. We report a direct investigation into the specific role of tailored plasmonic resonances in tuning the photoexcitation pathways and photocurrent enhancement in PSI by using spectrally resolved excitation of PSI assembled on nanopatterned electrodes. The absorption resonances of the Au and Ag ND patterns are tuned to ~680 nm and ~565 nm respectively guided by finite difference time

domain (FDTD) modeling. FDTD modeling is also used to quantify the spatially resolved local density of states for the dipolar plasmon resonances. Nine LED light sources spanning wavelengths of ~ 395-810 nm are employed to excite the PSI site-specifically assembled on the areas of peak resonance modes around each of the Au and Ag NDs to trace the photocurrent action spectra as well as the excitation wavelength-dependent photocurrent enhancement factors. The results presented here clearly reveal the direct correlations among the excitation wavelengths, PSI absorption spectra, plasmon resonance peaks, and the ensuing action spectra for broadband photocurrent enhancement. Specifically, the spectrally resolved photo-excitation pathways in PSI are tuned with designer plasmonic interactions, thereby allowing us to enhance PSI photocurrents for green wavelengths that are otherwise attributed to the blind chlorophyll regions of the native PSI absorption spectrum.

3.2 Results & Discussion:

Au and Ag ND arrays with a 200 nm pitch and (diameter, thickness) of (124 nm, 40 nm) and (76 nm, 30nm) respectively were designed based on FDTD simulations and patterned via electron beam lithography (EBL) on ITO coated glass in order to achieve LSPR absorbance resonances at ~680 nm and 561 nm respectively (Figure AII.2). The FDTD simulations shown in Figure 3.1 illustrate the dipolar field distribution for these plasmon resonances. The experimentally synthesized AuND arrays had measured Au thickness of 40 nm (including 3 nm Cr layer) and diameter of 112 nm, resulting in an absorption resonance at ~680 nm that matches closely with the PSI absorption maxima at 678 nm (Figure 3.2). We also note the presence of a resonance at ~443 nm which incidentally matches closely with the PSI absorption maxima in the Soret region at ~439 nm. AgNDs with thickness of ~30 nm (including 3 nm Cr adhesive layer) and diameter of ~76 nm was lithographically patterned to achieve resonant absorption at ~565 nm (Figure 3.2).

The PSI had to be site-specifically immobilized on only the exposed ITO areas around the edges of the NDs to get optimal overlap with the dipolar plasmon modes illustrated in Figure 1. To achieve this, site-specific chemical grafting via systematic OH-terminated thiol functionalization (SAM) of the ITO substrates was employed prior to EBL patterning (as discussed in detail in the Experimental Section). This led to thiolation of ITO areas while the Au and Ag surfaces were not functionalized. A sonication step after the incubation of the nanopatterned substrates in PSI solution ensured the PSI monolayer assembly on the thiol-activated ITO as well

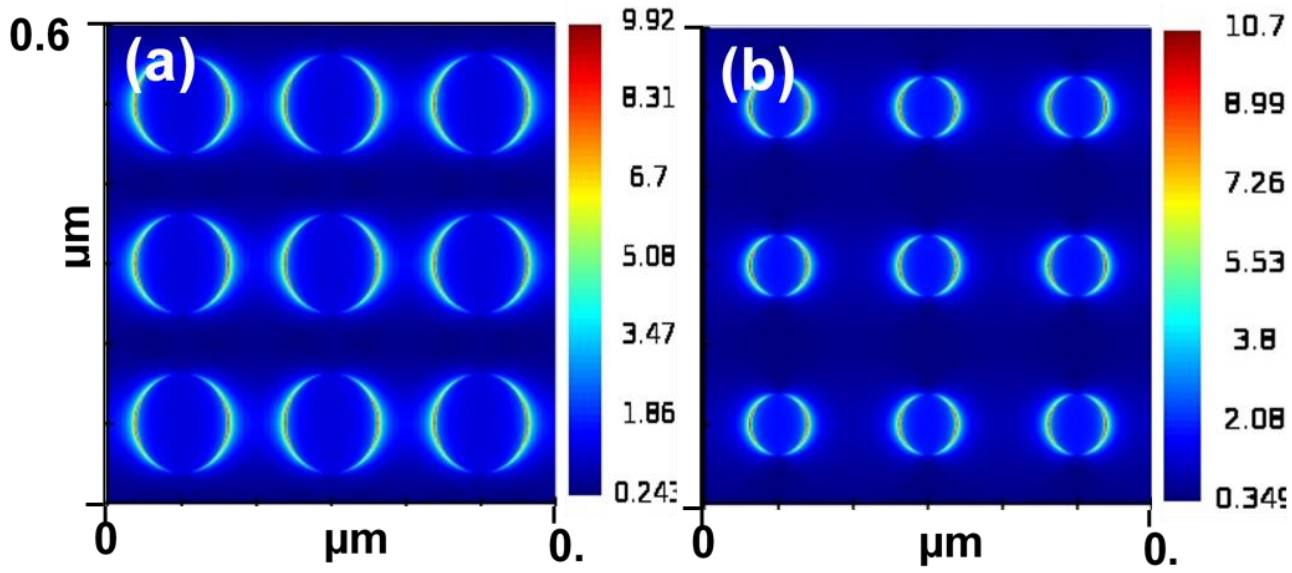

Figure 3.1 FDTD models of the 2D dipolar plasmon electric-field distribution on surface of ITO (z = 0) for (a) AuND/ITO and (b) AgND/ITO at 680 nm and 565 nm respectively.

as the removal of unbound PSI from the bare non-thiolated ND surfaces. SEM and atomic force microscopy (AFM) verified the site-specific PSI attachment. In Figure 3.3 (a-d), AFM topography images for the AuND and AgND substrates before and after the PSI deposition are shown. Topographical profiles along the labelled lines in Figures 3.3 (a) and (c) for the AuND and AgND substrates respectively without PSI immobilization reveal the roughness of the underlying ITO substrate to be under 1.4 nm. In contrast, the topography profiles for the AuND/ITO and AgND/ITO substrates coated with PSI in Figure 3.3 (b) and 3(d) respectively indicate increased roughness in the exposed ITO areas. Specifically, the height profile insets in Figure 3.3 (b) and (d) reveal densely packed ~28-35 nm in diameter and ~7-8 nm thick that correspond extremely well with the known dimensions for the PSI trimeric units and are consistent with our earlier reports on AFM circular characterizations of PSI trimers [27, 30, 90]. Also, the thicknesses for the AuNDs and AgNDs are measured to be ~43 nm and ~33 nm respectively, including the 3 nm Cr under both ND arrays. Upon comparing Figures 3.3 (e) and (f) with AFM images in Figures 3.2 (b) and

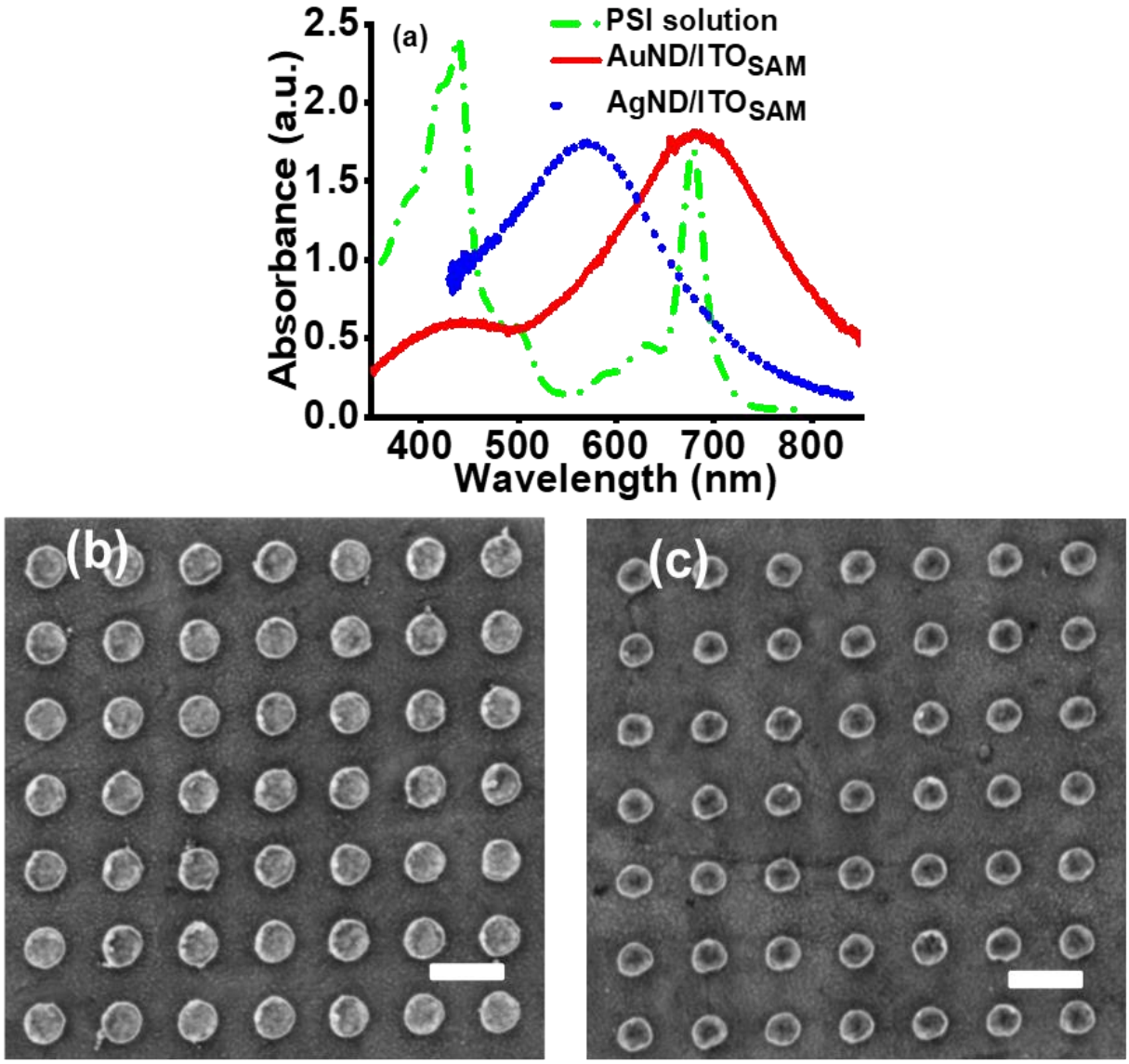

Figure 3.2 (a) Absorption spectra for bare PSI solution (gray dotted), AuND/ITO (red continuous) and AgND/ITO (blue dotted) substrates; SEM images of (b) blank AuND/ITO substrates and (c) blank AgND/ITO substrates. The white scale bar is 200 nm.

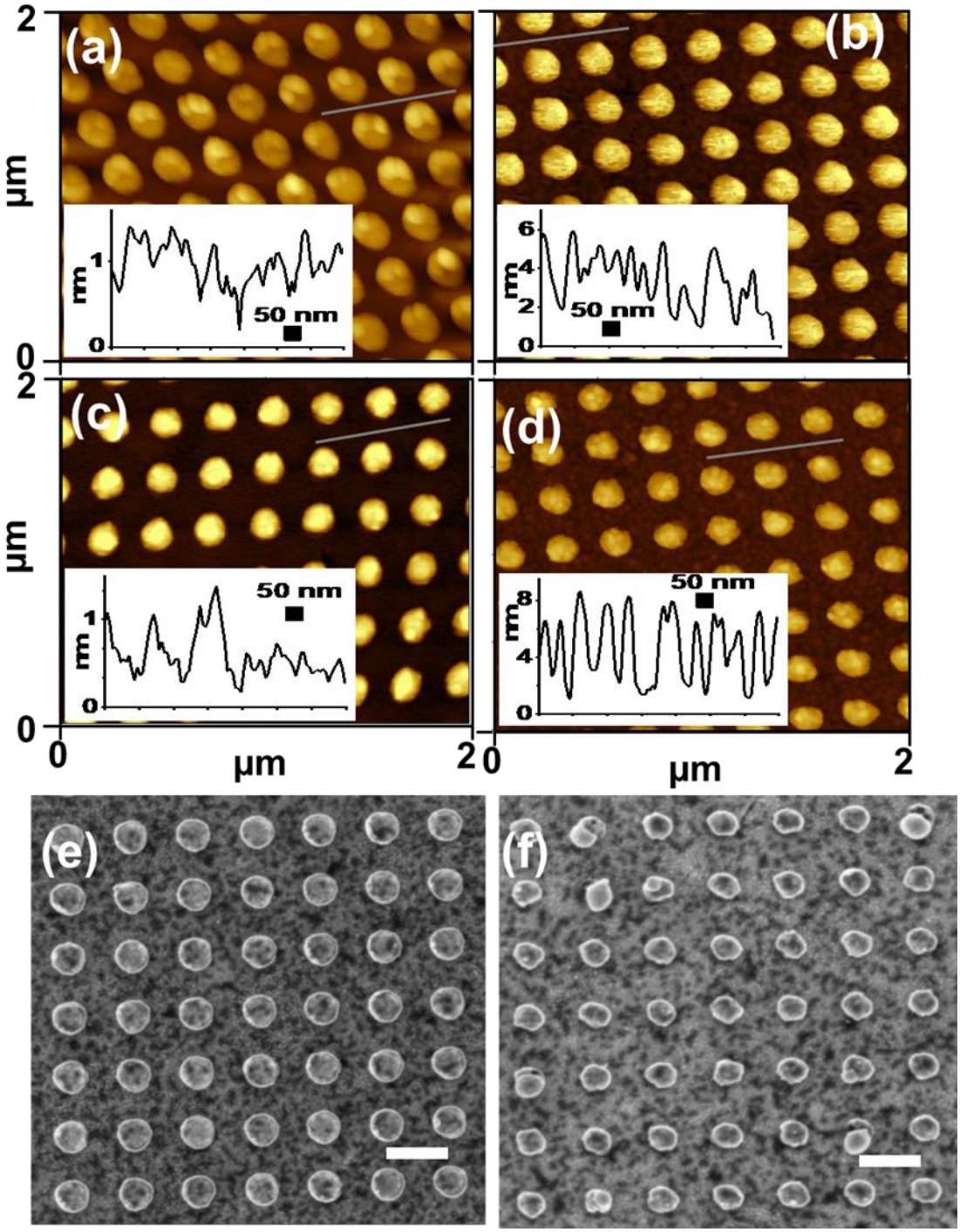

Figure 3.3 The AFM topographical images for AuND/ITOSAM substrates with (a) and without (b) PSI coatings, and AgND/ITOSAM with (b) and without (c) PSI coatings. The inset height profiles are measured along the respective lines labelled in the figures; SEM images for (e)AuND/ITOSAM and (f) AgND/ITOSAM with PSI coatings.

(d), spots the respective SEM images for the ND substrates with the PSI depositions clearly reveal the PSI assemblies as distinctive dark spots in the background ITO areas that were absent from the substrates without PSI deposition. Moreover, such distinctive dark spots are not observed on the surfaces of the Au and Ag NDs, corroborating the successful immobilization of PSI only on the exposed ITO areas around the NDs.

Figure 3.4 depicts the wavelength-specific plasmon-enhanced photocurrent measurements at nominal excitation wavelengths of 680 nm and 565 nm for the tailored AuND/ITO_{SAM} and AgND/ITO_{SAM} substrates as compared to the respective controls here. The working electrodes used are PSI/X (X= ITO_{SAM}, AuND/ITO_{SAM}, AgND/ITO_{SAM}) to measure the PSI photocurrents on the respective X substrates. The background photocurrents from the X substrates were measured as controls to account for the photocurrents from the bare substrates without PSI. Figure 3.4 (a) depicts the prototypical chronoamperometry (CA) photocurrent measurements on PSI immobilized AuND and ITO electrodes (i.e., PSI/AuND/ITO_{SAM} and PSI/ITO_{SAM}) along with the respective controls for the background photocurrents without PSI (i.e., AuND/ITO_{SAM} and ITO_{SAM}) using a 680 nm LED as the excitation light source. Similarly, Figure 3.4 (b) depicts the prototypical CA photocurrent measurements on PSI immobilized AgND and ITO electrodes (i.e., PSI/AgND/ITO_{SAM} and PSI/ITO_{SAM}) along with the respective controls for the background photocurrents without PSI (i.e., AgND/ITO_{SAM} and ITO_{SAM}) using a 565 nm LED as the excitation light source. The photocurrents measured from PSI assembled on a bare ITO substrate are used as the references throughout for estimating the plasmon enhanced photocurrents generated from the PSI assembled on the background ITO areas under the influence of the LSPR modes in PSI/AgND/ITO_{SAM} and PSI/AuND/ITO_{SAM} substrates. It should be noted that, unlike our previous work on plasmon enhanced photocurrents[80], we did not have to consider the planar Au or planar Ag electrode substrates for reference, since the PSI trimers are not directly assembled on the surfaces of the AuND or AgND. The photocurrent measurements in Figure 3.4 (a) and (b) clearly demonstrate enhanced cathodic photocurrents from the PSI coated plasmonic substrates compared to the photocurrents from either the background substrates without PSI (AgND/ITO_{SAM} and AuND/ITO_{SAM}) or the reference substrates of PSI coated ITO. The photocurrent enhancement is nearly 3 times for the PSI/AuND/ITO_{SAM} substrates as compared to the control PSI/ITO_{SAM} (see Figure 3.4 (a)). On the other hand, in the case of the PSI/AgND/ITO_{SAM} substrates, nearly 4 and

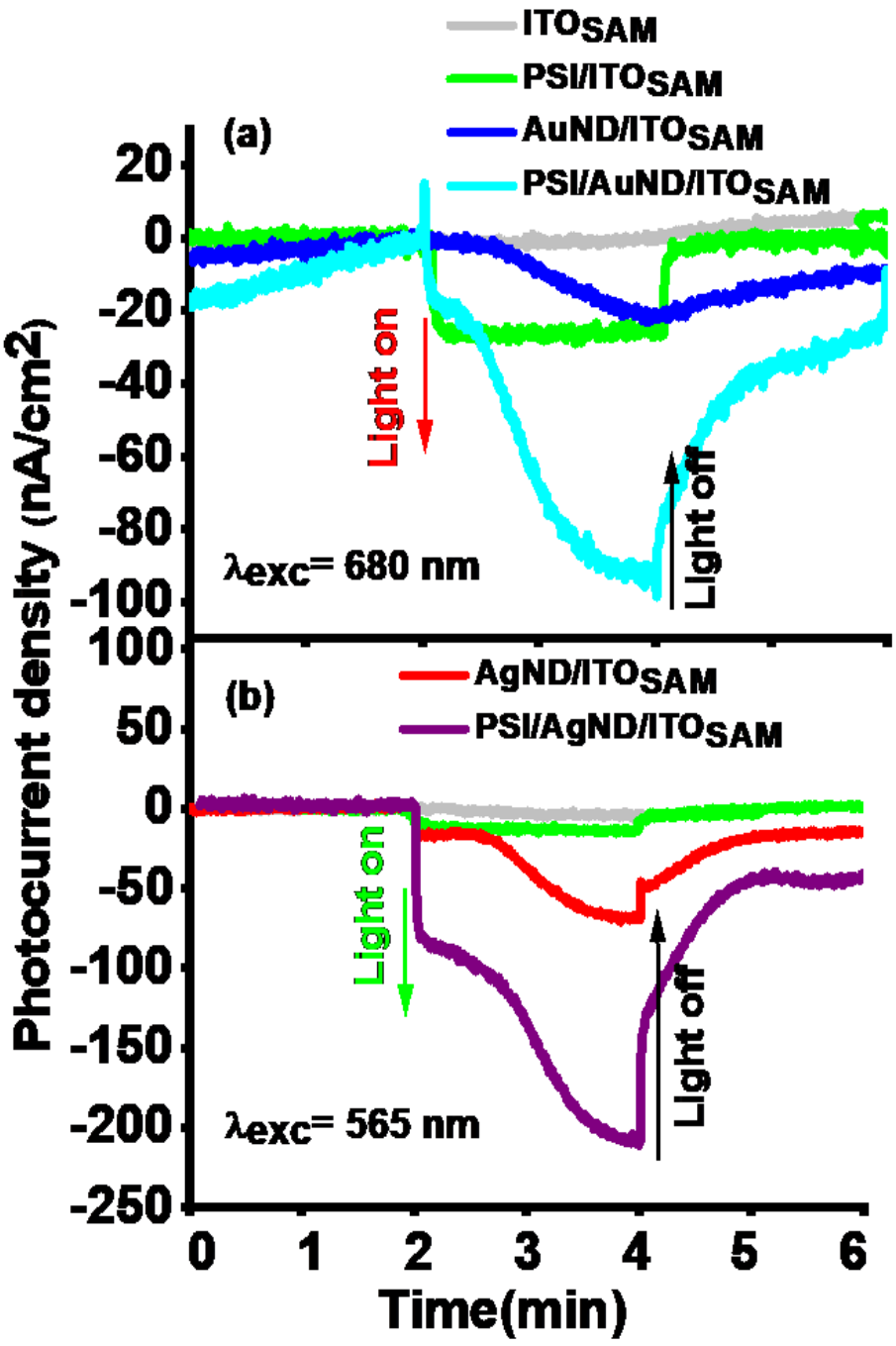

Figure 3.4 Chronoamperometric data for cathodic photocurrents measured from light on-off experiments on: (a) ITO_{SAM}, PSI/ITO_{SAM}, $AuND/ITO_{SAM}$ (controls) and $PSI/AuND/ITO_{SAM}$ (specific) at 680 nm excitation wavelength, (b) ITO_{SAM}, PSI/ITO_{SAM}, $AgND/ITO_{SAM}$ (controls) and $PSI/AgND/ITO_{SAM}$ (specific) at 565 nm excitation.

15-fold photocurrent enhancement is observed compared to the background plasmonic substrates without PSI (AgND/ITO_{SAM}) and the non-plasmonic PSI/ITO_{SAM} respectively A significant photocurrent from the background plasmonic substrate without PSI (AgND/ITO_{SAM}) was also noticed.

The enhanced photocurrent in the PSI-plasmonic nanodisc electrode substrates can be attributed to the improved excitation in PSI as a result of additional plasmon induced resonant energy transfer (PIRET) due to the strong dipole-dipole coupling between the PSI and plasmon. This can also be explained with the simple model of PSI-nanoparticle hybrid system that was established by Govorov et. al to theoretically estimate the plasmon enhanced photochemical production [78]. The enhancement was directly attributed to the plasmon enhanced fields inside the chlorophyll network. The enhancement factor P(ω) was calculated as the square of the plasmon-induced electric field enhancement. Energy transfer from PSI to metal nanoparticles that reduces the quantum yield of PSI was also considered for estimating the spectrally resolved plasmon enhanced photocurrent factors. However, this effect was determined to be minimal because charge separation at the reaction center is very fast compared to the transfer time to the metal. Since the PSI are not immobilized onto the nanodiscs, the probability of such energy losses is very low, so that the theoretical plasmon enhancement factors can be directly dependent on P(ω).

To determine the spatially and spectrally resolved theoretical photocurrent enhancement factor, FDTD simulations were carried out on the gold and silver nanodisc patterns. A 2D field and power monitor was placed at the surface of the ITO, and the spatially resolved photocurrent enhancement factor or P(ω) is plotted in Figure 3.5 at selected wavelengths of 680 nm, 440 nm and 565 nm where the highest values are observed. Depending on the location, the calculated enhancement factors reached as high as 140 and 15 for wavelengths of 680 nm and 440 nm respectively in the AuND system. For AgND patterns, the enhancement factor reached as high as 200.

Photocurrent action spectra were acquired with 9 LEDs with nominal peak wavelengths of 395, 420, 455, 470, 565, 660, 680, 730, and 810 nm. This allowed us to spectrally resolve the characteristic changes in the photocurrent and plasmon enhancement factors for both the PSI/AgND/ITO_{SAM} and the PSI/AuND/ITO_{SAM} substrates. In each case, the background photocurrents for the control substrate X (X = AuND/ITO_{SAM}; AgND/ITO_{SAM}; ITO_{SAM}) are

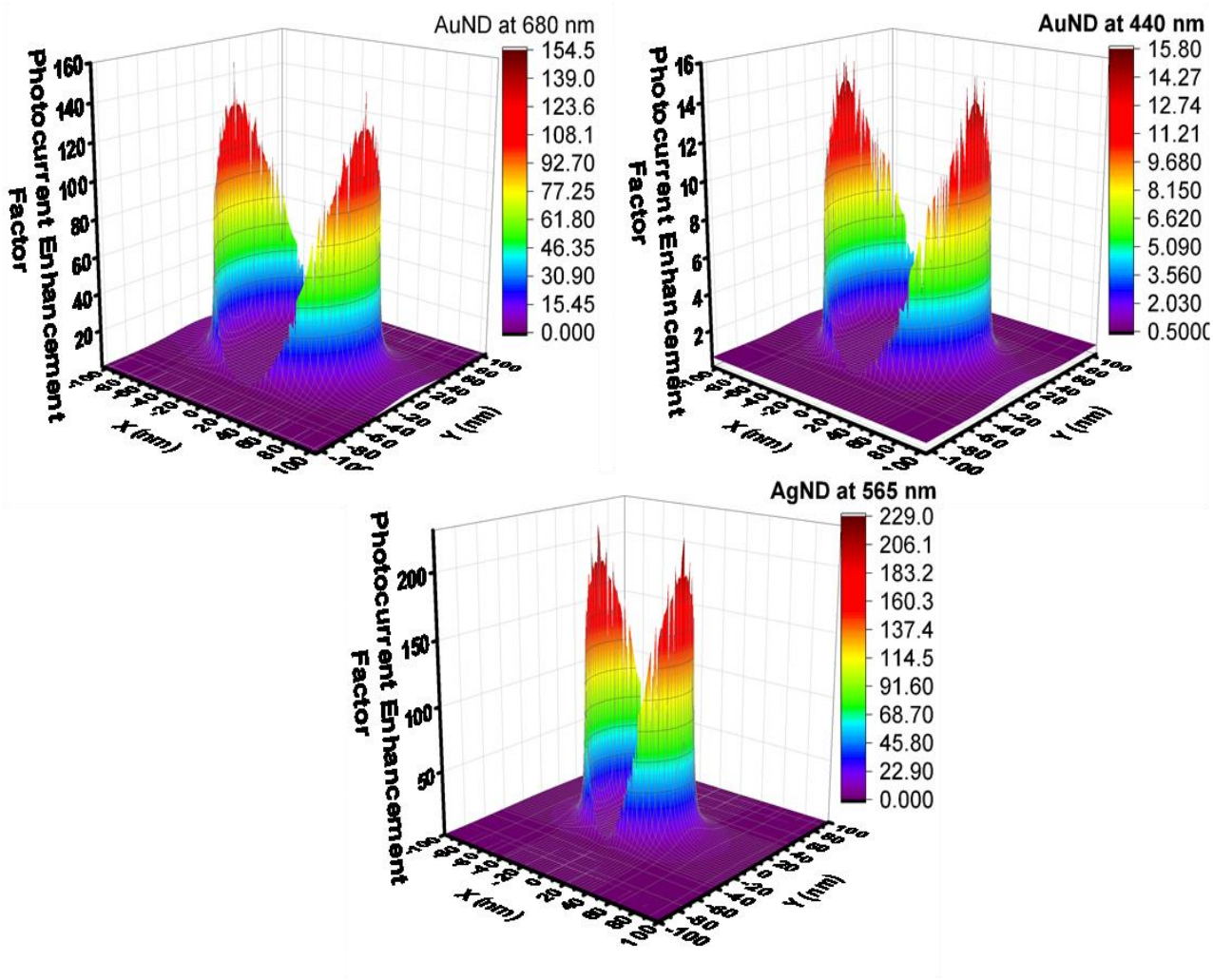

Figure 3.5 The spatially resolved FDTD simulated photocurrent enhancement factors for AuND nanopattern system at (a) 680 nm, (b) 440 nm and for AgND nanopattern system at (c) 565 nm.

subtracted from the respective PSI/X electrodes to extract the effective photocurrent contributions from the PSI assembly on the given substrate X, as shown in Figure 3.6 (a). The effective photocurrent density contributions from PSI assembled on the AuND/ITO_{SAM} when compared to the control substrate, PSI/ITO_{SAM} clearly demonstrate the photocurrent enhancement at each of the excitation wavelengths that can be directly attributed to near-field interactions between the LSPR and the PSI. A careful observation of the trends indicates that the effective photocurrent action spectra for the PSI/AuND/ITO_{SAM} and the PSI/ITO_{SAM} controls follow the characteristic PSI absorption spectrum. For both cases, the effective photocurrent density peak values traced at the excitation wavelengths of 680 nm and 455 nm closely match with the standard PSI absorption peaks at 678 nm and 439 nm respectively. Furthermore, for the ITO case, it is noted that the photocurrent density at the 455 nm excitation wavelength is higher than the photocurrent density at the 680 nm excitation, which is obviously expected considering that the characteristic PSI absorption spectrum exhibits higher absorbance for 439 nm excitation as compared to 680 nm excitation. Interestingly, this trend is not observed for the PSI/AuND/ITO_{SAM} substrates, where the photocurrent density peak at 680 nm excitation (resonant with the AuND dipolar plasmon mode) is the highest. This feature can be explained with the increased excitation energy from PIRET that is dominant at 680 nm due to the AuND dipolar resonance. Furthermore, unlike the lowest effective photocurrent densities around ~565 nm excitation for the PSI/ITO_{SAM} case (Note that PSI has the least absorption in the green region of ~530-570 nm), the PSI/AuND/ITO_{SAM} indicate the lowest effective photocurrent density at the 470 nm excitation wavelength, while displaying a significantly and unusually enhanced effective photocurrent densities in the green region for the 565 nm excitation wavelength. This characteristic enhancement of the effective photocurrent features in the green region of the spectrum coincide with the broadband plasmon absorption spectrum for the blank AuND/ITO_{SAM} substrates over the 500 – 800 nm wavelength range (see Figure 3.2 (a)).

Correspondingly, the effective photocurrent densities measured from the PSI/AgND/ITO_{SAM} substrates in Figure 3.6 (a) show significant enhancements at the excitation wavelengths ranging between 420-660 nm. It should be pointed out that unlike the PSI/AuND/ITO_{SAM} case, the PSI/AgND/ITO_{SAM} substrates exhibit characteristic photocurrent density spectra with the highest effective photocurrent densities noted at 455 nm excitation along with highly enhanced photocurrents in the green region (565 nm). As explained earlier, this

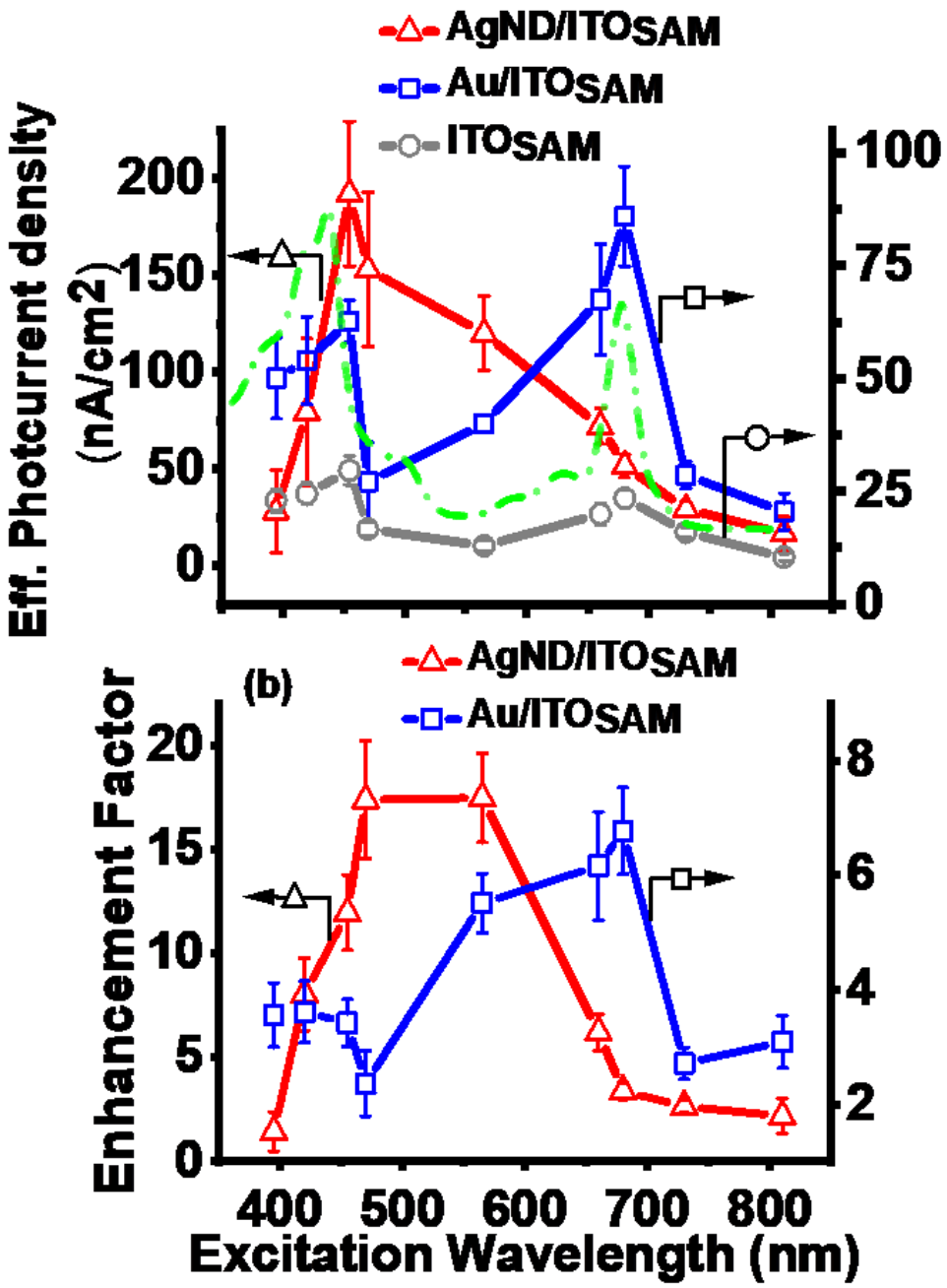

Figure 3.6 (a) Effective photocurrent (PSI/X – X) of PSI on X substrates where X=ITO_{SAM} gray, $AuND/ITO_{SAM}$, and $AgND/ITO_{SAM}$. The dash dotted green curve is the characteristic absorption of PSI for reference. (b) LSPR induced Photocurrent enhancement factors for PSI on $AuND/ITO_{SAM}$ and $AgND/ITO_{SAM}$ compared to the ITO_{SAM}.

enhancement in the green region can attributed to the broad-band strong plasmon resonance absorption for the control AgND/ITO_{SAM} substrates at ~565 nm (see Figure 3.2 (a)) that can enhance the excitation rates of the blind chlorophylls and initiate PIRET in the green region. The photocurrent enhancement in this case is more pronounced than that for the earlier PSI/AuND/ITO_{SAM} case that can be readily explained by the higher relative absorbance noted for the AgND/ITO_{SAM} substrates in the green region (~500-570 nm) as shown in Figure 3.2 (a). Since the background photocurrent of the plasmonic nanostructures before PSI coating is accounted for in the effective photocurrents reported here, this provides direct evidence of the broad-band plasmonic enhancements of the light harvesting and energy transfer processes by the otherwise blind chlorophylls in the green region. These observations are also in agreement with previous works reporting on the phenomenon of plasmon-enhanced activation of blind chlorophylls in PSI, where similar conclusions were drawn by using indirect evidence from fluorescence intensity and decay rate measurements[122]. Thus, in the case of the PSI/AgND/ITO_{SAM} substrates, the consistent and broad increase in the effective photocurrent densities as excitation wavelengths decreased from 810 nm to 455 nm is reflective of the strong influence of its corresponding plasmon resonance absorption spectrum (Figure 3.2 (a)) where broadband enhancements are observed over the 450-750 nm spectrum.

Finally, the photocurrent enhancement factors are determined based on the effective photocurrents for PSI on the respective X substrates. The PSI number density (# of PSI trimeric units per unit area) on ITO is kept constant on all three PSI coated electrode substrates since the PSI was immobilized only on the functionalized ITO surface. Here, the photocurrent enhancement factor is defined as the ratio of effective photocurrents in PSI on the Ag or AuND/ ITO_{SAM} to the effective photocurrents from PSI on the non-plasmonic ITO_{SAM} substrates. It needs to be mentioned here that the effective photocurrent densities (nA/cm^2) reported in Figures 3.6 (a) was based on the total exposed ITO_{SAM} working area for the respective electrodes X. For the ITO_{SAM} electrodes without the ND patterns, the total working area is the exposed ITO area (30.19 mm^2) that is calculated based on the inner diameter of the o-ring that was placed to immobilize the working electrode substrate during our electrochemistry measurements. But, for the plasmonic AuND/ITO_{SAM} and AgND/ITO_{SAM} electrode substrates, the effective exposed ITO_{SAM} areas are subsequently reduced to 25.362 mm^2 and 28.377 mm^2 respectively, i.e., by subtracting the areas covered by the NDs since no PSI is immobilized on them. Also, it should be noted that the

photocurrent contributions from the bare NDs without the PSI coatings on each of the nanopatterned substrates was already subtracted when calculating the effective photocurrent densities here. Furthermore, it needs to be mentioned that the nanodisc patterned array size is only within the 4 mm x 4 mm where the plasmon field is located, whereas the electrochemical working area is a circular spot due to the design of electrochemical cell (Figure AII.1). As described in the Appendix II, there is significant portion of ITO area (14.19 mm^2) outside the nanopatterned array in which the immobilized PSI is not under the plasmon field. After subtracting the photocurrent contribution from these PSI, the effective photocurrent density values representing the plasmon enhanced photocurrent of PSI located in plasmon field for AuND/ITO_{SAM} and AgND/ITO_{SAM} are utilized for estimating the photocurrent enhancement factors.

Based on these calculations, the plasmon-induced photocurrent enhancement factors from PSI with the AuNDs and AgNDs were calculated at each of the 9 excitation wavelengths. As shown in Figure 3.6 (b), the two highest enhancement factors of ~6.8 and 6.1 are observed at the excitation wavelengths of 680 nm and 660 nm respectively for the PSI on AuND/ITO_{SAM} substrate. Moreover, the characteristic enhancement factor spectra across the 470-730 nm wavelength range clearly correspond to the broad band absorbance of the AuND/ITO in the region (refer to Figure 3.2 (a)). In fact, the relatively small photocurrent enhancement factor bands across the 395-470 nm range also coincide very well with the smaller absorbance spectra bands for the AuND/ITO in the 350-470 nm window (see Figure 3.2 (a)). The blind chlorophyll activations in the green region, as described earlier, is clearly supported by the significant enhancement factor of ~5.5 observed at the 565 nm excitation. Unlike the effective photocurrent spectra reported in Figure 3.6 (a) the characteristic enhancement factor spectrum is more effective in mapping the stark resemblance with the plasmon resonance absorbance spectrum in Figure 3.2 (a) for the AuNDs. On the other hand, for the PSI on AgND/ITO_{SAM} case, a huge enhancement factor of ~17.5 is observed at the excitation wavelength of 565 nm. This is corroborated by the strong plasmon resonance absorption peak in the green region at ~561 nm wavelength for the AgNDs see Figure 3.2 (a)). Additionally, the broad-band photocurrent enhancement factors spanning the 450-650 nm wavelength range agrees extremely well with the single peak broadband absorbance mode in the same region for the AgND/ITO. This, in turn, confirms that the characteristic trends for the plasmon-induced enhancement factor spectrum closely follows the plasmon resonance absorbance spectrum of the respective ND substrates. However, the fact that the ~470 nm excitation wavelength resulted in an

enhancement factor of ~17.4, even though the plasmon resonance absorption at 470 nm was lower as compared to the absorbance at 565 nm (Figure 3.2 (a)) is counter intuitive. What is intriguing is that similar behavior was also observed in our previous work reporting PSI interactions with Ag nanopyramids, where the plasmon-induced photocurrent enhancement factor at 470 nm excitation was found to be comparable with the enhancement factor at 660 nm excitation even though the resonance absorption was lower at 470 nm[80]. It is known that the 470 nm excitation specifically activates the carotenoids (Cars) in PSI since the Chlorophyll a (Chla) absorptions are the lowest at ~470 nm[123]. To this end, a previous study had reported ~17 fold enhancement in the plasmon-induced fluorescence from PSI due to the carotenoid activations at 485 nm as compared to ~114 and ~201-fold enhancements in fluorescence for 580 and 640 nm excitations[77]. Here the relatively lower plasmon enhanced emission with carotenoid activation is suggesting relatively lower excitation energy losses. Considering these observations our results here corroborate that effective carotenoid activations can result in reduced pathways for radiative excitation energy losses and hence, enhanced excitation rates in PSI. This can allow the system to generate plasmon-induced photocurrents relatively more efficiently when the carotenoid excitation pathway is substantially activated by the plasmon resonance absorptions (beyond the PSI absorbance) as compared to the Chla activations at the higher wavelengths.

A critical observation here is that, in spite of the PSI absorption being minimal in the green region of the absorption spectra, a significant photocurrent enhancement factors of ~5.5 is observed at the excitation wavelengths 565 nm for the AuNDs, whereas a significantly larger enhancement factor of ~17.5 is observed for the excitation at 565nm for the AgNDs which, incidentally, also had the maximum plasmon resonance absorption peak at ~560 nm wavelength. In fact, unlike the previous study[122] where the plasmon enhanced blind chlorophyll absorption was suggested specifically for PSI with uniform orientation , we find here the uniform PSI orientations in these systems are not necessary for such blind chlorophyll's enhanced activation. Also, despite the lower light trapping capacities for the AgND/ITO substrates due to their smaller ND sizes compared to the AuND/ITO samples, the effective photocurrents are higher for the PSI/AgND/ITO_{SAM} plasmonic substrates. Such behavior was also reported for LHCII systems combined with TiO_2 - plasmonic Ag and Au nanoparticles, where the PSI photocurrent generation due to coupling with Ag nanoplates and nanospheres had outperformed those from Au nanospheres despite the latter's higher absorption cross-sections[118]. The implications of tailoring such

broadband photocurrent enhancement from PSI assembled on spatially resolved and spectrally tuned plasmonic modes of nanopatterned substrates can be enormous when it comes to architecting natural photosynthetic systems for bio-inspired photo-electrochemical devices.

Furthermore, it is evident from Figure 3.5 that every PSI immobilized on the $AgND/ITO_{SAM}$ or $AuND/ITO_{SAM}$ substrates does not interact equally with the plasmonic near-field (refer to Figure 1). While our approach has successfully confined the PSI in-plane with the plasmonic nanodiscs, designs with improved fill factors will be essential future device designs. In principle, devices in which PSI is densely packed inside the plasmonic mode volume, with no PSI outside the mode volume, could offer two orders of magnitude further enhancement in photocurrent.

3.3 Conclusion:

Our experimental results indicate substantial photocurrent enhancement for PSI spatially assembled in the LSPR mode volume around AuNDs and AgNDs. Action spectra for the plasmon-induced photocurrent enhancement factors measured by using 9 LED light sources over a wavelength range of 395 nm – 810 nm clearly reveals that the characteristic trend of the spectra strongly follows the absorption spectra for the plasmonic AuND and AgND substrates. We report strong enhancement factors of ~17.5 and ~5.5 at the green light excitation of 565 nm for the AgNDs and AuNDs respectively, thereby indicating the unique activation of the blind chlorophylls under the influence of LSPR electric fields. Specifically, an intriguing observation is that the excitation wavelengths of 470 nm and ~565 nm both generated equal enhancement factor of ~17.5 for the $PSI/AgND/ITO_{SAM}$ samples, even though the AgND resonance intensity at 470 nm is lower than that at 565 nm. This observation paves the path for tuning the carotenoid excitation at ~470 nm to promote more efficient LSPR induced photocurrent enhancements. To the best of our knowledge, such detailed and systematic studies have heretofore not been carried out to investigate the direct interactions of spatially resolved and spectrally tuned LSPR modes with PSIs to modify their photoexcitation pathways and, enhance the ensuing photocurrent generations. The fundamental findings of the current work are crucial in designing rational biotic-abiotic interfaces for future bio-hybrid solar energy harvesting technologies.

3.4 Methods:

Fabrication of AuND and AgND on ITO substrates using EBL technique

Commercial ITO coated sodium lime glass substrates (NANOCS: IT100-111-25) were cut into 1inch x 1inch sizes, cleaned in RCA with 5:1:1 volume fractions of H_2O:30% NH_4OH:30% H_2O_2, and sonicated for 15 minutes to remove organic residues. The substrates were further sonicated in DI water for 10 mins. All solvent and washing agents (NH_4OH, H_2O_2) were purchased from Fisher Chemicals. The cleaned ITO slides were thiolated by immersing them in 7mM 4-mercapto-1-butanol (obtained from Sigma-Aldrich) solution in ethanol for 7 days under N_2 environment at room temperature. Subsequently, the slides were thoroughly rinsed with ethanol and sonicated in isopropanol for 10 min to remove any unbound thiol molecules. Following this procedure, the thiolated SAM/ITO slides were spin coated with PMMA495A at 1000 rpm for 45 seconds and treated on a hot plate at 180ºC for 2 mins. Subsequently, the slides were patterned by EBL (JEOL JBX-9300FS) with a 100kV electron beam energy and 2 nA beam current for custom pattern writing. The resist was developed by immersing in MIBK:IPA (1:3) solvent for 1 min. Subsequently, they were plasma etched for 6 sec. A 3 nm thick Cr and subsequent 40 nm gold or 30 nm silver thin film was deposited using electron beam physical vapor deposition (Thermionics VE-240). Finally, the slides were was sonicated in Acetone for 5 min to remove the PMMA resist along with the metal deposited from the unwritten regions. The prepared AuNDs or AgNDs on ITO were thoroughly rinsed with isopropanol and subsequently dried with nitrogen.

Immobilization of PSI on ITO, AuND/ITO and AgND/ITO substrates

The details of the extraction and purification of the trimeric PSI complex from the grown thermophilic cyanobacterium *Thermosynechococcus elongatus* cells are provided elsewhere.[57] For PSI immobilization, the as prepared SAM/AuND/ITO and SAM/AgND/ITO substrates (thiolated on ITO areas) from the EBL procedure were immersed in 0.013 μM PSI solution with 0.02% w/v n-dodecyl-β-D-maltoside surfactant and 200 mM phosphate buffer solution for 24 hours in dark at room temperature. To prepare non-plasmonic PSI/SAM/ITO slides, the thiolated ITO slides were immersed in the PSI solution under similar conditions. Finally, the PSI/SAM/ITO, PSI/SAM/AuND/ITO and PSI/SAM/AgND/ITO substrates were sonicated for 10 min in DI water and dried under pressurized N_2.

Imaging with SEM and AFM

A Zeiss Merlin SEM with accelerating voltage of 1kV was used to image the SAM/AuND/ITO and SAM/AgND/ITO electrode surface with and without PSI immobilization. All surface topography images were collected on an NT-MDT AFM in the tapping mode using Si cantilever tips compatible with softer biological materials (NT-MDT; Model: NSG03). The tip had a force constant of 0.35-6.1 N/m along with a resonant frequency of 90 kHz.

Absorption measurements:

Plasmonic resonance absorbance measurements were obtained via optical transmission spectroscopy on the AuND/ITO and AgND/ITO electrodes by using an HR2000 + ES spectrometer from Ocean Optics. The measurements were performed when the substrates were covered with water. PSI spectral absorbance data was obtained on BioTek Synergy H1 well plate reader at room temperature.

Electrochemistry Measurements

All CA measurements were carried out with an electrochemistry set-up using a potentiostat from Bio-Logic (Model: SP-300) and performed in custom built standard 3-electrode electrochemical cell where ITO, AuND/ITO, and AgND/ITO substrates were used as the working electrodes, Pt wire as counter electrode and sat. calomel electrode (sat. KCl) as the reference electrode (BAS Inc.; Model: EF-1352). 2 mM aqueous methyl viologen was used as the soluble electron scavenger. The 9 LEDs purchased from Thorlabs with the nominal wavelengths of 395 nm, 420 nm, 455 nm, 470 nm, 565 nm, 660 nm, 680 nm, 730 nm and 810 nm (model: M395L4, M420L3, M455L4, M470L3, M565L3, M660L4, M680L4, M730L5 and M810L3) were operated with a power density of 25mW/cm^2 reaching the working area when the solution in the cell was absent. The LED power densities were measured using a power meter purchased from Thorlabs (Model: S120VC). All chronoamperometric measurements were performed at open circuit voltage with the on/off light cycles being operated with 2 minutes intervals each and repeated for at least 3 cycles. It was repeated at least 3 times by preparing fresh substrates for each case. The results reported are based on averaging the system response over repeated 3 cycles for 3 repeated measurements.

FDTD simulation:

The FDTD simulations were carried out in a FDTD solver software (Lumerical FDTD Solutions). The 3D model of the periodic gold and silver nanodisc array was arranged with the 200 nm pitch on a 0.6 x 0.6 x 1 μm^3 glass slide coated with a 72 nm thick ITO layer. A plane wave was

used to illuminate the substrate from top towards negative z-direction. Anti-symmetric and symmetric boundary conditions were used in x- and y- directions respectively while Perfectly Matched Layers (PML) were used in the z-direction. A frequency domain power monitor was placed at 300 nm from the top ITO layer towards negative z-direction to measure the absorbance. 2D Z-normal frequency domain profile monitor was placed on the surface of the ITO to image the localized electric field. The minimum mesh step size was 0.25 nm with a mesh accuracy of 4. The permittivity model of Au (Gold)-CRC was used for AuND patterns while the Ag (Silver)-Palik (0-2 μm) with 4 coefficients was used for AgND. The Cr (Chromium)-Palik permittivity model was used for Cr layer in both AgND and AuND patterns.

Chapter 4

Evidence for Alterations in the Photoexcitation Pathways in Cyanobacterial Photosystem I (PSI) Confined in Synthetic Membranes

4.1 Introduction

Photosystem I (PSI) is one of the primary biomolecular machines that acts as a biological photodiode in driving light-activated charge separation and electron transport during natural oxygenic photosynthetic process to achieve solar to electrochemical energy conversions[4]. PSI is a chlorophyll-rich transmembrane protein complex that exists in the thylakoid membrane of chloroplasts in plants and cyanobacteria. Specifically, membrane bound PSI exists in trimeric form and weighs 1068 kDa in the cyanobacterium *Thermosynechococcus elongatus*. *(T. elongatus)*[110, 111]. Detailed X-ray crystallography studies [11] have revealed that each monomer of the trimeric PSI comprises 12 protein subunits, 96 chlorophylls, 2 phylloquinone, 3 Fe_4S_4 clusters, 22 carotenoids, and 4 lipids. The protein subunits function as binding blocks to stabilize all the cofactors and maintain structural integrity. The conserved coordination among antenna chlorophyll molecules in PsaA and PsaB subunits in PSI suggest that protein-Chla interactions fine-tune the functionality of these cofactors. An Electron Transport Chain (ETC), with 3 chlorophyll pairs, 2 phylloquinone and 3 Fe_4S_4 clusters, play a vital role in initiating charge separation at the primary chlorophyll pair P700 with ~100% internal quantum efficiency[81, 82, 111]. The 90-chlorophyll a (Chla) molecules and 22 carotenoids (Cars) act as light-harvesting antenna systems. It is largely posited that, upon photons hitting the antenna system, excitation energy is funneled to the P700 through singlet-singlet energy transfer among neighboring chromophores via Forster Resonant Energy Transfer (FRET) process that can be extremely sensitive to the molecular arrangements of the interacting chromophores[12-14]. The Cars harvest light in the 450 - 570 nm region where Chla absorptions are minimal, and enable photoprotection by quenching the excited Chla triplet states to prevent the formation of toxic singlet oxygen as powerful oxidizing agents[124, 125]. The Cars also undergo Van der Waals interactions with 60 Chla head groups that facilitate efficient Cars to Chla energy transfers. And finally, the carotenoids

ensure the structural stabilization of the protein through strong π-π stacking and CH-π interactions that allows strong binding of the pigment-protein complexes[126].

The structural robustness and remarkable photoactivated charge separation properties of PSI, active over ~53% of the solar spectrum, have resulted in extensive scientific studies to understand its fundamental biophysics and integrate it into bio-hybrid optoelectronic devices.[24, 47, 112, 113] But the first step towards such device fabrication requires rational strategies to immobilize PSIs onto conducting substrates that can work as photoanodes in a photoelectrochemical (PEC) cell. To this end, a flurry of research in recent years have constructed PSI-based bio-hybrid PEC devices by interfacing PSI with conductive materials[127] such as gold electrodes,[78, 90, 128-130] carbon nanotubes,[36, 40, 131] metal oxide nanowires,[132] metal nanostructures,[75, 80, 133] silicon, graphene or semiconductor substrates[35-37, 46, 88, 131, 134-138] as well as, by wiring genetically mutated PSI to electrodes.[23, 139-142]Our group's earlier works with PSI had also investigated PSI assembly dynamics and the corresponding charge transport processes by using solution-phase colloidal chemistry [143] and electric field assisted directed assembly to achieve dense, uniform PSI monolayers with preferential orientations on thiol-activated electrodes.[27, 90, 128] Despite the insights gained from these works, the relatively poor photocurrent generations from these systems were largely attributed by us to the weak optical absorption of PSI monolayer (~0.34% at 680 nm)[113] as well as loss of PSI structure and functionality outside its natural membrane housing. Here, one cannot ignore the fact that the unique architecture of the transmembrane PSI, both internally with unidirectional electron transfer and externally with a hydrophobic toroidal belt that interfaces with the natural membrane, demands special care in optimizing oriented PSI organization in suitably designed biotic-abiotic interfaces.

To mitigate these problems, various research groups have pursued multi-layer PSI assemblies on conducting substrates [37, 39, 42, 144] and various constructs such as mesoporous electrodes,[88] hydrogels,[145] conductive polymers,[146-148] polymer micro-particles,[149] and DNA binders with complementary enzymes[33] to design suitable platforms for stabilizing PSI thin films and facilitating efficient charge transport. Our own curiosity in tailoring optimal biotic-abiotic environments for PSI have led us to encapsulate PSI trimers in chemically protective nano porous metal organic frameworks (ZIF-8)[57], MOF-derived conductive charge transfer salt matrices[150], as well as assemble PSI on plasmonic Ag-nanopyramid (Ag-NP) structures[80].

Each of cases demonstrated unique photo response shifts for PSI absorption and fluorescence, and/or, significantly high photocurrent enhancements. The fact that different PSI environments could alter its optical and PEC responses was perplexing and yet, a clear sign that PSI microenvironments can affect its excitation energy transfer pathways. One needs to note that in all these works, the PSIs were devoid of their natural thylakoid membrane housing that often results in non-native conformational changes and alter membrane protein functionalities in undesirable ways[54-56]. In fact, none of these engineering constructs could unleash the full potential of photocurrent generations expected from a ~100% QE photon-to-electrochemical energy conversion promises for natural membrane bound PSI.

To address the challenges for PSI functionality under non-native microenvironments, it becomes imperative to gain mechanistic insights into the dynamic functional role of membrane confinements, beyond being the structural scaffold, in tailoring photoexcitation/dissipation pathways and conformational changes in PSI. To this end, past studies using incubated mixtures of phosphatidylglycerol (PG) or phosphatidylcholine (PC) based biomimetic lipid membranes and eukaryotic PSIs have observed membrane-induced small changes in spectroscopic properties, thereby indicating conformational changes in both the PSI core complex and peripheral antenna complex LHCI.[151, 152] However, the protein reconstitution methods in these studies did not guarantee complete lipid membrane encapsulation of PSI without being also physisorbed onto the liposome surfaces. Recent efforts by our group have specifically investigated the optical and PEC properties of PSI-proteoliposomes successfully reconstituted in biomimetic DPhPG (1,2-diphytanoyl-sn-glycero-3-phospho-(1´-rac-glycerol)) lipid bilayers via detergent-mediated liposome solubilization and size-exclusion chromatography (SEC).[79, 153-155] Our choice of the lipid was driven by the large negatively charged PG contents in natural PSI thylakoid membranes. Here, the successful fabrication of pure PSI-proteoliposomes was confirmed through systematic AFM topology and force spectroscopy characterizations coupled with cryo-TEM imaging. Interestingly, our results indicated a 4-fold photocurrent enhancements from PSI-confined supported lipid bilayers as compared to the unconfined PSIs[79] that could be attributed to better protein orientations, conformational changes, and/or coherent interactions among PSI chromophores architected by the membrane environments. However, since mere orientations cannot explain such large photocurrent enhancements, we posit that conformational and structural changes in PSI in conjunction with altered protein-membrane interaction dynamics could have

played major roles in tuning the photocurrent responses which, in turn, itself becomes a critical area of investigation. Here it needs to be mentioned that a recent investigation on Light-Harvesting Complex II (LHC-II) embedded in near-native discoidal lipid membranes has specifically reported membrane confinement induced conformational changes to carotenoids that, in turn, was hypothesized to control the balance between enhanced excess energy dissipation and light-harvesting during the EET process in PSI [156]. The significance of biomimetic microenvironments was also highlighted by enhanced photocurrents from PSI confined in hybrid lipid bilayer designs as well as conjugated oligoelectrolytes or 3D structures of cytochrome c and DNA molecules[33, 157]. Such observations raise an interesting question: *How does the light-activated energy transduction pathways in PSI get affected by PSI micro-environment (bath) properties that can put the chromophore-chromophore interactions competing with the chromophore-bath interactions?*

In our effort to gain fundamental insights into the role of protein microenvironment alterations in regulating energy transport and dissipation mechanisms in membrane-bound PSI, we present here a series of systematic spectroscopic studies on the conformational, structural and spectral property changes induced in PSIs reconstituted in biomimetic lipid membranes. For the sake of comparisons, PSIs are reconstituted in two different lipid systems namely, anionic DPhPG and neutral DPhPC (1,2-diphytanoyl-sn-glycero-3-phosphocholine) and benchmarked against unconfined PSIs stabilized in detergents as controls. The effective alterations in the PSI structure-property relations are inferred through a series of Circular Dichroism (CD) spectroscopy coupled with absorption and fluorescence measurements. This work provides evidence for alterations in the inter-chromophore, chromophore-carotenoid interactions, and carotenoid response behaviors in PSI under lipid confinements that can tune their photoactivated EET pathways by regulating the energy dissipation mechanisms. In a broader context, the study also provides the foundations for designing tailored lipid membrane scaffolds with specific ionic charge and stiffnesses that can architect favorable functionalities in reconstituted photosynthetic protein complexes through enhanced light harvesting properties, altered protein secondary structures, and improved excitation pathways.

4.2 Materials and Methods:

Materials:

Dibasic (Na_2HPO_4) and monobasic (NaH_2PO_4) sodium phosphate with >99% assay was purchased from Fisher Scientific to prepare the 200 mM Na-Phosphate aqueous buffer solution with pH = 7. All aqueous solutions were prepared using ultrapure de-ionized (D.I.) water with a resistivity of 18.2 MΩ cm at 25 ^{0}C (Millipore, Billerica, MA). Triton X-100 (10 % w/v aqueous solution) surfactant was purchased from Anatrace. 1,2-diphytanoyl-sn-glycero-3-phosphocholine (DPhPC) and 1,2-diphytanoyl-sn-glycero-3-phospho-(1′-rac-glycerol) (DPhPG) was purchased as lyophilized powder from Avanti Polar Lipids, Inc.

Methods:

Growth of T. elongatus and preparation of PSI: The thermophilic cyanobacterium Thermosynechococcus elongatus (T. elongatus) BP-1 was grown and extracted from thylakoids according to previously described methods[27]. The details of the extraction and purification of the trimeric PSI complex from the grown T. elongatus cells are provided elsewhere[158], with few changes mentioned previously[57]. The concentration of PSI trimers in the final stock solution is estimated to be 54.0 x 10^{-6} mol L^{-1}. PSI trimers were stored in aliquots of 100 µl at -80 ^{0}C for future use.

Liposome preparation: First, 4 mg ml^{-1} lipid suspensions were prepared in 200 mM Na-phosphate (pH = 7) buffer. Second, it underwent 3-4 freeze-thaw cycles to form multilamellar liposomes. Third, these suspensions extruded through a 100 nm pore size filter using a NanoSizer Extrusion Kit (T&T Scientific) to form unilamellar vesicles at room temperature. The large unilamellar vesicle sizes of ~100 nm confirmed via dynamic light scattering (DLS) measurements. Further details regarding the lipid vesicle preparations can be found in previous studies [159].

Reconstitution of PSI: The detailed procedure for the detergent mediated protein reconstitution can be found in our previously published articles [59, 60]. First, the prototypical non-ionic detergent Triton X-100 (TX-100) was added to preformed DPhPG liposomes (4 mg ml^{-1}) such that the triton concentration in the liposome to be 12mM. The solution was equilibrated for 60 min, then mixed with solubilized 2µM PSI solution containing 2CMC TX-100 and 200 mM Na-phosphate buffer (pH 7.0). Afterward, the mixture was incubated for 30 min at room temperature under gentle agitation. For PSI reconstitution, TX-100 was slowly removed using bio beads by a three-step procedure. The first step was the addition of 15 mg bio-beads per milligram

of TX-100 and incubation for 1 hour at room temperature under gentle agitation. A similar amount of bio beads was added in the second step and incubated for 12 hours at 4 ^{0}C. Finally, another batch of a similar amount of bio-beads was added and incubated for 1 hour at room temperature. Then, the bio beads were removed, and the solution was undergone through size-exclusion chromatography to extract only PSI reconstituted proteoliposomes. In the case of DPhPC proteoliposomes, 2 mg ml^{-1} liposome concentration and 20 mM of Na-Phosphate buffer were used while following a similar procedure as DPhPG proteoliposomes.

Size-exclusion chromatography (SEC): SEC separation was carried out using a Sephacryl S-400 column attached to an AKTA purifier (GE). After the detergent removal step, the 200 µl of the PSI-lipid sample was loaded into the SEC at a flow rate of 0.5 ml min^{-1}. The sample elution was monitored by optimal wavelength for liposome and PSI absorbance at 540 and 680 nm.

Preparation of PSI-proteoliposome coated ITO/glass substrates: Commercial 50-80 nm thick ITO coated sodium lime glass substrates (NANOCS: IT100-111-25) cut into 1-inch x 1-inch size were first sonicated in 2-propanol for 10 minutes. The ITO/glass substrate was thiolated by immersing it in 5 mM 4-mercapto-1-butanol (C4) for 7 days under N_2 environment at room temperature. The thiolated substrates(C4/ITO) were sonicated in 2-propanol for 10 minutes and dried under N_2 stream. 150 µl of PSI-proteoliposomes was drop casted on the thiolated ITO/glass substrate and incubated for 1 hour at 45 ^{0}C. Then, the substrate was left at room temperature to cool for 1 hour. The assembled supported bilayers of PSI onto the thiolated ITO was washed several times with de-ionized water. The PSI coated C4/ITO substrates was also prepared as per the procedure mentioned in Pamu et. al. [80].

Photocurrent measurements: The photocurrent measurements were carried out with a photoelectrochemical setup using a potentiostat from Bio-Logic (model SP-300) and the measurements were performed in a custom-built standard three-electrode electrochemical cell where PSI-proteoliposome coated ITO/glass substrate as working electrode, Pt wire as counter electrode and Ag/AgCl as the reference electrode (BAS Inc.: model MF-2052). The iodine mixture with 50 µM of I_2 (Fisher Chemical, catalog: SI86-1) + 10mM NaI (Sigma Aldrich, catalog: 793558), used as electron mediator and 100 mM KCl as supporting electrolyte in the electrochemical cell. A Custom-built tunable wavelength light source setup consisting of 300 W

Xenon lamp (Newport, model: 6258), focusing lenses and monochromator (oriel cornerstone, 130 1/8m monochromator model: 74004) were used as the light source for measuring the photocurrent action spectrum. The power output from the tunable wavelength light source at each set wavelength was measured using Si photodiode power sensor (Thorlabs, part no. S120VC). This power output spectrum is utilized for normalizing the photocurrent action spectrum at corresponding wavelengths.

UV-Visible absorbance and fluorescence: All spectral absorbance and fluorescence data was obtained on BioTek Synergy H1 well plate reader at room temperature. The PSI solution was prepared by diluting the stock PSI solution with 20mM Phosphate buffer solution without adding detergent for PSI solubilization.

Circular Dichroism:

The UV-visible CD spectra was collected with Aviv Instruments Inc. Model 202, circual dichroism spectrometer at a scanning speed of 72 nm/min, with a bandwidth of 1nm at room temperature. The CD measurements were taken in a quartz cuvette with a path length of 1mm. The protein secondary structure was calculated using the Dichroweb online server (http://dichroweb.cryst.bbk.ac.uk) [160]. The fitting was performed with CDSSTR analysis program using the Sreerama et. al., reference data set [161].

4.3 Results & Discussion:

a. UV/Vis-absorption spectroscopy:

Proteoliposomes of PSIs reconstituted in DPhPG and DPhPC lipids are collected from the SEC step, as per the protocols described in the methods section and in our previous works[58, 59]. We present here the UV/Vis absorption spectra collected for the different PSI-proteoliposomes and compare them to the standard absorption spectrum of unbound PSI in solution. The absorbance values recorded for bare PSI and PSI-proteoliposomes were normalized by their respective absorbance values at ~680 nm for comparison. As shown in Figure 4.1 (a) dotted green and solid blue curves, the 439 nm absorption peak of PSI is blue shifted to 413 nm with large edge enhancements for the PSI-proteoliposomes, which indicate successful protein reconstitution into the DPhPG lipid membrane as also observed in our earlier work [59]. Also, the spectrum indicates that a slight shift (~ 1 nm) in the Qy band peak (~680 nm) for the PSI-proteoliposomes as compared

to the unconfined PSIs. Added to this, we also observe characteristic changes in the green region (500 - 580 nm) and around the Qy-bands (650-720 nm). Noting that the green region represents most of the carotenoid absorptions, the characteristic Car absorptions in the proteoliposomes get significantly increased in the green region, where the characteristic absorption for isolated PSI is normally expected to minimal (Figure 4.1 (a)). We observe a significant increase in the relative ratio of the absorbance in the 500-580 nm range to the absorbance at the ~680 peak for the reconstituted PSIs as compared to the control PSI solution. For clarity of understanding, the ratio of the normalized absorbance values for PSI-DPhPG proteoliposomes to corresponding value for the bare PSI are plotted in Figure 4.1 (a) dash dotted purple curve. A distinct ~ 3.5 times enhancement in the absorbance is observed at ~ 540 nm wavelength. This unique absorption in the green region for PSIs under membrane confinements clearly increases the overall extent of light absorption due to this additional absorption in the green region which is otherwise well-known to be the least absorbing region of the spectra - thereby giving the green tint for most photosynthetic organisms. This is one of the most crucial observations here since it implies that the carotenoids and blind chlorophylls get activated to start absorbing light in the ~520-570 nm range when PSI is under membrane confinements.

The other key observation here is the widening of the absorbance peak around the Qy band. As shown in Table 4.1, the Full-Width Half Maximum (FWHM) of the ~680 peak for the Qy band for the PSI-DPhPG proteoliposomes increases by ~64% as compared to the FWHM for the control PSI solution. This is more clearly observed from the enhancements recorded in Figure 4.1(a) (dash dotted purple curve) for the ratio of the relative changes in the normalized absorbance for PSI-DPhPG systems to the normalized absorbance for bare PSI indicating the two maxima at ~656 nm and ~698 nm around the 680 nm peak. The comparisons for the area under the curve (AUC) of the normalized absorbance spectra (Figure 4.1(a)) between 450 - 750 nm shows that there is a ~45% increase in the AUC for the PSI-DPhPG proteoliposome absorbance as compared to that for PSI absorbance. This indicates that the characteristic absorptions for PSIs under DPhPG confinements get significantly enhanced, especially due to the emergence of the unusual enhanced absorption in the green region.

The reconstitution of PSI into DPhPC lipid vesicles was performed by following the procedure identical to the PSI reconstitution into DPhPG vesicle. After the subsequent steps of

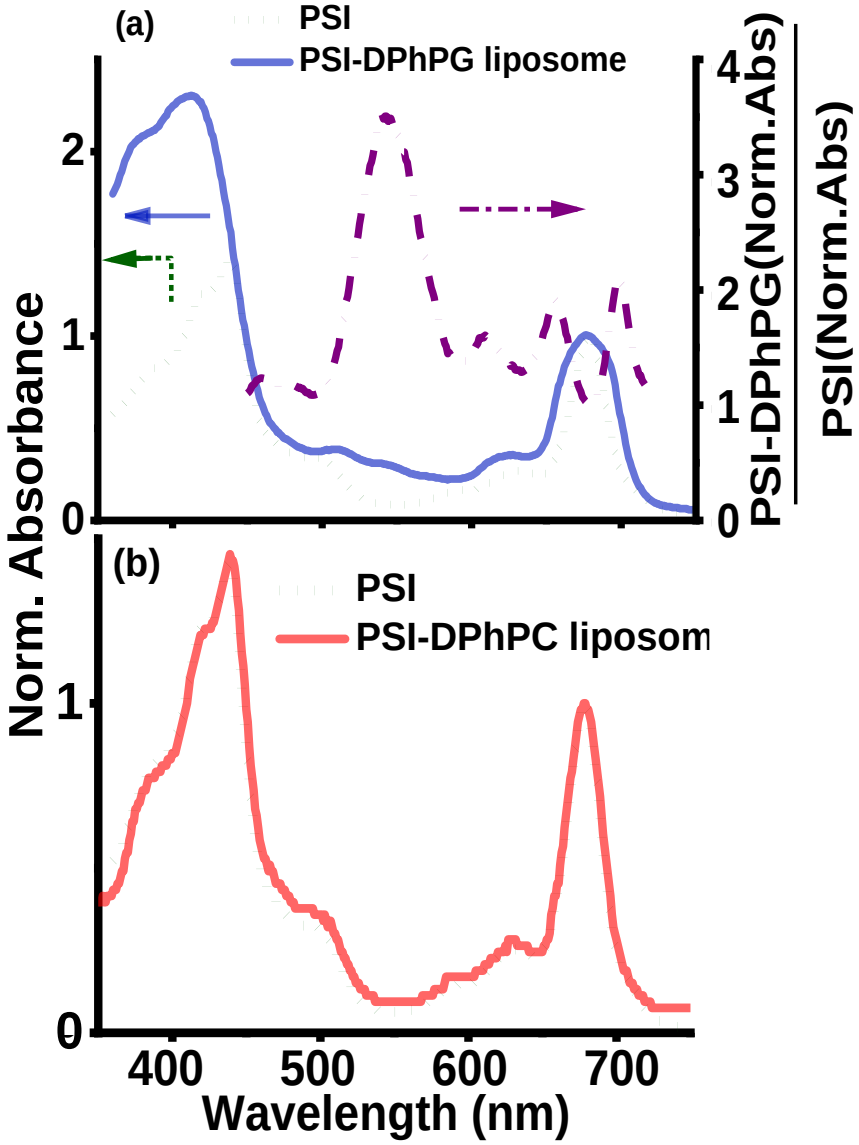

Figure 4.1 (a) Room temperature normalized absorption spectra of PSI (dotted green) and PSI-DPhPG proteoliposome (solid blue) indicating characteristic changes in the spectra of PSI before and after reconstitution into DPhPG lipid membrane. The absorption data was normalized with its own Qy band peak absorbance for both PSI and PSI-proteoliposome. The ratio of normalized absorbances of PSI-DPhPG liposome to PSI (dash dotted purple) indicating the characteristic enhancement in the absorbance spectra of PSI after reconstitution compared to isolated PSI. (b) Room temperature normalized absorbance spectra of PSI-DPhPC (solid red) liposome and PSI (dotted green).

Table 4.1 The FWHM of Qy band and AUC of normalized absorbance for PSI and PSI-DPhPG liposome in Figure 4.1(a).

	PSI solution	**PSI-proteoliposome (DPhPG)**	**Increment**
FWHM at Qy-band (650-720 nm)	29.3 nm	48.1 nm	64.16%
AUC (450 nm – 750 nm)	75.76	109.93	45.10%

slow detergent removal and the SEC steps, the final isolated PSI-DPhPC liposome solution is tested here for their absorbance properties. In comparison to the PSI-DPhPG case, the UV/Vis absorption spectra in Figure 4.1 (b) for the PSI-DPhPC proteoliposomes show no characteristic peak shifts or alterations when compared to the control bare PSI case. In fact, here the absorption spectrum follow the expected spectral profile similar to the PSI in all the regions including the 500 - 580 nm range, thereby indicating that the light absorption characteristics for the PSI-DPhPC proteoliposomes do not deviate much from that observed for bare PSI case. In sum, in this section we report unique alterations in the absorption characteristics of PSI-DPhPG proteoliposomes that reflect blue shifts in the Soret region (~443- 503 nm), distinct broadening of the Qy bands (~ 675 - 685 nm) and more importantly, unusual absorption by the Cars and blind chlorophylls in the green region (~500 -580 nm).

b. Fluorescence spectroscopy:

The respective fluorescence spectra collected with 440 and 550 nm excitation wavelengths for bare PSI (control), PSI-DPhPG proteoliposomes (specific) and PSI-DPhPC (specific) are reported here in Figure 4.2 (a), (b) and (c) respectively. The solid and dotted green curves of Figure 4.2 (a) shows the fluorescence emission spectra recorded for bare PSI at the excitation wavelengths of 440 nm and 550 nm, respectively. Specifically, for the 550 nm excitation, we observe a new dominant emission peak at ~660 nm along with the characteristic ~722 nm emission band for PSI.

This indicates that with the 550 nm excitation, two different radiative energy dissipative pathways are activated via strong fluorescence at ~660 nm (possibly from the Cars absorption at 450-550 nm) and a relatively weak fluorescence at ~722 nm (possibly from the weaker Chla absorptions). But, bearing in mind the unrestricted non-radiative dissipation pathways (heat) already available for the unconfined PSI, the interesting observation here is that the additional large radiative energy dissipation mediated via the strong ~660 nm fluorescence emissions would suggest an inefficient energy transfer to the P700 before the excitation energy can be funneled to the P700 for effective charge separation it is being emitted at ~660 nm. Hence, while both 440 and 550 nm excitations provide ample energy dissipation routes (both radiative and non-radiative) in the unconfined PSI, the energy loss is enhanced via the additional emissions at ~660 nm for the 550 nm excitation case. We have also investigated this excitation wavelength dependent fluorescence via gradual increments in the excitation wavelengths from 440 nm to 550 nm in steps of ~10 nm. As the excitation wavelength increased from 440 nm to 550 nm, the fluorescence band at ~660 was observed to gradually increase as compared to the emission band at ~722 nm. It should be noted here that the 440 nm excitation activates the Chla soret band, whereas the 450-550 nm excitation mostly activates the Cars.

For direct comparisons, similar excitation wavelength-dependent fluorescence emission is also measured for the PSI-DPhPG proteoliposomes. The fluorescence emission from PSI-DPhPG samples at 440 nm excitation (solid blue line in Figure 4.2 (b)) indicate that under lipid membrane confinements, the fluorescence peak shifts to ~680 nm from the well-known peak typically recorded around ~722 nm for bare PSI at room temperature conditions[162, 163]. Such blue shifts in fluorescence were also reported for PSI under organic and inorganic confinements previously [57, 59]. This large ~42 nm blue shift in the fluorescence peak has been previously reported as the characteristic indication of microenvironment alterations around PSI and/or conformational changes in the protein structures [151, 164]. Interestingly, as seen from blue curves of Figure 4.2 (b), minimal differences are observed in the characteristic emission spectra when the excitation wavelength is increased from 440 nm to 550 nm. The slight broadening toward the trailing blue edge of the ~680 nm peak (dotted blue line in Figure 4.2 (b)) can be plausibly explained by the excess absorption in the green region for the PSI-DPhPG samples (see Figure 4.1 (a)). Unlike the appearance of the large blue shifted peak maxima at ~660 nm for bare PSI when the excitation wavelength is changed from 440 to 550 nm, the fluorescence spectra for the PSI-DPhPG samples

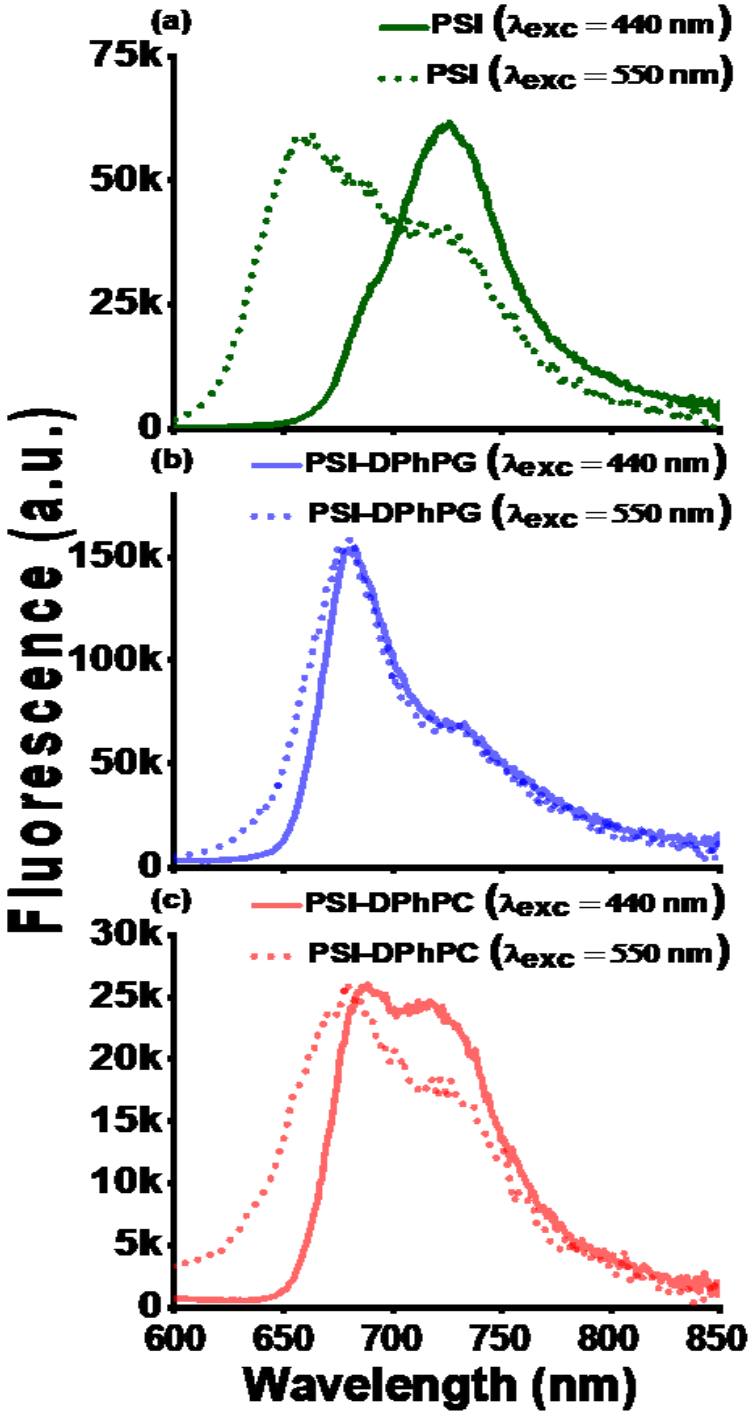

Figure 4.2 Room temperature fluorescence spectra of (a) PSI (green), (b) PSI-DPhPG proteoliposome (blue) and (c) PSI-DPhPC proteoliposome (red) with 440nm (solid) and 550 nm (dotted) excitation wavelength.

remain relatively invariant for both 440 and 550 nm excitations. This provides the first qualitative indication of of new and altered photoexcitation and energy dissipation pathways being mapped

out possibly by the unique activation of the Car networks in PSI under membrane confinements. Upon careful observation of Figure 4.2 (a) & (b), it can be seen that the relative ratios of the peak intensities at ~680 nm to the characteristic ~720 nm peak in the PSI-DPhPG cases are significantly enhanced as compared to the respective peak intensity ratios between ~660 nm and ~720 nm for the bare PSI case (specifically, for the 550 nm excitation case for bare PSI). If we account for the two different energy dissipation modes, namely radiative (light) and non-radiative (heat), then we can indirectly infer from these observations that the highly enhanced and blue-shifted radiative fluorescence from the PSI-DPhPG samples (blue lines in Figure 4.2 (b)) imply weaker non-radiative dissipation pathways in the PSI-DPhPG proteoliposomes as compared to the bare PSI. This would also make sense considering the absence of any lipid barriers around the bare PSI to tailor its non-radiative energy dissipation routes. Such tailoring of the radiative and non-radiative dissipation pathways to alter the effective photoexcitation energy transfer process in PSI could be hypothetically attributed to the unique photoactivation of the Car networks and alterations in the Car-Chla interactions due to the membrane confinements of the PSI (as also corroborated by the unusual absorption in the green region in Figure 4.1 (a)). But a more definite validation of such a hypothesis would require the analyses of the CD spectral data that will be presented in our following section.

The fluorescence emission spectra for the PSI-DPhPC liposomes and bare PSI at the excitation wavelengths of 440 and 550 nm are shown in Figure 4.2 (c) as solid and dotted red curves, respectively. For the 440 nm excitation, the typical PSI fluorescence emission peak at ~722 nm also exists in the PSI-DPhPC emission spectrum. The characteristic blue-shifted fluorescence peak at ~690 nm is observed as before indicating the PSI reconstitution into the DPhPC lipid membranes[57, 59]. But, unlike the PSI-DPhPG case, the 550 nm excitation induces a further blue shift of the 690 nm fluorescence peak in the PSI-DPhPC sample (see dotted red curve in Figure 4.2 (c)), with the 690 nm peak becoming dominant over the 722 nm peak when compared to its corresponding emission profile for the 440 nm excitation. Here, it should be noted that the fluorescence spectra for unconfined PSIs (see green curves of Figure 4.2 (a)) typically divulge two characteristic features when the excitation wavelength is changed from 440 nm to 550 nm: i)

emergence of a blue shifted dominant peak at ~660 nm and ii) relative decrease in the ~722 nm emission peak intensity. Thus, unlike the PSI-DPhPG case study, the fluorescence spectra for the PSI-DPhPC proteoliposomes follow both the aforementioned features of the bare PSI case as the excitation wavelength is increased from 440 nm to 550 nm. However, the first attribute of the blue shift of ~10 nm in the fluorescence maxima is not as significant for the PSI- DPhPC case as the ~62 nm blue shift for the bare PSI case. However, a careful observation also reveals that the ratio of the relative fluorescence peak intensity at ~690 nm to the one at ~722 nm is much subdued for the PSI-DPhPC case as compared to the corresponding ratio noted for the PSI-DPhPG case in Figure 4.2 (b). On the basis of our earlier analyses, one can indirectly infer here that under DPhPC confinements, the relatively subdued radiative dissipation pathways (fluorescence) imply the possible opening up of energy losses from the non-radiative dissipation channels (heat) that, in turn, can disrupt the amount of excitation energy effectively funneled to the P700 in PSI. In fact, the relative intensities and blue-shifts of the fluorescence peak at ~690 nm for the PSI-DPhPC proteoliposomes as seen from Figure 4.2 (c), and when compared to the respective values for the PSI-DPhPG case in Figure 4.2 (b), can provide us an indirect and qualitative estimation that the non-radiative dissipation losses for PSI-DPhPC are less than those for bare PSI but more than what is observed for PSI-DPhPG.

Overall, the fluorescence spectral data in this section provides a qualitative analysis suggesting that an enhanced and blue-shifted fluorescence peak profiles for the PSI confinements in biomimetic DPhPG lipid membranes imply distinct suppression of the non-radiative dissipation pathways that can, in turn, also make more excitation energy directed toward the P700. This enhancement of the photoexcitation pathways in PSI-DPhPG samples is also facilitated by the increased characteristic absorption in the green region (Figure 4.1 (a)). Unlike the PSI-DPhPG case, the relatively weaker fluorescence emissions peak profile for the PSI-DPhPC, along with its similar behavior as the emission profiles from bare PSI cases, indicate relatively enhanced non-radiative dissipation pathways in both the cases with the bare PSI obviously exhibiting the most unrestrained dissipation losses. It is worth mentioning that the DPhPC lipid breakthrough force observed to be greater than 10 nN which is significantly higher than 1.95 nN observed for DPhPG lipids [60, 165, 166]. The relative rigidness of the DPhPC lipids could have facilitated in enhancing the non-radiative dissipation (heat) compared to softer DPhPG due to the altered heat transfer rates.

Circular Dichroism Spectroscopy:

Previous studies have well documented the use of UV and visible circular dichroism spectroscopic techniques to infer changes in structural, conformational and Chla-Chla/Car-Chla interactions in photosynthetic proteins [167-169]. Hence, in this section we resort to CD spectral analyses in our effort to explain the aforementioned intriguing and unique observations from the absorption and fluorescence spectra for the PSI under DPhPG and DPhPC confinements. It needs to be pointed out here that for effective comparisons, the CD spectra for the PSI-proteoliposomes and bare PSIs were taken while keeping the PSI concentration constant. Firstly, the visible CD spectra for the PSI and PSI-DPhPG liposome in Figure 4.3 (a) top is devoid of any bands in the 540 - 640 nm region. Hence, the overlapping CD signal for both the PSI and PSI-proteoliposome in the 540 - 640 nm region reflects the identical concentration of chlorophylls/PSI units. Furthermore, the spectra for the bare PSI controls show two bands at around (+) 671 nm and (-) 685 nm in the Qy region. These bands represent the excitonic interactions between the Chla dimers (P700) of PSI [151, 168]. The absence of (-) 650 nm band related to Chlorophyll b is evident since the extracted PSI does not contain any Chlb. Also, the (+) 442 nm and (+) 503 nm bands in the Soret regions originate from the Chla and Cars respectively [151].

As shown in Figure 4.3 (a) top and Table 4.2, the CD signals for the Chla bands in the Qy region (671 nm, 685 nm) and Soret region (442 nm) indicate significantly increases for the PSI-DPhPG samples compared to the bare PSI. This is indicative of enhanced chromophore-chromophore interactions for the reconstituted PSI. In addition, the enhanced CD signals for the Qy region bands also indicate the improved excitonic interactions of the Chla dimer. It should also be noted that the 671 nm band is slightly blue-shifted to 669 nm in the PSI-DPhPG proteoliposomes. This enhanced CD signal in Qy region and the blue shift incidentally coincide with the improved FWHM of the Qy band at ~680 nm in the absorption spectrum. One can infer from this that these exists a direct correlation between enhanced light-harvesting and enhanced excitonic interactions. Interestingly, the Car band at 503 nm of the CD signal is also enhanced and blue-shifted to 501 nm for PSI-DPhPG. This, on the other hand, is a clear indication of the increased Car-Chla interactions and Car-protein interactions. The improved Car-Chla interactions suggest that the excitation energy exchanges between Cars and Chla are improved which can be critical in the case of Cars acting as accessory light harvesting units. Finally, the augmented Car-

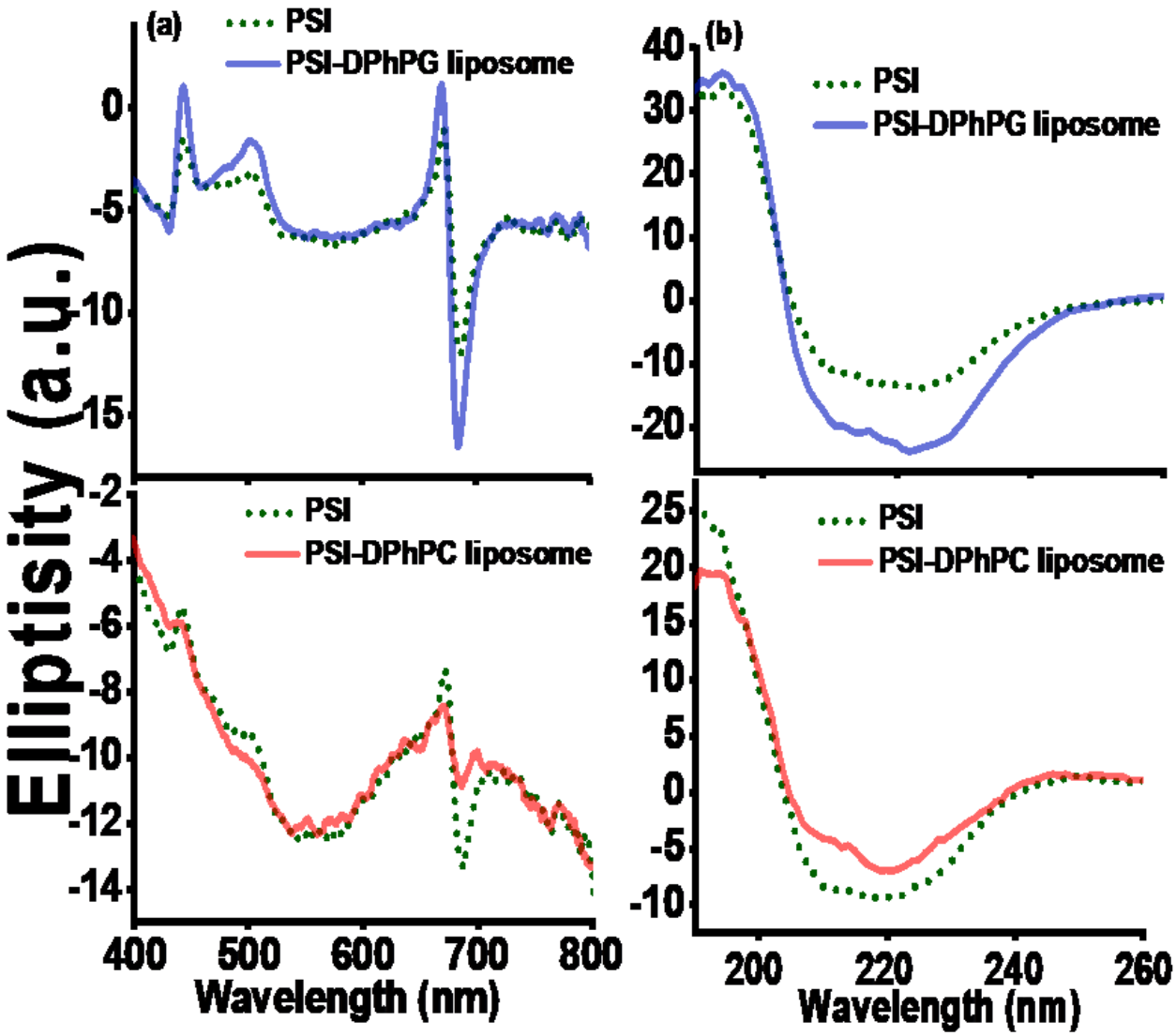

Figure 4.3 (a) Visible CD spectra of PSI (dotted green), PSI-DPhPG liposome (solid blue) and PSI-DPhPC (solid red). (b) UV CD spectra of PSI (dotted green), PSI-DPhPG liposome (solid blue) and PSI-DPhPC liposome (solid red). The Chla concentration kept constant for both PSI and PSI-DPhPG liposome (top) or PSI-DPhPC liposome (bottom) for CD measurements

Table 4.2 The location of CD peaks for Chla and carotenoids in PSI, PSI-DPhPG and PSI-DPhPC liposomes. The Δ is the difference of CD signal of PSI-DPhPG or PSI-DPhPC and PSI at the respective band peaks.

	PSI	**PSI-DPhPG**	**PSI-DPhPC**
Chla peak position (nm)	671	669 (Δ = 2.097)	670 (Δ = -0.685)
	685	685 (Δ = 4.665)	685 (Δ = -1.113)
	442	442 (Δ = 2.682)	441 (Δ = 0.267)
Cars peak position (nm)	503	501 (Δ = 1.527)	501 (Δ = -0.703)

protein subunits interactions possibly suggest the increased role of Carotenoids in the protein structural stabilization.

In case of PSI-DPhPC liposomes, the visible CD spectra in Figure 4.3 (a) bottom also indicate the close overlap in the 540 nm – 640 nm region, thereby confirming the similar Chla concentrations in controls and specific samples. In contrast to the observations from the PSI-DPhPG case, the CD signal intensities for the Chla bands at the Qy region and the soret region decrease for the PSI-DPhPC liposomes as compared to PSI. Moreover, the Car bands at ~503 nm also decreases for the PSI-DPhPC liposomes. The differences in the signal values (Δ in Tables 4.2) between PSI-liposomes and bare PSIs at the respective peaks are much smaller for the PSI-DPhPC case as compared to the observed Δ in the case of PSI-DPhPG liposomes, indicating lesser variations in the Chla-Chla and Chla-Car interactions in PSI-DPhPC from that observed in PSI.

The UV-CD data in Figure 4.3 (b) top is collected for PSI and PSI-DPhPG for observing the protein secondary structure alterations. As shown in Table 4.3, the UV-CD spectral analysis indicates that the PSIs contains 55% α-helix, 21.5% β-sheet, 6.5% turn, 16.5% disordered structure whereas the reconstituted PSI-DPhPG samples contains 65% α-helix, 16% β-sheet, 2% turn, and 16% disordered structure. The increased α-helix contents and decreased β-sheets, turns and

Table 4.3 The contents of protein secondary structure in PSI, PSI-DPhPG and PSI-DPhPC liposomes.

	PSI	PSI-DPhPG	PSI-DPhPC
α-helix (%)	55	65	43
β-sheet (%)	21.5	16	26
Turn (%)	6.5	2	11
Disorder (%)	16.5	16	20

disorders provide a clear picture of the secondary protein structures in PSI being altered when PSI is encapsulated in the DPhPG lipid membrane. Here it needs to mention that altering the protein secondary structures affects the structural stability and functionality of the protein. As the protein secondary structures are correctly packed into its native conformations, it lowers their free energies thereby allowing it to approach the native functionality and efficiency[170]. Due to the presence of the more PG lipids in the native state, the aforementioned changes in the secondary structures might resemble the native conformation of the protein approaching its native functionality and stability. As shown in Figure 4.3 (b) bottom and Table 4.3, the UV-CD spectrum analyses of the PSI-DPhPC liposome indicate that the protein secondary structures have also slightly changed in the confined PSI. The percentage of β-sheets, turns and disorders is increased while the percentage of α-helices is decreased when PSI was reconstituted into the DPhPC liposome compared to the bare PSI. Interestingly, this is quite opposite to the secondary structure changes observed in the case of PSI-DPhPG proteoliposomes.

4.4 Discussion:

The characteristic changes in the absorption, fluorescence, and CD spectral properties for PSIs reconstituted in DPhPG and DPhPC liposomes both reveal interesting, unique and in some cases, intriguing effects. The results from these spectral analyses shed light on the structure-function variations in PSIs arising from the uniquely architected photoexcitation energy transfer and dissipation pathways under membrane confinements. Especially the PSI confinements in the DPhPG liposomes specifically reveal altered Cars-related attributes that include: 1) characteristic absorbance for the Cars and blind Chls in the 500nm - 580nm range; 2) the invariance in the fluorescence emission bands or the blue-shift of the fluorescence peak at ~660 nm when the

excitation wavelength is varied from 440 nm to 550 nm, unlike the fluorescence emissions from the bare PSI case; And, 3) characteristic blue shift for the Car bands at ~501 nm observed from the CD spectra .

Moreover, in case of PSI-DPhPG liposome, the enhanced FWHM around 680 nm band and enhanced CD signal around ~670 and ~685 nm peaks indicate improved light harvesting, excitonic interactions and efficient energy transfer to the chlorophyll dimer (P700). Furthermore, the increased CD signal at ~442 nm also indicates increased Chla-Chla interactions. Additionally, conformational changes in protein secondary structures are revealed through improved α-helix contents and reduced β-sheets, turns and disorders. In the case of PSI-DPhPC, CD signal enhancements are only observed at the Soret band of the Chl. Contrary to the PSI-DPhPG liposome, the protein secondary structures in this case are altered through decrease in α-helix contents and increase in β-sheets, turns and disorders.

The CD spectral data also reveal conformational changes in the protein secondary structures in PSI that could have also affected the Car-Chla interactions and/or the unique spectroscopic changes related to the Cars. All the observations from the current study point toward unique alterations in the Car activities leading to enhanced Car-Chla, Car-protein interactions that can significantly tailor the light harvesting properties by tuning the excitation energy transfer and dissipation pathways. Unlike the PSI-DPhPG liposomes, the Car attributes are much weaker in the PSI-DPhPC liposomes. Thus, increased light harvesting in the green region coupled with the unique Car activations and improved Car-Chla interactions in the PSI-DPhPG proteoliposomes could be responsible for tuning the dissipative pathways to effectively enhance the EET pathways within PSI that culminates in the charge separation at the P700 and promotes enhanced photon-to-electrochemical conversions.

Thus, in our effort to verify the implications of the aforementioned characteristic changes in regard to the EET and the charge transport properties in PSI under membrane confinements, the corresponding photocurrent action spectra for the PSI-DPhPG (specific) and the bare PSI (control) samples are recorded in Figure 4.4. One can immediately notice the corresponding characteristic enhancements in the photocurrent at the 500-580 nm range as well as the broadened FWHM for the photocurrents recorded around ~680nm peak. This is indicative of the enhanced excitation dynamics as a result of the improved light harvesting by Cars, particularly in the green region

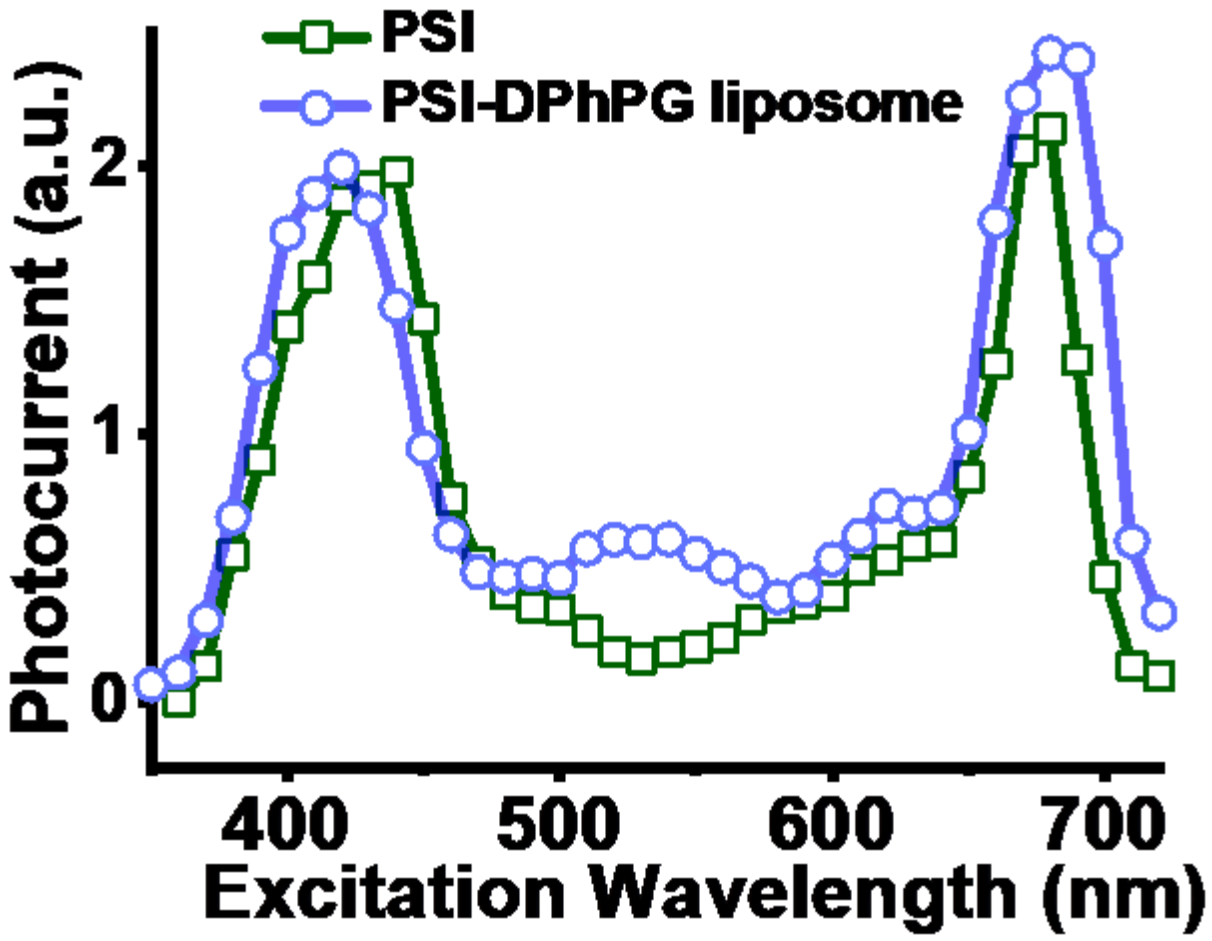

Figure 4.4 Photocurrent action spectra of PSI on ITO substrate (green squares) and PSI-DPhPG liposome coated on ITO (blue circles) after subtracting the background blank ITO photocurrent. The photocurrent was measured at open-circuit potential in aqueous solution carrying 50 μM of I_2 + 10mM NaI + 100mM KCl. Ag/AgCl and Pt wire used as reference electrode and counter electrode, respectively. Photocurrent data was normalized with power of excitation wavelength and adjusted vertically for comparing the characteristic behavior of the photocurrent action spectra

(500-580 nm), that are favorably funneling the excess energy to reaction center P700, thereby augmenting the EET process. In fact, our previous studies have reported ~4-5-fold photocurrent enhancements from PSIs confined in supported DPhPG lipid bilayers as compared to unconfined PSI monolayer that also corroborates the efficient EET process in the membrane bound PSIs.

Overall, the observations made from this study clearly indicate that Cars activity and Chla-Car interactions are enhanced that can significantly alter the relative efficiencies of the light harvesting and energy dissipation pathways in PSI confined in DPhPG lipid membranes. In fact, if we attribute the emergence of the ~660 nm blue shifted peak in the bare PSI case under 450-550 nm excitation to the ineffective photo-activation of the Car networks then, based on the non-emergence of any blue shifted peak under 450-550 nm excitation for the PSI-DPhPG cases in Figure 4.2 (b), we could hypothesize that lipid confinements uniquely activate the Car networks and alter the Car-Chla interactions to enhance both the radiative energy dissipation (via fluorescence) and photoexcitation energy transfer (via exciton transfer) pathways through the Chla networks, while subduing the non-radiative dissipation modes. This, in turn, will inadvertently imply the improved efficacy of the Car networks in transferring the excitation energy to the reaction center P700 in PSI under DPhPG membrane confinements as compared to unconfined PSIs. These preliminary hypotheses also corroborate our earlier observations from the absorption spectra for PSI-DPhPG case (Figure 4.1 (a)) indicating excess light harvesting in the green region due to Car activations.

Interestingly, a recent study by Minjung Son et. al. [156] on light harvesting complex II (LHCII) under near-native discoidal membrane confinements had also suggested effective enhancements in the dissipating pathways while suppressing the EET pathways in their LHCII-membrane systems. To this end, it should be highlighted here that by no means we can claim from our work here that the PSI-DPhPG proteoliposomes with the dampened non-radiative dissipation pathways would architect the best or the optimal EET process. In fact, one can easily surmise that excessive dampening of the dissipation pathways might also lead to localized energy traps in the chromophore networks that can result in excessive electron-hole recombination losses and/or photobleaching over long periods of time. All that the current study claim is that the suitable choice and design of biomimetic lipid membranes could potentially facilitate the effective tuning of the relative pathways for the excitation energy transfer and dissipation in PSI. As a closing statement,

we would like to highlight that a direct proof for the alterations in the EET and radiative/nonradiative dissipation pathways in PSIs under confinements, as posited in the present study, would require systematic ultra-fast electronic/vibrational spectroscopic measurements with unprecedented spatiotemporal resolutions in future that is beyond the scope of the current work.

4.5 Conclusion:

Alterations in the photoexcitation and dissipation pathways for PSI confined in DPhPG and DPhPC lipid membranes are investigated here by using absorbance, fluorescence, and circular dichroism spectroscopies. The carotenoid networks in PSI underwent unique changes in their characteristic spectral attributes only when PSI was confined in DPhPG lipid membranes. These attributes include enhanced characteristic absorption and EET in the green region (500 nm -580 nm) as indicated from absorbance and photocurrent measurements, and enhanced carotenoid-Chla excitonic interactions, as indicated from enhanced CD signals. Moreover, a ~64% increment in the FWHM around the Qy region of the absorbance band (~680 nm) and the enhanced CD signals from the Chla bands indicate improved Chla-Chla excitonic interactions that promotes broad-band light harvesting in PSI. Unlike the bare PSI fluorescence emission, the fluorescence spectrum from PSI-DPhPG proteoliposomes indicate the absence of the characteristic blue shift in the peak maxima or appearance of the new emission band at ~660 nm when the excitation wavelength is changed from 440 nm to 550 nm. These specific changes in the PSI spectral properties indicate uniquely altered pathways for excitation transfer and dissipation in PSI under DPhPG membrane confinements. Such distinct alterations in the Car and Chla spectral bands are not observed for the PSI-DPhPC confinements, where the EET pathways are hindered by enhanced dissipation modes. The ratios of the two fluorescence emission band values for the respective samples are in the ascending order of PSI, PSI-DPhPC and PSI-DPhPG indicating the respective weakening of the effective non-radiative energy dissipation pathways. The protein secondary structures for PSI-DPhPG are altered significantly to indicate an increase in α-helices and decrease in β-sheets. In case of the PSI-DPhPC the α and β structures in the protein secondary structure are altered conversely when compared to the PSI-DPhPG case. The current study is useful for the fundamental understanding of optoelectronic properties of PSI under biomimetic confinement and useful for designing efficient bio-hybrid photovoltaic devices, biosensors, and artificial photosynthesis systems.

Chapter 5

Conclusions

The current dissertation presents a detailed and systematic investigations into the effects of microenvironment alterations on the PSI photo response behaviors, induced by electromagnetic and lipid confinements architected by tailored plasmonic nanostructures and synthetic phospholipids. The studies pave the path for future integration and assembly of cyanobacterial PSI into functional bio-hybrid photovoltaic/photo-electrochemical devices for efficient solar energy harvesting.

Chapter 1 makes the imperative case for the global shift from fossil fuels energy consumption to renewable energy resources and the great potential of abundant solar energy in this effort. The primary solar harvesting biological engines PSII and PSI, and their roles in the initial light dependent reactions during oxygenic photosynthesis process are discussed. A detailed description of PSI and its cofactors are presented with respect to its structural, electrochemical, functional properties. A brief history of research works towards PSI based bio-hybrid photovoltaic devises, photocatalysis and photo biosensors are mentioned while the strategies to improve the performance of the PSI are emphasized. At the end the LSPR effect of plasmonic nanostructures is introduced with a brief history PSI integrating with LSPR of metal nanostructures In addition, the investigation towards role of biomimetic lipid membrane confinement in altering the PSI functionality was introduced with our group's previous accomplishments.

In **Chapter 2**, the plasmon enhanced photocurrent of PSI was experimentally investigated to demonstrate an effective strategy to improve light harvesting of PSI, in biohybrid optoelectronic devices by coupling with LSPR electric field of plasmonic nanostructures. To this end, the enhanced performance of PSI was examined when integrated with Fischer patterns of plasmonic silver nanopyramid (Ag-NP) structures that are fabricated using Nano-Sphere Lithography (NSL). Specifically, the photocurrent measurements of PSI coated Ag-NP substrate in comparison to PSI coated non-plasmonic planar silver substrate as well as control background uncoated substrates was analyzed. In conclusion, our work presents the first-ever experimental observation of plasmon-induced photocurrent enhancements in cyanobacterial PSI coupled to Fischer patterns of

Ag-NP structures as a result of plasmon-induced localized electric field. This was achieved by tuning the plasmonic absorption peak of Ag-NPs to the absorption peak of PSI at ~675 - 680 nm wavelengths. A large PSI photocurrent enhancement factor of ~6.5 was noted for 660 nm excitation of PSI assembled on Ag-NP/ITO surfaces as compared to PSI on non-plasmonic planar Ag electrodes under similar conditions. The photocurrent enhancement factors increased only slightly from the excitations at 470 nm to the excitation at 660 nm owing to the enhanced plasmon-induced fluorescence emission losses for red light excitations as compared to blue light excitations. The fundamental findings of the current work are crucial in designing rational biotic-abiotic interfaces for future bio-hybrid solar energy harvesting technologies.

However, due to the intrinsic defects in the nanostructure's fabrication process of NSL and less control over specific plasmon modes interacting with PSI. Therefore, the **Chapter 3** is dedicated to address the challenges of finding the more accurate plasmon enhancement factors and track the effect of specific plasmonic resonance modes. To this end, plasmonic Au and Ag nano disc (AuND and AgND) are fabricated with high resolution Electron Beam Lithography (EBL) method, whose geometric properties are tailored to tune their absorption peaks to ~680 nm and 565 nm respectively. Our experimental results indicate substantial photocurrent enhancement for PSI spatially assembled in the LSPR mode volume around AuNDs and AgNDs. Action spectra for the plasmon-induced photocurrent enhancement factors measured by using 9 LED light sources over a wavelength range of 395 nm – 810 nm clearly reveals that the characteristic trend of the spectra strongly follows the absorption spectra for the plasmonic AuND and AgND substrates. We report strong enhancement factors of ~17.5 and ~5.5 at the green light excitation of 565 nm for the AgNDs and AuNDs respectively, thereby indicating the unique activation of the blind chlorophylls under the influence of LSPR electric fields. Specifically, an intriguing observation is that the excitation wavelengths of 470 nm and ~565 nm both generated equal enhancement factor of ~17.5 for the PSI/AgND/ITO$_{SAM}$ samples, even though the AgND resonance intensity at 470 nm is lower than that at 565 nm. This observation paves the path for tuning the carotenoid excitation at ~470 nm to promote more efficient LSPR induced photocurrent enhancements. To the best of our knowledge, such detailed and systematic studies have heretofore not been carried out to investigate the direct interactions of spatially resolved and spectrally tuned LSPR modes with PSIs to modify their photoexcitation pathways and, enhance the ensuing photocurrent generations. The

fundamental findings of the current work are crucial in designing rational biotic-abiotic interfaces for future bio-hybrid solar energy harvesting technologies.

Inspired by previous work of our group, **Chapter 4** dives into the fundamental understanding of conformational, structural and excitation pathway changes in biomimetic synthetic lipid membrane reconstituted PSI through the detergent mediated solubilization method. Alterations in the photoexcitation and dissipation pathways for PSI confined in DPhPG and DPhPC lipid membranes are investigated here by using absorbance, fluorescence, and circular dichroism spectroscopies. The carotenoid networks in PSI underwent unique changes in their characteristic spectral attributes only when PSI was confined in DPhPG lipid membranes. These attributes include enhanced characteristic absorption and EET in the green region (500 nm -580 nm) as indicated from absorbance and photocurrent measurements, and enhanced carotenoid-Chla excitonic interactions, as indicated from enhanced CD signals. Moreover, a ~64% increment in the FWHM around the Qy region of the absorbance band (~680 nm) and the enhanced CD signals from the Chla bands indicate improved Chla-Chla excitonic interactions that promotes broad-band light harvesting in PSI. Unlike the bare PSI fluorescence emission, the fluorescence spectrum from PSI-DPhPG proteoliposomes indicate the absence of the characteristic blue shift in the peak maxima or appearance of the new emission band at ~660 nm when the excitation wavelength is changed from 440 nm to 550 nm. These specific changes in the PSI spectral properties indicate uniquely altered pathways for excitation transfer and dissipation in PSI under DPhPG membrane confinements. Such distinct alterations in the Car and Chla spectral bands are not observed for the PSI-DPhPC confinements, where the EET pathways are hindered by enhanced dissipation modes. The ratios of the two fluorescence emission band values for the respective samples are in the ascending order of PSI, PSI-DPhPC and PSI-DPhPG indicating the respective weakening of the effective non-radiative energy dissipation pathways. The protein secondary structures for PSI-DPhPG are altered significantly to indicate an increase in α-helices and decrease in β-sheets. In case of the PSI-DPhPC the α and β structures in the protein secondary structure are altered conversely when compared to the PSI-DPhPG case. The current study is useful for the fundamental understanding of optoelectronic properties of PSI under biomimetic confinement and useful for designing efficient bio-hybrid photovoltaic devices, biosensors, and artificial photosynthesis systems.

Future direction:

1) Inspired by the current research findings related to PSI coupling with LSPR field of plasmonic nanostructures, future tailored designs of nanopatterned structures can be conceived that will allow the systematic immobilization of every PSI trimeric complex under the direct influence of LSPR electric fields for maximizing the plasmon-enhanced photocurrents from these systems. One simple way of doing this is to arrange the AuND or AgND in hexagonal packing with decreased distance of separation between the discs. While doing this, the plasmon resonance peaks should be tracked simultaneously.

2) Two closely spaced plasmonic nanostructures or dimers have hot spot in between them where the localized electric field is very strong. The field enhancement grows as the distance between them reduces. The impact of such plasmonic hot spots on photocurrent enhancements can be characterized with a localized conductive AFM set up. The immobilized PSI in the hot spot can be genetically modified to have site specific tagging such that the functionalized bio-conjugate AFM tips can make covalent bonds with the site-specific tags on PSI. This arrangement will be of great help in characterizing the distance of separation, various geometries, and nanomaterials for the plasmon enhanced photocurrent effect in single PSI unit.

3) Inspired by the research work reported in Chapter 4, different bio-mimetic and synthetic lipid membranes with other functional head groups and charges can be explored in future to get a mechanistic insight into the tenability of membrane-induced optoelectronic properties in reconstituted PSIs. Furthermore, the membrane stiffness factors can also be altered in future by designing lipid vesicles with mixed lipid components and cholesterol with varying ratios. Such investigations can open up the tremendous possibilities of tailoring the competing photoexcitation and energy dissipation pathways in bio-inspired quantum systems.

References

1. Govindjee, R. *The Z-scheme diagram of photosysnthesis*. 2000; Available from: http://www.life.illinois.edu/govindjee/ZSchemeG.html.
2. Perez, R., *Making the Case for Solar Energy*, in *Day light & Architecture*. 2008.
3. Green, M.A., *Photovoltaics: technology overview*. Energy policy, 2000. **28**(14): p. 989-998.
4. Björn, L.O., *The evolution of photosynthesis and chloroplasts.* Current Science, 2009: p. 1466-1474.
5. Blankenship, R.E., M.T. Madigan, and C.E. Bauer, *Anoxygenic photosynthetic bacteria*. Vol. 2. 2006: Springer Science & Business Media.
6. Montero, F., *Photosynthesis*, in *Encyclopedia of Astrobiology*, M. Gargaud, et al., Editors. 2011, Springer Berlin Heidelberg: Berlin, Heidelberg. p. 1245-1249.
7. Utschig, L.M., et al., *Z-scheme solar water splitting via self-assembly of photosystem I-catalyst hybrids in thylakoid membranes.* Chemical science, 2018. **9**(45): p. 8504-8512.
8. 2015; Available from: https://en.wikipedia.org/wiki/Photosynthesis#/media/File:Thylakoid_membrane_3.svg.
9. Govindjee, G.a.R. *Photosynthesis and the "Z"-scheme*. 2000; Available from: http://www.life.illinois.edu/govindjee/textzsch.htm.
10. Grotjohann, I. and P.J.P.r. Fromme, *Structure of cyanobacterial photosystem I.* 2005. **85**(1): p. 51-72.
11. Jordan, P., et al., *Three-dimensional structure of cyanobacterial photosystem I at 2.5 Å resolution.* 2001. **411**(6840): p. 909.
12. Melkozernov, A.N., *Excitation energy transfer in Photosystem I from oxygenic organisms.* Photosynthesis research, 2001. **70**(2): p. 129-153.
13. Laible, P.D., R.S. Knox, and T.G. Owens, *Detailed Balance in Förster− Dexter Excitation Transfer and Its Application to Photosynthesis.* The Journal of Physical Chemistry B, 1998. **102**(9): p. 1641-1648.
14. Sundström, V., T. Pullerits, and R. van Grondelle, *Photosynthetic light-harvesting: reconciling dynamics and structure of purple bacterial LH2 reveals function of photosynthetic unit*. 1999, ACS Publications.
15. Brettel, K. and W. Leibl, *Electron transfer in photosystem I.* Biochimica et Biophysica Acta (BBA)-Bioenergetics, 2001. **1507**(1-3): p. 100-114.
16. Bruce, B.D. and R.J.J.o.B.C. Malkin, *Subunit stoichiometry of the chloroplast photosystem I complex.* 1988. **263**(15): p. 7302-7308.
17. Setif, P.Q. and H. Bottin, *Laser flash absorption spectroscopy study of ferredoxin reduction by photosystem I: spectral and kinetic evidence for the existence of several photosystem I-ferredoxin complexes.* Biochemistry, 1995. **34**(28): p. 9059-9070.
18. Toporik, H., et al., *Large photovoltages generated by plant photosystem I crystals.* Advanced Materials, 2012. **24**(22): p. 2988-2991.
19. Jordan, P., et al., *Three-dimensional structure of cyanobacterial photosystem I at 2.5 angstrom resolution.* Nature, 2001. **411**(6840): p. 909-917.
20. Ko, B.S., et al., *Effect of surface composition on the adsorption of photosystem I onto alkanethiolate self-assembled monolayers on gold.* 2004. **20**(10): p. 4033-4038.
21. Das, R., et al., *Integration of photosynthetic protein molecular complexes in solid-state electronic devices.* 2004. **4**(6): p. 1079-1083.
22. Carmeli, I., et al., *Photovoltaic activity of photosystem I-based self-assembled monolayer.* 2007. **129**(41): p. 12352-12353.

23. Frolov, L., et al., *Fabrication of a photoelectronic device by direct chemical binding of the photosynthetic reaction center protein to metal surfaces.* 2005. **17**(20): p. 2434-2437.
24. Ciesielski, P.N., et al., *Photosystem I–Based biohybrid photoelectrochemical cells.* Bioresource technology, 2010. **101**(9): p. 3047-3053.
25. LeBlanc, G., et al., *Photosystem I protein films at electrode surfaces for solar energy conversion.* Langmuir, 2014. **30**(37): p. 10990-11001.
26. Lee, I., J.W. Lee, and E.J.P.R.L. Greenbaum, *Biomolecular electronics: vectorial arrays of photosynthetic reaction centers.* 1997. **79**(17): p. 3294.
27. Mukherjee, D., et al., *Controlling the Morphology of Photosystem I Assembly on Thiol-Activated Au Substrates.* Langmuir, 2010. **26**(20): p. 16048-16054.
28. Mukherjee, D., et al., *Modulation of cyanobacterial photosystem I deposition properties on alkanethiolate Au substrate by various experimental conditions.* Colloids and Surfaces B: Biointerfaces, 2011. **88**(1): p. 181-190.
29. Wink, T., et al., *Self-assembled monolayers for biosensors.* Analyst, 1997. **122**(4): p. 43R-50R.
30. Mukherjee, D., M. May, and B. Khomami, *Detergent–protein interactions in aqueous buffer suspensions of Photosystem I (PS I).* Journal of colloid and interface science, 2011. **358**(2): p. 477-484.
31. Ciesielski, P.N., et al., *Enhanced photocurrent production by photosystem I multilayer assemblies.* Advanced Functional Materials, 2010. **20**(23): p. 4048-4054.
32. Frolov, L., et al., *Fabrication of Oriented Multilayers of Photosystem I Proteins on Solid Surfaces by Auto-Metallization.* Advanced Materials, 2008. **20**(2): p. 263-266.
33. Stieger, K.R., et al., *Engineering of supramolecular photoactive protein architectures: the defined co-assembly of photosystem I and cytochrome c using a nanoscaled DNA-matrix.* Nanoscale, 2016. **8**(20): p. 10695-10705.
34. Stieger, K., et al., *Biohybrid architectures for efficient light-to-current conversion based on photosystem I within scalable 3D mesoporous electrodes.* Journal of Materials Chemistry A, 2016. **4**(43): p. 17009-17017.
35. LeBlanc, G., et al., *Enhanced photocurrents of photosystem I films on p-doped silicon.* Advanced Materials, 2012. **24**(44): p. 5959-5962.
36. Kaniber, S.M., et al., *On-Chip Functionalization of Carbon Nanotubes with Photosystem I.* Journal of the American Chemical Society, 2010. **132**(9): p. 2872-2873.
37. Gunther, D., et al., *Photosystem I on graphene as a highly transparent, photoactive electrode.* Langmuir, 2013. **29**(13): p. 4177-4180.
38. LeBlanc, G., et al., *Integration of photosystem I with graphene oxide for photocurrent enhancement.* Advanced Energy Materials, 2014. **4**(9): p. 1301953.
39. Darby, E., et al., *Photoactive films of photosystem I on transparent reduced graphene oxide electrodes.* Langmuir, 2014. **30**(29): p. 8990-8994.
40. Kaniber, S.M., et al., *The optoelectronic properties of a photosystem I–carbon nanotube hybrid system.* Nanotechnology, 2009. **20**(34): p. 345701.
41. Feifel, S.C., et al., *Unidirectional photocurrent of photosystem I on π-system-modified graphene electrodes: nanobionic approaches for the construction of photobiohybrid systems.* Langmuir, 2015. **31**(38): p. 10590-10598.
42. Feifel, S., et al., *High photocurrent generation by photosystem I on artificial interfaces composed of π-system-modified graphene.* Journal of Materials Chemistry A, 2015. **3**(23): p. 12188-12196.

43. Kiliszek, M., et al., *Orientation of photosystem I on graphene through cytochrome c 553 leads to improvement in photocurrent generation.* Journal of Materials Chemistry A, 2018. **6**(38): p. 18615-18626.
44. Gizzie, E.A., et al., *Electrochemical Preparation of Photosystem I–Polyaniline Composite Films for Biohybrid Solar Energy Conversion.* ACS applied materials & interfaces, 2015. **7**(18): p. 9328-9335.
45. Badura, A., et al., *Photocurrent generation by photosystem 1 integrated in crosslinked redox hydrogels.* Energy & Environmental Science, 2011. **4**(7): p. 2435-2440.
46. Beam, J.C., et al., *Construction of a Semiconductor–Biological Interface for Solar Energy Conversion: p-Doped Silicon/Photosystem I/Zinc Oxide.* Langmuir, 2015. **31**(36): p. 10002-10007.
47. Lubner, C.E., et al., *Wiring photosystem I for direct solar hydrogen production.* 2009. **49**(3): p. 404-414.
48. Lubner, C.E., et al., *Solar hydrogen-producing bionanodevice outperforms natural photosynthesis.* Proceedings of the National Academy of Sciences, 2011. **108**(52): p. 20988-20991.
49. Terasaki, N., et al., *Bio-photosensor: Cyanobacterial photosystem I coupled with transistor via molecular wire.* Biochimica et Biophysica Acta (BBA)-Bioenergetics, 2007. **1767**(6): p. 653-659.
50. Frolov, L., et al., *Photoelectric junctions between GaAs and photosynthetic reaction center protein.* The Journal of Physical Chemistry C, 2008. **112**(35): p. 13426-13430.
51. Grimme, R.A., et al., *Photosystem I/molecular wire/metal nanoparticle bioconjugates for the photocatalytic production of H2.* Journal of the American Chemical Society, 2008. **130**(20): p. 6308-6309.
52. Iwuchukwu, I.J., et al., *Self-organized photosynthetic nanoparticle for cell-free hydrogen production.* Nature nanotechnology, 2010. **5**(1): p. 73.
53. Efrati, A., et al., *Assembly of photo-bioelectrochemical cells using photosystem I-functionalized electrodes.* Nature Energy, 2016. **1**(2): p. 1-8.
54. Moya, I., et al., *Time-resolved fluorescence analysis of the photosystem II antenna proteins in detergent micelles and liposomes.* Biochemistry, 2001. **40**(42): p. 12552-12561.
55. Akhtar, P., et al., *Pigment interactions in light-harvesting complex II in different molecular environments.* Journal of biological chemistry, 2015. **290**(8): p. 4877-4886.
56. Ogren, J.I., et al., *Impact of the lipid bilayer on energy transfer kinetics in the photosynthetic protein LH2.* Chemical science, 2018. **9**(12): p. 3095-3104.
57. Bennett, T.H., et al., *Jolly green MOF: confinement and photoactivation of photosystem I in a metal–organic framework.* Nanoscale Advances, 2019. **1**(1): p. 94-104.
58. Niroomand, H., et al., *Lipid-detergent phase transitions during detergent-mediated liposome solubilization.* The Journal of membrane biology, 2016. **249**(4): p. 523-538.
59. Niroomand, H., D. Mukherjee, and B. Khomami, *Tuning the photoexcitation response of cyanobacterial Photosystem I via reconstitution into Proteoliposomes.* Scientific reports, 2017. **7**(1): p. 2492.
60. Niroomand, H., et al., *Microenvironment alterations enhance photocurrents from photosystem I confined in supported lipid bilayers.* 2018.
61. Zapata-Herrera, M., et al., *Quantum Confinement Effects on the Near Field Enhancement in Metallic Nanoparticles.* Plasmonics, 2018. **13**(1): p. 1-7.

62. Hutter, E. and J.H. Fendler, *Exploitation of localized surface plasmon resonance.* Advanced materials, 2004. **16**(19): p. 1685-1706.
63. Petryayeva, E. and U.J. Krull, *Localized surface plasmon resonance: Nanostructures, bioassays and biosensing—A review.* Analytica chimica acta, 2011. **706**(1): p. 8-24.
64. Wei, Q.-H., et al., *Plasmon resonance of finite one-dimensional Au nanoparticle chains.* Nano letters, 2004. **4**(6): p. 1067-1071.
65. Murray, W.A. and W.L. Barnes, *Plasmonic materials.* Advanced materials, 2007. **19**(22): p. 3771-3782.
66. Rycenga, M., et al., *Controlling the synthesis and assembly of silver nanostructures for plasmonic applications.* Chemical reviews, 2011. **111**(6): p. 3669-3712.
67. Lakowicz, J. and Y. Fu, *Modification of single molecule fluorescence near metallic nanostructures.* Laser & photonics reviews, 2009. **3**(1-2): p. 221-232.
68. Anger, P., P. Bharadwaj, and L. Novotny, *Enhancement and quenching of single-molecule fluorescence.* Physical review letters, 2006. **96**(11): p. 113002.
69. Aslan, K., et al., *Metal-enhanced fluorescence: an emerging tool in biotechnology.* Current opinion in biotechnology, 2005. **16**(1): p. 55-62.
70. Koo Lee, Y.-E., R. Smith, and R. Kopelman, *Nanoparticle PEBBLE sensors in live cells and in vivo.* Annual review of analytical chemistry, 2009. **2**: p. 57-76.
71. Jeong, N.C., C. Prasittichai, and J.T. Hupp, *Photocurrent enhancement by surface plasmon resonance of silver nanoparticles in highly porous dye-sensitized solar cells.* Langmuir, 2011. **27**(23): p. 14609-14614.
72. Lin, S.-J., et al., *Plasmon-enhanced photocurrent in dye-sensitized solar cells.* Solar Energy, 2012. **86**(9): p. 2600-2605.
73. Nieder, J.B., R. Bittl, and M.J.A.C.I.E. Brecht, *Fluorescence studies into the effect of plasmonic interactions on protein function.* 2010. **49**(52): p. 10217-10220.
74. Kim, I., et al., *Metal nanoparticle plasmon-enhanced light-harvesting in a photosystem I thin film.* Nano letters, 2011. **11**(8): p. 3091-3098.
75. Brecht, M., et al., *Plasmonic interactions of photosystem I with Fischer patterns made of Gold and Silver.* Chemical Physics, 2012. **406**: p. 15-20.
76. Ashraf, I., et al., *Temperature dependence of metal-enhanced fluorescence of photosystem I from Thermosynechococcus elongatus.* Nanoscale, 2017. **9**(12): p. 4196-4204.
77. Czechowski, N., et al., *Large plasmonic fluorescence enhancement of cyanobacterial photosystem I coupled to silver island films.* 2014. **105**(4): p. 043701.
78. Govorov, A.O. and I.J.N.l. Carmeli, *Hybrid structures composed of photosynthetic system and metal nanoparticles: plasmon enhancement effect.* 2007. **7**(3): p. 620-625.
79. Niroomand, H., et al., *Microenvironment alterations enhance photocurrents from photosystem I confined in supported lipid bilayers.* Journal of Materials Chemistry A, 2018. **6**(26): p. 12281-12290.
80. Pamu, R., et al., *Plasmon-enhanced photocurrent from photosystem I assembled on Ag nanopyramids.* The journal of physical chemistry letters, 2018. **9**(5): p. 970-977.
81. Nelson, N. and C.F.J.A.R.P.B. Yocum, *Structure and function of photosystems I and II.* 2006. **57**: p. 521-565.
82. Nelson, N.J.J.o.n. and nanotechnology, *Plant photosystem I–the most efficient nano-photochemical machine.* 2009. **9**(3): p. 1709-1713.
83. Fromme, P., P. Jordan, and N. Krauß, *Structure of photosystem I.* Biochimica et Biophysica Acta (BBA)-Bioenergetics, 2001. **1507**(1-3): p. 5-31.

84. Setif, P.Q. and H.J.B. Bottin, *Laser flash absorption spectroscopy study of ferredoxin reduction by photosystem I in Synechocystis sp. PCC 6803: evidence for submicrosecond and microsecond kinetics.* 1994. **33**(28): p. 8495-8504.
85. Andrews, D.L., *Photonics, Biomedical Photonics, Spectroscopy, and Microscopy*. 2015, NewJersey: Wiley.
86. Saboe, P.O., et al., *Biomimetic wiring and stabilization of photosynthetic membrane proteins with block copolymer interfaces.* Journal of Materials Chemistry A, 2016. **4**(40): p. 15457-15463.
87. Lubner, C.E., et al., *Wiring photosystem I for electron transfer to a tethered redox dye.* Energy & Environmental Science, 2011. **4**(7): p. 2428-2434.
88. Ciesielski, P.N., et al., *Functionalized nanoporous gold leaf electrode films for the immobilization of photosystem I.* ACS Nano, 2008. **2**(12): p. 2465-2472.
89. Ciobanu, M., et al., *Electrochemistry and photoelectrochemistry of photosystem I adsorbed on hydroxyl-terminated monolayers.* Journal of Electroanalytical Chemistry, 2007. **599**(1): p. 72-78.
90. Bennett, T., et al., *Elucidating the role of methyl viologen as a scavenger of photoactivated electrons from photosystem I under aerobic and anaerobic conditions.* Physical Chemistry Chemical Physics, 2016. **18**(12): p. 8512-8521.
91. Carmeli, I., et al., *Broad band enhancement of light absorption in photosystem I by metal nanoparticle antennas.* Nano letters, 2010. **10**(6): p. 2069-2074.
92. Dulkeith, E., et al., *Fluorescence quenching of dye molecules near gold nanoparticles: radiative and nonradiative effects.* Physical review letters, 2002. **89**(20): p. 203002.
93. Akiyama, T., et al., *Photocurrent enhancement in a porphyrin-gold nanoparticle nanostructure assisted by localized plasmon excitation.* Chemical communications, 2006(4): p. 395-397.
94. Qi, J., et al., *Highly efficient plasmon-enhanced dye-sensitized solar cells through metal@ oxide core–shell nanostructure.* ACS nano, 2011. **5**(9): p. 7108-7116.
95. Standridge, S.D., G.C. Schatz, and J.T. Hupp, *Distance dependence of plasmon-enhanced photocurrent in dye-sensitized solar cells.* Journal of the American Chemical Society, 2009. **131**(24): p. 8407-8409.
96. Kim, S.-S., et al., *Plasmon enhanced performance of organic solar cells using electrodeposited Ag nanoparticles.* Applied Physics Letters, 2008. **93**(7): p. 305.
97. Yoon, W.-J., et al., *Plasmon-enhanced optical absorption and photocurrent in organic bulk heterojunction photovoltaic devices using self-assembled layer of silver nanoparticles.* Solar Energy Materials and Solar Cells, 2010. **94**(2): p. 128-132.
98. Friebe, V.M., et al., *Plasmon-enhanced photocurrent of photosynthetic pigment proteins on nanoporous silver.* Advanced Functional Materials, 2016. **26**(2): p. 285-292.
99. Yen, C.-W., L.-K. Chu, and M.A. El-Sayed, *Plasmonic field enhancement of the bacteriorhodopsin photocurrent during its proton pump photocycle.* Journal of the American Chemical Society, 2010. **132**(21): p. 7250-7251.
100. Hussels, M., et al., *Interactions of Photosystem I with Plasmonic nanostructures.* Acta Physica Polonica, A., 2012. **122**(2).
101. Terasaki, N., et al., *Fabrication of novel photosystem I–gold nanoparticle hybrids and their photocurrent enhancement.* Thin Solid Films, 2006. **499**(1-2): p. 153-156.

102. Le, R.K., et al., *Sortase-mediated ligation of PsaE-modified photosystem I from Synechocystis sp. PCC 6803 to a conductive surface for enhanced photocurrent production on a gold electrode.* 2015. **31**(3): p. 1180-1188.
103. Alloway, D.M., et al., *Tuning the effective work function of gold and silver using ω-functionalized alkanethiols: varying surface composition through dilution and choice of terminal groups.* The Journal of Physical Chemistry C, 2009. **113**(47): p. 20328-20334.
104. Alloway, D.M., et al., *Interface Dipoles Arising from Self-Assembled Monolayers on Gold: UV− Photoemission Studies of Alkanethiols and Partially Fluorinated Alkanethiols.* The Journal of Physical Chemistry B, 2003. **107**(42): p. 11690-11699.
105. Khan, M.Z.H., *Effect of ITO surface properties on SAM modification: A review toward biosensor application.* Cogent Engineering, 2016. **3**(1): p. 1170097.
106. Hong, J.-P., et al., *Tuning of Ag work functions by self-assembled monolayers of aromatic thiols for an efficient hole injection for solution processed triisopropylsilylethynyl pentacene organic thin film transistors.* Applied Physics Letters, 2008. **92**(14): p. 131.
107. Rusu, P.C. and G. Brocks, *Surface dipoles and work functions of alkylthiolates and fluorinated alkylthiolates on Au (111).* The Journal of Physical Chemistry B, 2006. **110**(45): p. 22628-22634.
108. Cornil, D. and J. Cornil, *Work-function modification of the (1 1 1) gold surface upon deposition of self-assembled monolayers based on alkanethiol derivatives.* Journal of Electron Spectroscopy and Related Phenomena, 2013. **189**: p. 32-38.
109. Feilchenfeld, H., G. Chumanov, and T.M. Cotton, *Photoreduction of methylviologen adsorbed on silver.* The Journal of Physical Chemistry, 1996. **100**(12): p. 4937-4943.
110. Jordan, P., et al., *Three-dimensional structure of cyanobacterial photosystem I at 2.5 Å resolution.* Nature, 2001. **411**(6840): p. 909.
111. Nelson, N. and C.F. Yocum, *Structure and function of photosystems I and II.* Annual Review of Plant Biology, 2006. **57**: p. 521-565.
112. Nguyen, K. and B.D. Bruce, *Growing green electricity: progress and strategies for use of photosystem I for sustainable photovoltaic energy conversion.* Biochimica et Biophysica Acta (BBA)-Bioenergetics, 2014. **1837**(9): p. 1553-1566.
113. Gordiichuk, P.I., et al., *Solid-State Biophotovoltaic Cells Containing Photosystem I.* Advanced Materials, 2014. **26**(28): p. 4863-4869.
114. Niroomand, H., et al., *Tuning the photocurrent generations from photosystem I assembled in tailored biotic–abiotic interfaces.* Mrs Communications, 2018. **8**(3): p. 823-829.
115. Kinkhabwala, A., et al., *Large single-molecule fluorescence enhancements produced by a bowtie nanoantenna.* Nature Photonics, 2009. **3**(11): p. 654-657.
116. Shanthil, M., et al., *Ag@ SiO2 core–shell nanostructures: distance-dependent plasmon coupling and SERS investigation.* The journal of physical chemistry letters, 2012. **3**(11): p. 1459-1464.
117. Yao, K., et al., *Nano-bio hybrids of plasmonic metals/photosynthetic proteins for broad-band light absorption enhancement in organic solar cells.* Journal of Materials Chemistry A, 2016. **4**(35): p. 13400-13406.
118. Yang, Y., et al., *Plasmonic enhancement of biosolar cells employing light harvesting complex II incorporated with core–shell metal@ TiO2 nanoparticles.* Advanced Materials Interfaces, 2016. **3**(15): p. 1600371.

119. Yen, C.-W., et al., *Tailoring plasmonic and electrostatic field effects to maximize solar energy conversion by bacteriorhodopsin, the other natural photosynthetic system.* Nano letters, 2011. **11**(9): p. 3821-3826.
120. Ashraf, I., et al. *Effects of Irregular Bimetallic Nanostructures on the Optical Properties of Photosystem I from Thermosynechococcus elongatus*. in *Photonics*. 2015. Multidisciplinary Digital Publishing Institute.
121. Zeng, Z., et al., *Plasmon–Exciton Coupling in Photosystem I Based Biohybrid Photoelectrochemical Cells.* ACS Applied Bio Materials, 2018. **1**(3): p. 802-807.
122. Szalkowski, M., et al., *Plasmon-induced absorption of blind chlorophylls in photosynthetic proteins assembled on silver nanowires.* Nanoscale, 2017. **9**(29): p. 10475-10486.
123. Stamatakis, K., M. Tsimilli-Michael, and G.C. Papageorgiou, *On the question of the light-harvesting role of β-carotene in photosystem II and photosystem I core complexes.* Plant physiology and biochemistry, 2014. **81**: p. 121-127.
124. Fraser, N.J., H. Hashimoto, and R.J. Cogdell, *Carotenoids and bacterial photosynthesis: The story so far.* Photosynthesis research, 2001. **70**(3): p. 249-256.
125. Triantaphylides, C., et al., *Singlet oxygen is the major reactive oxygen species involved in photooxidative damage to plants.* Plant physiology, 2008. **148**(2): p. 960-968.
126. Wang, Y., L. Mao, and X. Hu, *Insight into the structural role of carotenoids in the Photosystem I: a quantum chemical analysis.* Biophysical journal, 2004. **86**(5): p. 3097-3111.
127. Badura, A., et al., *Wiring photosynthetic enzymes to electrodes.* Energy & Environmental Science, 2011. **4**(9): p. 3263-3274.
128. Mukherjee, D., et al., *Modulation of cyanobacterial Photosystem I deposition properties on alkanethiolate Au substrate by various experimental conditions.* Colloids and Surfaces B: Biointerfaces, 2011. **88**: p. 181 - 190.
129. Terasaki, et al., *Plugging a Molecular Wire into Photosystem I: Reconstitution of the Photoelectric Conversion System on a Gold Electrode.* Angewandte Chemie, 2009. **48**(9): p. 1585-1587.
130. Manocchi, A.K., et al., *Photocurrent generation from surface assembled photosystem I on alkanethiol modified electrodes.* Langmuir, 2013. **29**(7): p. 2412-9.
131. Carmeli, I., et al., *A photosynthetic reaction center covalently bound to carbon nanotubes.* Advanced Materials, 2007. **19**(22): p. 3901-3905.
132. Mershin, A., et al., *Self-assembled photosystem-I biophotovoltaics on nanostructured TiO 2 and ZnO.* Scientific Reports, 2012. **2**: p. 234.
133. Czechowski, N., et al., *Large plasmonic fluorescence enhancement of cyanobacterial photosystem I coupled to silver island films.* Applied Physics Letters, 2014. **105**(4): p. 043701.
134. Terasaki, N., et al., *Fabrication of novel photosystem I-gold nanoparticle hybrids and their photocurrent enhancement.* Thin Solid Films, 2006. **499**(1-2): p. 153-156.
135. Gerster, D., et al., *Photocurrent of a single photosynthetic protein.* Nat Nano, 2012. **7**(10): p. 673-676.
136. LeBlanc, G., et al., *Photoreduction of Catalytic Platinum Particles Using Immobilized Multilayers of Photosystem I.* Langmuir, 2012. **28**(21): p. 7952-7956.
137. LeBlanc, G., et al., *Integration of Photosystem I with Graphene Oxide for Photocurrent Enhancement.* Advanced Energy Materials, 2014. **4**(9): p. 5.

138. Frolov, L., et al., *Fabrication of oriented multilayers of photosystem I proteins on solid surfaces by auto-metallization.* Advanced Materials, 2008. **20**(2): p. 263-266.
139. Terasaki, N., et al., *Photosensor Based on an FET Utilizing a Biocomponent of Photosystem I for Use in Imaging Devices.* Langmuir, 2009. **25**(19): p. 11969-11974.
140. Terasaki, N., et al., *Plugging a Molecular Wire into Photosystem I: Reconstitution of the Photoelectric Conversion System on a Gold Electrode.* Angewandte Chemie International Edition, 2009. **48**(9): p. 1585-1587.
141. Terasaki, N., et al., *Bio-photosensor: Cyanobacterial photosystem I coupled with transistor via molecular wire.* Biochimica et Biophysica Acta (BBA) - Bioenergetics, 2007. **1767**(6): p. 653-659.
142. Le, R.K., et al., *Sortase-mediated ligation of PsaE-modified photosystem I from Synechocystis sp. PCC 6803 to a conductive surface for enhanced photocurrent production on a gold electrode.* Langmuir, 2015. **31**(3): p. 1180-1188.
143. Mukherjee, D., M. May, and B. Khomami, *Detergent-protein interactions in aqueous buffer suspensions of Photosystem I (PS I).* Journal of Colloid and Interface Science, 2011. **358**(2): p. 477-484.
144. LeBlanc, G., et al., *Enhanced photocurrents of photosystem I films on p-doped silicon.* Advanced Materials, 2012. **24**(44): p. 5959-62.
145. Badura, A., et al., *Photocurrent generation by photosystem 1 integrated in crosslinked redox hydrogels.* Energy & Environmental Science, 2011. **4**(7): p. 2435-2440.
146. Baker, D.R., et al., *Comparative photoactivity and stability of isolated cyanobacterial monomeric and trimeric Photosystem I.* The Journal of Physical Chemistry B, 2014. **118**(10): p. 2703-2711.
147. Robinson, M., et al., *Photocatalytic photosystem I/PEDOT composite films prepared by vapor-phase polymerization.* Nanoscale, 2017. **9**(18): p. 6158-6166.
148. Gizzie, E.A., et al., *Electrochemical Preparation of Photosystem I–Polyaniline Composite Films for Biohybrid Solar Energy Conversion.* ACS Applied Materials & Interfaces, 2015.
149. Cherubin, A., et al., *Encapsulation of Photosystem I in Organic Microparticles Increases Its Photochemical Activity and Stability for Ex Vivo Photocatalysis.* ACS Sustainable Chemistry & Engineering, 2019.
150. Bennett, T.H., et al., *Augmented photocurrents from Photosystem I embedded in zinc and imidazole based TCNQ charge transfer salt films derived from ZIF-8.* ChemNanoMat, 2019. **In Submission.**
151. Yang, Z., et al., *Effect of phosphatidylglycerol on molecular organization of photosystem I.* Biophysical chemistry, 2005. **115**(1): p. 19-27.
152. Nabedryk, E., et al., *Conformation and orientation of chlorophyll-proteins in photosystem I by circular dichroism and polarized infrared spectroscopies.* Biochimica et Biophysica Acta (BBA)-Bioenergetics, 1984. **767**(3): p. 640-647.
153. Niroomand, H., et al., *Tuning the photocurrent generations from photosystem I assembled in tailored biotic–abiotic interfaces.* MRS Communications, 2018: p. 1-7.
154. Niroomand, H., D. Mukherjee, and B. Khomami, *Tuning the photoexcitation response of cyanobacterial Photosystem I via reconstitution into Proteoliposomes.* Scientific Reports, 2017. **7**.
155. Niroomand, H., et al., *Lipid-Detergent Phase Transitions During Detergent-Mediated Liposome Solubilization.* Journal of Membrane Biology, 2016. **249**(4): p. 523-538.

156. Son, M., et al., *Dissipative Pathways in Light-Harvesting Complex II Are Controlled by the Plant Membrane.* 2019.
157. Saboe, P.O., et al., *Two-Dimensional Protein Crystals for Solar Energy Conversion.* Advanced Materials, 2014. **26**(41): p. 7064-7069.
158. Fromme, P. and H.T. Witt, *Improved isolation and crystallization of photosystem I for structural analysis.* Biochimica et Biophysica Acta (BBA)-Bioenergetics, 1998. **1365**(1-2): p. 175-184.
159. Lichtenberg D, B.Y., *Liposomes: preparation, characterization, and preservation, methods of biochemical analysis*. 2006, Newyork: Wiley.
160. Whitmore, L. and B.A. Wallace, *Protein secondary structure analyses from circular dichroism spectroscopy: methods and reference databases.* Biopolymers: Original Research on Biomolecules, 2008. **89**(5): p. 392-400.
161. Sreerama, N. and R.W. Woody, *Estimation of protein secondary structure from circular dichroism spectra: comparison of CONTIN, SELCON, and CDSSTR methods with an expanded reference set.* Analytical biochemistry, 2000. **287**(2): p. 252-260.
162. Franck, F., P. Juneau, and R. Popovic, *Resolution of the photosystem I and photosystem II contributions to chlorophyll fluorescence of intact leaves at room temperature.* Biochimica et Biophysica Acta (BBA)-Bioenergetics, 2002. **1556**(2-3): p. 239-246.
163. Papageorgiou, G.C., *Chlorophyll a fluorescence: a signature of photosynthesis*. Vol. 19. 2007: Springer Science & Business Media.
164. Shang, L., et al., *pH-dependent protein conformational changes in albumin: gold nanoparticle bioconjugates: a spectroscopic study*. Langmuir, 2007. **23**(5): p. 2714-2721.
165. Balleza, D., et al., *Ether-versus ester-linked phospholipid bilayers containing either linear or branched apolar chains.* Biophysical journal, 2014. **107**(6): p. 1364-1374.
166. Relat-Goberna, J., A.E. Beedle, and S. Garcia-Manyes, *The nanomechanics of lipid multibilayer stacks exhibits complex dynamics.* small, 2017. **13**(24): p. 1700147.
167. Ranjbar, B. and P. Gill, *Circular dichroism techniques: biomolecular and nanostructural analyses-a review.* Chemical biology & drug design, 2009. **74**(2): p. 101-120.
168. Philipson, K.D., V.L. Sato, and K. Sauer, *Exciton interaction in the photosystem I reaction center from spinach chloroplasts. Absorption and circular dichroism difference spectra.* Biochemistry, 1972. **11**(24): p. 4591-4595.
169. Somsen, O., R. van Grondelle, and H. van Amerongen, *Spectral broadening of interacting pigments: polarized absorption by photosynthetic proteins.* Biophysical journal, 1996. **71**(4): p. 1934-1951.
170. Herczenik, E. and M.F. Gebbink, *Molecular and cellular aspects of protein misfolding and disease.* The FASEB Journal, 2008. **22**(7): p. 2115-2133.
171. Melby, L., et al., *Substituted quinodimethans. II. Anion-radical derivatives and complexes of 7, 7, 8, 8-tetracyanoquinodimethan.* Journal of the American Chemical Society, 1962. **84**(17): p. 3374-3387.
172. Mukherjee, D. and M.D. Cheng, *Characterization of carbon-containing aerosolized drugs using laser-induced breakdown spectroscopy.* Applied Spectroscopy, 2008. **62**(5): p. 554-562.
173. Mukherjee, D. and M.D. Cheng, *Quantitative analysis of carbonaceous aerosols using laser-induced breakdown spectroscopy: a study on mass loading induced plasma matrix effects.* Journal of Analytical Atomic Spectrometry, 2008. **23**(1): p. 119-128.

Appendices

Appendix I

1. Prototypical Photocurrent data:

Table AI.1 Photocurrents data in nA/cm^2 for the three-electrode (ITO, Planar Ag and AgNP/ITO) constructs at 4 different wavelength light illumination having same power density of ~36 mW/cm^2

Wavelength (nm)	ITO	SAM /ITO	PSI /SAM /ITO	PlanarAg	SAM /PlanarAg	PSI /SAM /PlanarAg	AgNP /ITO	SAM /AgNP /ITO	PSI /SAM /AgNP /ITO
395	13	7.5	47.5	49	178	336	110	280	333
420	4	3	25.9	31.5	100	187	62	114	346.5
470	4	1	13.3	9.5	79	116	9.5	124	347
660	0.5	0	8.7	1.8	14.25	21	1	30	88.5

2. Plasmon Induced Photocurrent Enhancement Factors calculations:

3.656 µm x 3.342 µm area of the SEM image for Ag-NP/ITO was analyzed using ImageJ software and the following quantities were in turn evaluated.

The number density of the pyramids = $Ag\text{-}NP_{count}$ = 692958314.5 cm^{-2}

Average pyramid base area (2D projected) = *Base* = 14024.75996 nm^2

Total apparent working area estimate (considering Ag-NP as 2D Δ plate) = 1 unit = sum of total apparent Ag-NP area and ITO area.

Apparent total Ag-NP area = *Base* x $Ag\text{-}NP_{count}$= 0.09718 unit.

Apparent ITO area = 1-*Base*. $AgNP_{count}$ = 0.90282 unit.

This number is close to the ideal hexagonal circle packing value of 0.9069.

From the figure AI.1: curved ΔDEF area = ΔABC – sector areas (ADE + BDF + CEF)

$$= \frac{\sqrt{3}}{4} AB^2 - (\frac{3}{2} r\theta^2)$$

Since the ΔABC is equilateral triangle, θ = angle at ΔABC corners (60^0) and r = radius of the circles

The arc ΔDEF area as 'Base' area evaluated from the SEM analysis are used to evaluate the r value, r = 294.915 nm.

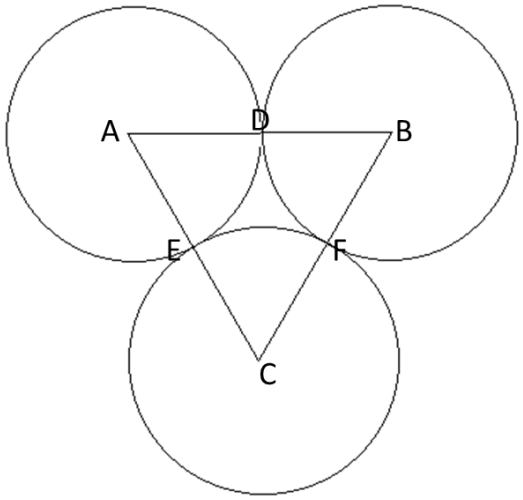

Figure AI.1. Model of NSL arc triangle and spherical bead shadows.

The side length of the curved triangle is DE=EF=DF= rθ = 308.835 nm

Since the Ag-NP is a triangular pyramid chopped at the top. In other words, the base triangle projected upwards while the side lengths reduce to form an upper small size triangle. Using the AFM analysis of 25 Ag-NP, the ratio of upper triangle side length to base triangular side is 0.421 on average. This implies the upper Δ side length as 130 nm for the 308.835nm base Δ side length.

Using this information, the surface area of a single Ag-NP = top triangle area + 3 trapezoidal surfaces on each side can be accurately estimated.

Single AgNP surface area = *Surface Area* = 60587.9658 nm^2

To turn the apparent working area to an actual working area, the 'Base' area must be converted to an equivalent 3D *Surface Area*. With this projection, the apparent ITO area won't change.

So, the total working area = $(1 - Base.AgNP_{count}) + Base.AgNP_{count}.\frac{SurfaceArea_{AgNP}}{Base}$

= 1.3226 units

Therefore, a nominal 1 cm^2 area of our electrode has a true surface area of 1.323 cm^2 due to the area added by the nanopyramids.

Total Ag-NP area = $Ag\text{-}NP_{area} = Base.AgNP_{count} . \frac{SurfaceArea_{AgNP}}{Base} = 0.4198$

Fraction of ITO area = $fAREA_{ITO} = \frac{1-Base.NSL_{count}}{Total\ working\ area} = 0.680$

Fraction of Ag-NP area = $fAREA_{AgNP}$ = 1- fraction of ITO area = 0.32

So, after taking into account the nanopyramids, our surface is 68% ITO and 32% silver, whereas the nominal 2D projected areas are 90.3% and 9.7% respectively.

PSI trimers number density

Five different 0.3 µm x0.3 µm spots of PSI/SAM/ITO electrode surface AFM images were chosen and counted the PSI trimer units. The average PSI density on the ITO =

$\#PSI_{ITO} = 7.8 \times 10^{10} cm^{-2}$.

Similarly estimated, the PSI density on ITO areas of PSI/SAM/Ag-NP/ITO electrode surface = $\#PSI_{ITONSL} = 4.733 \times 10^{10} cm^{-2}$

Two different 2 µm x2 µm AFM image of PSI/SAM/Planar Ag electrode surface was used to count all the PSI trimer units. The average PSI density on the Planar Ag is $\#PSI_{Ag} = 3.064\times 10^{10} cm^{-2}$.

From the AFM phase images of PSI/C6/AgNP/ITO, number of PSI counted on 22 AgNP and the PSI density on AgNP is = $\#PSI_{AgNP} = 7.592 \times 10^{10} cm^{-2}$

Estimating the number of photoelectrons per PSI trimer per second on each electrode:

The rate of photoelectrons per PSI trimer for PSIs on SAM/ITO ($\boldsymbol{P_{ITO}}$) and PSI on SAM/Planar Ag ($\boldsymbol{P_{Ag}}$) electrodes at the 4 excitation wavelengths can be calculated from effective photocurrent densities and PSI number densities using following equation.

$$\boldsymbol{P_{ITO}, P_{Ag}} = \frac{\#photoelectrons}{(PSI\ trimer)s} = \frac{Effective\ PSI\ photocurrent\ (\frac{nA}{cm^2}) \times 6.2415 \times 10^9}{PSI\ trimers\ number\ density}$$

For the PSI/SAM/AgNP/ITO, the effective PSI photocurrent density reported in Figure 5(a) is according to the apparent working area. It must be corrected to include the improved surface area due to AgNP height.

Corrected photocurrent density = $\frac{Effective\ photocurrent\ density}{1.3226}$

Since this photocurrent is composed of two contributions, one from PSI attached to ITO area and the other from PSI attached to AgNP area.

$$\frac{Effective\ photocurrent\ density}{1.3226} = \left(fAREA_{ITO} \times \frac{Effective\ PSI\ photocurrent\ on\ ITO\ \left(\frac{nA}{cm^2}\right)}{\#PSI_{ITO}} \times \#PSI_{ITONSL} \right) + (fAREA_{AgNP} \times \boldsymbol{A} \times \#PSI_{AgNP})$$

where $\boldsymbol{A} = \frac{\boldsymbol{Effective\ PSI\ photocurrent\ of\ PSI\ on\ AgNP\ (nA)}}{\boldsymbol{PSI\ trimer}}$

'$\boldsymbol{P_{AgNP}}$' = $\frac{\#photoelectrons}{(PSI\ trimer)s}$ = $\boldsymbol{A} \times 6.2415 \times 10^9$ for PSI on Ag-NP area.

The final evaluated photoelectrons per PSI values are calculated using the effective photocurrents and the final mean values are reported in following table. These values are used for determining the final plasmon enhanced photocurrents by dividing the $\frac{\boldsymbol{P_{AgNP}}}{\boldsymbol{P_{Ag}}}$

Excitation wavelength (nm)	$\boldsymbol{P_{ITO}}$	$\boldsymbol{P_{Ag}}$	$\boldsymbol{P_{AgNP}}$	$\frac{\boldsymbol{P_{AgNP}}}{\boldsymbol{P_{Ag}}}$
395	3.30078	33.84881	3.9096	0.1128
420	2.06315	18.60497	45.22	2.430
470	1.04552	7.061739	41.446	5.870
660	0.91349	1.65509	10.722	6.476

Table AI.2: Wavelength and electrode substrate dependent rate of photoelectrons per PSI trimer; Wavelength dependent Plasmon enhancement factors

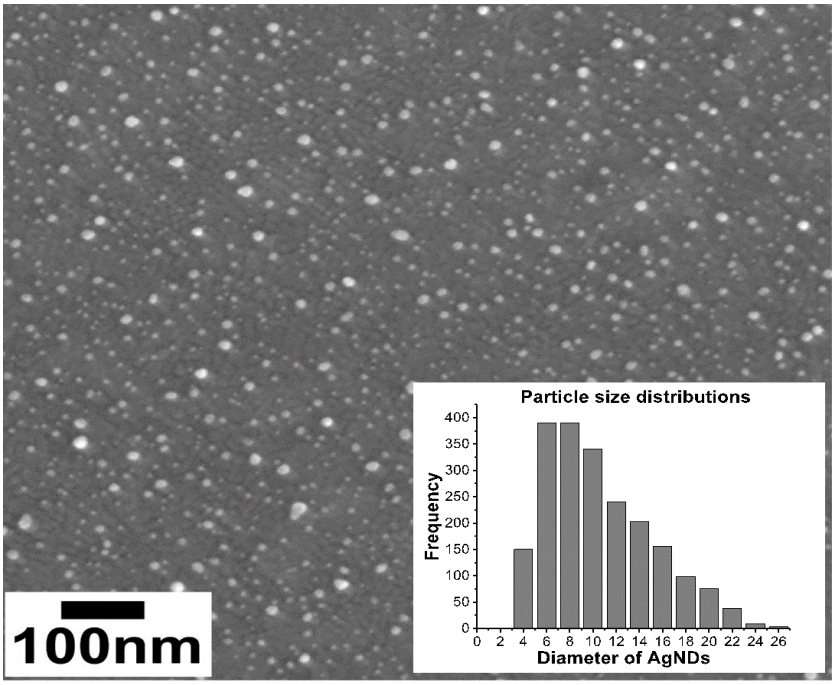

Figure AI.2 SEM image of AgND on ITO.

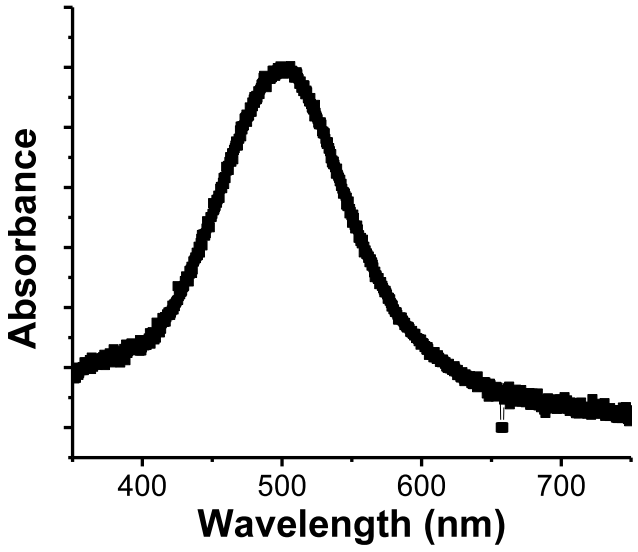

Figure AI.3 The plasmonic absorption of the AgND on ITO sample

3. Silver Nano-Dots (AgND) enhancement factor calculation:

A 3.262x2.184 μm^2 area of SEM image was analyzed using ImageJ software and following quantities were estimated.

Total apparent area = 7125478.046 nm^2

Total apparent AgND area = 182688.153 nm^2

Fraction of apparent AgND area = 0.025

Fraction of apparent ITO area = 0.975

Taking AgND as hemispheres the actual AgND area = 365376.306 nm^2

Fraction of actual AgND area, $fAREA_{AgND}$= 0.948

Fraction of actual ITO area, $fAREA_{ITO}$ = 0.052

Total actual area = 7308166.199 nm^2

Total area of increment = 1.0256

The enhancement factors estimated based on similar background references of planar Ag and planar ITO values of $\boldsymbol{P_{ITO}, P_{Ag}}$ used earlier for AgNP.

The PSI number density on ITO areas of PSI/C6/AgND/ITO substrate was taken as the $\#PSI_{ITONSL}$.

The PSI number density on AgND areas was calculated by assuming 1 PSI trimer per 1 AgND particle. $\#PSI_{AgND} = 57.365 \times 10^{10} cm^{-2}$. The assumption is reasonable since the median and mean of the AgNDs diameters are 8.55 nm and 10.5 nm respectively and 1 PSI trimer size is ~30 nm (see Figure AI.2). The maximum allowable density is 1 PSI trimer per AgND. The enhancement factors estimated from this assumption is conservative since the increasing the PSI density will decrease the enhancement factor. And the AgND density is 7 times higher than the $\#PSI_{AgNP}$.

Applying similar equations as in AgNP enhancement factor calculations:

$$\frac{Effective\ photocurrent\ density}{1.0256} = \left(fAREA_{ITO} \times \frac{Effective\ PSI\ photocurrent\ on\ ITO\ \left(\frac{nA}{cm^2}\right)}{\#PSI_{ITO}} \times \#PSI_{ITONSL} \right) + (fAREA_{AgND} \times \boldsymbol{A} \times \#PSI_{AgNP})$$

where $\boldsymbol{A} = \frac{\boldsymbol{Effective\ PSI\ photocurrent\ on\ AgNP\ (nA)}}{\boldsymbol{number\ of\ PSI\ trimers}}$

'$\boldsymbol{P_{AgND}}$' = $\frac{\#photoelectrons}{(PSI\ trimer)s}$ = $\boldsymbol{A} \times 6.2415 \times 10^9$ for PSI on AgND area.

The final enhancement factor values are calculated by the ratio of $\frac{\boldsymbol{P_{AgNP}}}{\boldsymbol{P_{Ag}}}$ and presented in the Figure AI.4.

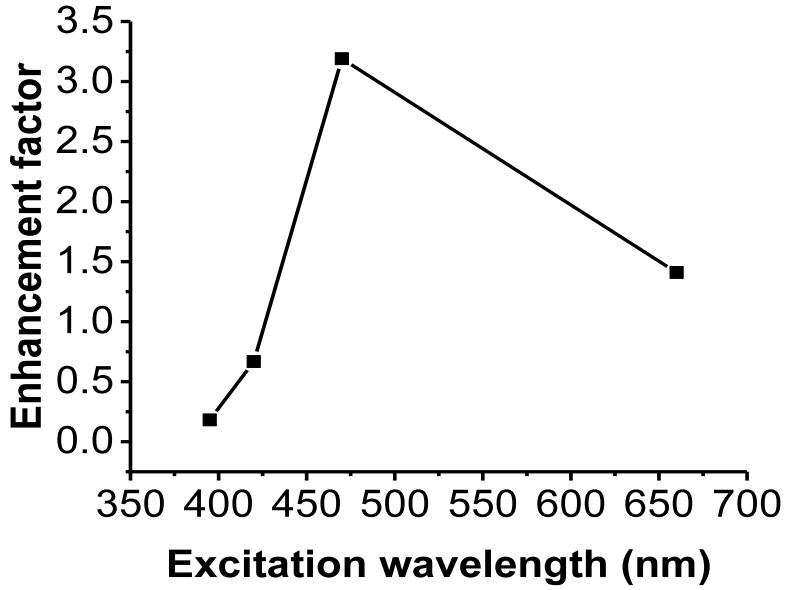

Figure AI.4 Plasmon induced photocurrent enhancement factors based on ratio of effective photocurrent per PSI on AgND to that from planar Ag.

Appendix II

1. Fraction of plasmon and non-plasmon working area calculations:

Gold Nano-Disks (AuND):

The height of the AuND determined from the AFM image (H_g) = 43 nm.

The FDTD simulations performed on a design that is similar to the developed AuND/ITO substrate using EBL. The periodic Nano-Disk patterns pitch =200 nm, height = 43 nm.

The optimal diameter of the AuND (D_g) = 112 nm where the absorbance spectrum matching with measured spectrum of the AuND/ITO developed.

The circular area of a single Nano-Disk = 9847.04 nm^2

The EBL patterning array size = $4\ mm \times 4\ mm$

With 200 nm pitch, total number of the Nano-Disks in the array (n)= $20000 \times 20000 = 4 \times 10^8$

Total circular area of the Nano-Disks (A_d)= $9847.04\ nm^2 \times 4 \times 10^8 = 3.9388\ mm^2$

The circular exposed area of the working electrode in the electrochemical cell based on inner diameter of the O-ring (A_O) = 30.19 mm^2

Since PSI is assembled only on exposed ITO areas, the working area can be reduced to exposed ITO working area (A_g).

(A_g)= $A_O - A_d$= 26.2512 mm^2.

The ITO area outside the ND square array (Total ITO working area not under LSPR) = 30.19 mm^2 – 16 mm^2 = 14.19 mm^2

Fraction of non-plasmonic ITO area (f_{nP}) = $\frac{14.19}{26.2512} = 0.54$

Fraction of ITO area under LSPR (f_P) = $\frac{26.2512-14.19}{26.2512} = 0.46$

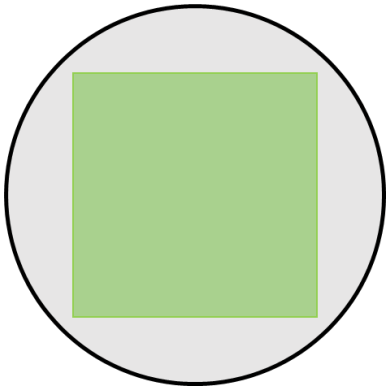

Figure AII.1. Depicting the electrochemical working area. The square part is nanopattern array of size 4mm x 4mm. The gray part is the ITO area (14.19 mm^2) located outside the ND array square. The circular part is the O-ring with inner diameter of 6.2 mm.

Silver Nano-Disk (AgND):

The analysis method followed is similar to the method followed above for AuND.

The height of the AgND determined from the AFM image (H_s) = 33 nm.

The optimal diameter of the AgND (D_s) = 76 nm

The circular area of a single Nano-Disk = 4534.16 nm^2

Total circular area of the Nano-Disks (A_s) = $4534.16\ nm^2 \times 4 \times 10^8 = 1.813\ mm^2$

Since PSI is assembled only on exposed ITO areas, the working area can be reduced to exposed ITO working area (A_s).

(A_g)= $A_O - A_d$= 28.377 mm^2.

The ITO area outside the ND square array (Total ITO working area not under LSPR) = 30.19 mm^2 – 16 mm^2 = 14.19 mm^2

Fraction of non-plasmonic ITO area (f_{nP}) = $\frac{14.19}{28.377} = 0.50$

Fraction of ITO area under LSPR (f_P) = $\frac{28.377-14.19}{28.377} = 0.50$

2. Plasmon induced photocurrent enhancement factor calculations:

Photocurrent density of PSI from ITO_{SAM} = $\mathbf{P_{ITO}}$ = measured eff. photocurrent density of PSI on ITO_{SAM}

Photocurrent density of PSI due to the LSPR of AuND or AgND = $\mathbf{P_{AuND}}$ or $\mathbf{P_{AgND}}$

$$(\text{Effective photocurrent density})_{(\text{AuND/ITO or AgND/ITO})} = (f_P \times \mathbf{P_{AuND\ or\ AgND}}) + (f_{nP} \times \mathbf{P_{ITO}}) \quad \textit{...equation I}$$

Where $(\text{Effective photocurrent density})_{(AuND/ITO\ or\ AgND/ITO)}$ = the measured effective photocurrent density of PSI on AuND/ITO or AgND/ITO.

f_P = fraction of area under localized plasmon electric field on AuND/ITO or AgND/ITO substrate

f_{nP} = fraction of non-plasmonic area under localized plasmon electric field on AuND/ITO or AgND/ITO substrate

The equation I is valid since, the measured eff. photocurrent density of PSI on AuND/ITO_{SAM} AgND/ITO_{SAM} is emanating from two type of PSI. One set of PSI located inside the LSPR field. Another set of PSI located outside of the LSPR field away from the nanopatterned array.

The f_P and f_{nP} for both the AuND/ITO and AgND/ITO are estimated in above section 1.

Finally, the $(\text{plasmon enhancement factor})_{\lambda exc} = \left(\frac{P_{AuND}}{P_{ITO}}\right)_{\lambda_{exc}}$ or $\left(\frac{P_{AgND}}{P_{ITO}}\right)_{\lambda_{exc}}$

Table AII.1. The average effective photocurrent values and enhancement factors for each substrate with respect to the excitation wavelength.

nm	ITO_{SAM} (nA/cm^2)	AuND/ITO_{SAM} (nA/cm^2)	AgND/ITO_{SAM} (nA/cm^2)	P_{ITO}	P_{AuND}	P_{AgND}	$\frac{P_{AuND}}{P_{ITO}}$	$\frac{P_{AgND}}{P_{ITO}}$
810	10.46	20.5	16.7	10.46	32.36	22.91	3.1	2.19
730	16	28.6	29.2	16	43.4	42.37	2.71	2.64
680	23.5	86	51.5	23.5	159.17	79.43	6.77	3.38
660	20	67.5	72	20	123.3	124	6.16	6.20
565	13	40	120	13	71.63	227	5.51	17.46
470	16.6	27.1	153	16.6	39.4	289.5	2.36	17.37
455	29.6	62.7	192	29.6	101.5	354.6	3.42	11.95
420	24.5	54	110.6	24.5	88.58	196.8	3.61	8.03
395	23	50	28	23	81.88	33.12	3.56	1.44

3. FDTD simulated absorbance spectrum:

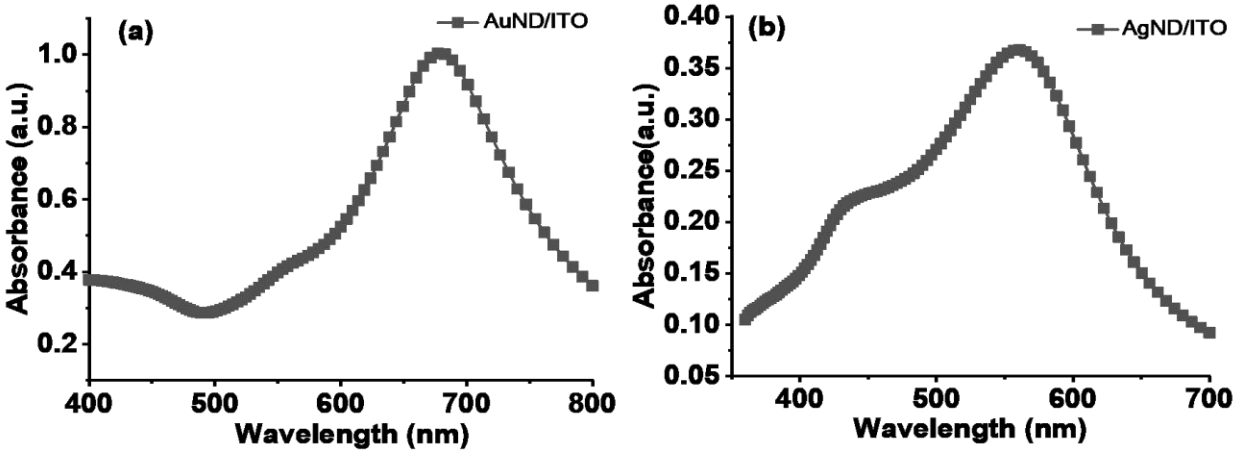

Figure AII.2. (a) FDTD simulated LSPR absorbance spectrm for AuND/ITO in water **(b)** FDTD simulated LSPR absorbance spectrum for AgND/ITO in water. The background refractive index of 1.33 is used to reflect the water sorrounding. The AuND/ITO and AgND/ITO absorbance maximum are located at 677 nm and 561 nm respectively.

Appendix III

Facile Method of PSI-Au Nanoparticle Reconstitution into DPhPG lipid membrane

AIII.1 Materials and Methods:

Materials:

Dibasic (Na_2HPO_4) and monobasic (NaH_2PO_4) sodium phosphate with >99% assays were purchased from Fisher Scientific to prepare the 200 mM Na-Phosphate aqueous buffer solution with pH = 7. All aqueous solutions were prepared using ultrapure de-ionized (D.I.) water with a resistivity of 18.2 MΩ cm at 25 ^{0}C (Millipore, Billerica, MA). Triton X-100 (10 % w/v aqueous solution) surfactant was purchased from Anatrace. 1,2-diphytanoyl-sn-glycero-3-phospho-(1′-rac-glycerol) (DPhPG) was purchased as lyophilized powder from Avanti Polar Lipids, Inc. The average diameter of 5 nm spherical gold nanoparticles functionalized with 4-mercapto-1-butanol suspended in DI water solvent was purchased from Nanopartz (Part # B11-5-4MB-DIH-50-0.25).

Methods:

Growth of T. elongatus and preparation of PSI: The thermophilic cyanobacterium Thermosynechococcus elongatus (T. elongatus) BP-1 was grown and extracted from thylakoids according to previously described methods[27]. The details of the extraction and purification of the trimeric PSI complex from the grown T. elongatus cells are provided elsewhere[158], with few changes mentioned previously[57]. The concentration of PSI trimers in the final stock solution is estimated to be 54.0 x 10^{-6} mol L^{-1}. PSI trimers were stored in aliquots of 100 µl at -80 ^{0}C for future use.

Liposome preparation: First, 4 mg ml^{-1} lipid suspensions were prepared in 200 mM Na-phosphate (pH = 7) buffer. Second, it underwent 3-4 freeze-thaw cycles to form multilamellar liposomes. Third, these suspensions extruded through a 100 nm pore size filter using a NanoSizer Extrusion Kit (T&T Scientific) to form unilamellar vesicles at room temperature. The large

unilamellar vesicle sizes of ~100 nm confirmed via dynamic light scattering (DLS) measurements. Further details regarding the lipid vesicle preparations can be found in previous studies [159].

UV-Visible absorbance and fluorescence: All spectral absorbance and fluorescence data was obtained on BioTek Synergy H1 well plate reader at room temperature.

Negative-staining electron microscopy: Negative staining was used to facilitate electron microscopic imaging by surrounding the biological sample with a thin layer of heavy metal, thereby increasing the contrast of the biological material with its surroundings. A sequential two-droplet method was used for negative staining. An aliquot (~5μl) of the PSI or PSI-AuNP in buffer suspension was allowed to adhere to a thin carbon film supported by a 200-mesh copper grid. Just prior to use the grid with carbon film was glow-discharged for 20 s to render the film hydrophilic. The suspension was incubated for 1 min at room temperature. The excess sample solution was removed by blotting with filter paper touched to the edge of the grid. After removing the excess sample, the grid was stained with 1% (w/v) uranyl acetate (UAC) at pH 3 for 60 s. Excess stain solution was removed by blotting with filter paper touched to the edge of the grid. Then the grid was dried at room temperature. Negatively stained specimens were examined with a Zeiss Libra 200MC TEM.

AIII.2 Results:

As shown in Figure 1, the negative staining with specifically UAC facilitated the contrast to image the individual PSI units with its trimeric form. The uranyless acetate staining was found to be ineffective to stain and image the PSI. The Figure 1(b) shows the individual spherical gold nanoparticles (AuNP) of size ~5 nm in diameter. The purchased AuNP was functionalized with SAM of 4-mercapto-1-butanol. The hydroxyl functional group of the SAM can form hydrogen bonds with PSI units. To reconstitute the PSI-AuNP hybrid system into DPhPG lipid membrane, the AuNP attachment to PSI units is investigated first at varying concentration of AuNP while keeping the detergent and PSI concentration as constant. The detergent solubilized PSI was incubated in the 3 different concentrations of AuNP and the AuNP attachment to PSI is tracked with the TEM images. The detergent in the incubation step is facilitating the disaggregation of high concentrated AuNP in the solution. The AuNP found to be attaching to the rim and flat sides of the disc like structure of PSI. As shown in the Figure AIII.2 the number of AuNP attachment to

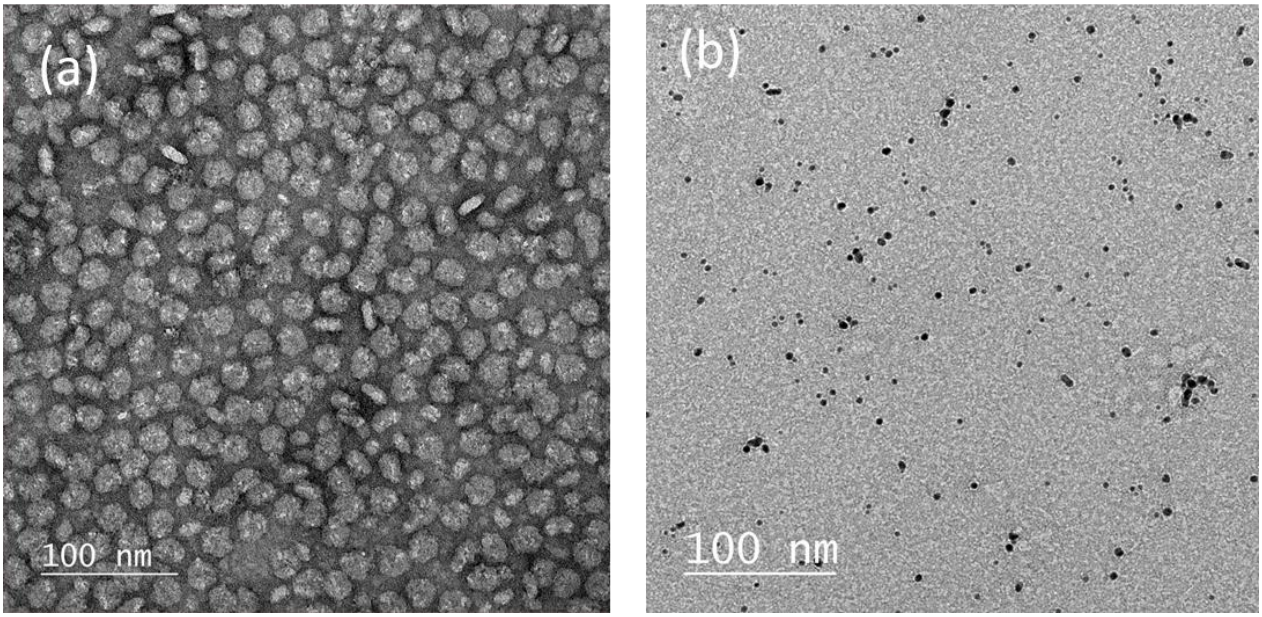

Figure AIII.1 Stained-TEM images of (a) individual PSI units showing its trimeric form, and (b) functionalized gold nanoparticles.

PSI is observed to be increasing with the concentration of AuNP.

To reconstitute the PSI-AuNP into DPhPG lipid membrane the procedure mentioned in the methods section of Chapter 4 by replacing the solubilized PSI solution with PSI-AuNP solution along with few other changes as follows. First, the prototypical non-ionic detergent Triton X-100 (TX-100) was added to preformed DPhPG liposomes (4 mg ml^{-1}) such that the triton concentration in the liposome to be 12mM. The solution was equilibrated for 60 min and mixed with solubilized and centrifuged PSI-AuNP solution containing 4CMC TX-100, 7 mM Na-phosphate buffer (pH 7.0) and 12mM PSI. The centrifugation (at 5000 rpm for 1 min) step was added prior to mix with DPhPG liposome to remove the large size aggregation precipitate. The PSI to AuNP ratio as determined from the Figure AIII.2 (a) was maintained. The concentrations of AuNP mentioned in Figure AIII.2 (b) & (c) could not be maintained due to unavailability of high concentrated AuNP stock solution to start with. The Triton concentration was doubled to accommodate the high concentration of AuNP disaggregation in the solution. Afterward, the mixture was incubated for30 min at room temperature under gentle agitation. For PSI-AuNP reconstitution, TX-100 was slowly

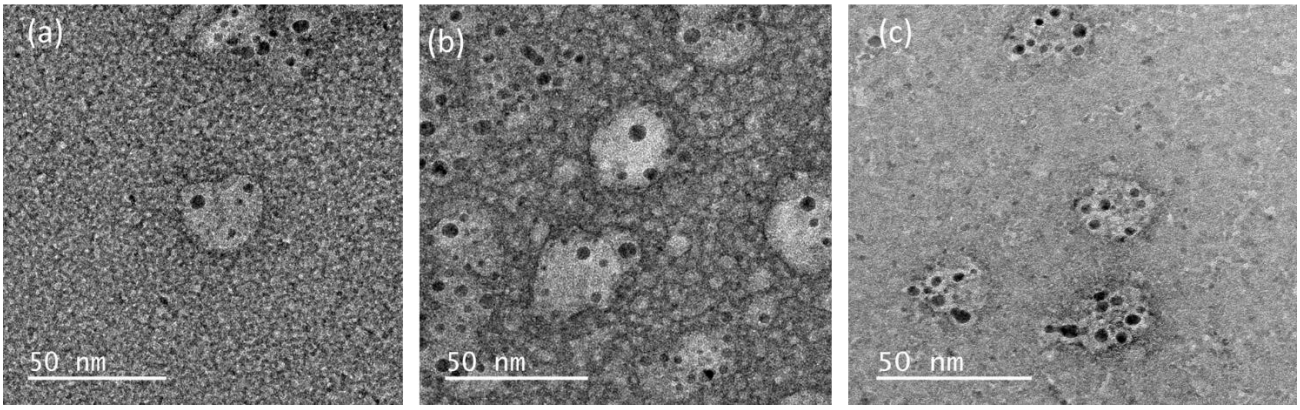

Figure AIII.2 stained-TEM images of PSI-AuNP system with increasing concentrations of AuNP from left to right. The AuNP concentrations used in the incubation process are (a) 0.3174 μM, (b) 0.4232 μM, (c) 0.529 μM while the PSI concentration is kept constant at 0.1325 μM.

removed using bio beads by a three-step procedure. The first step was the addition of 20 mg bio-beads per milligram of TX-100 and incubation for 1 hour at room temperature under gentle agitation. A similar amount of bio beads was added in the second step and incubated for 12 hours at 4 ^{0}C. Finally, another batch of a similar amount of bio-beads was added and incubated for 1 hour at room temperature. Then, the bio beads were removed, and the solution was undergone through centrifugation to extract only PSI-AuNP reconstituted proteoliposomes. Here, the size exclusion was replaced with centrifugation since the size exclusion failed to separate due to the nanoparticle aggregates clogging in the column. First the solution was centrifuged at 5000 rpm for 1 min and collected the supernatant. The supernatant was diluted with 200mM phosphate buffer in 3:7 ratios. In the last step, the solution was further centrifuged at 13300 rpm for 5 min and the supernatant was further tested for absorption and fluorescence spectrum.

The absorption spectra of PSI, AuNP, and PSI-AuNP in Figure AIII.3 shows the distinctive characteristic features. The AuNP has increasing absorbance as the wavelength decreases. It has absorption band centered at ~517 nm. The absorption spectrum for the PSI-AuNP system reflect both PSI and AuNP characteristic features. Interestingly, the absorbance of PSI-AuNP-DPhPG system after the 13300 rpm centrifugation step shows a significant blue shift (~440 nm to 418 nm)

in the blue region of the PSI absorption peak which is similar to blue shift observed in the earlier PSI-DPhPG proteoliposome samples (Figure AIII.3 (b-c)). As shown in the Table AIII.1, there is a 26 nm and 20 nm shift in PSI-DPhPG and PSI-AuNP-DPhPG respectively in comparison with the bare PSI peak position in the blue region. In case of the Chla peak in the red region, a 4 nm blue shift is observed in the PSI-AuNP-DPhPG system. These blue shifts are indicating the successful reconstitution of PSI-AuNP in DPhPG lipids. Furthermore, the spectrum in the green region for PSI-AuNP-DPhPG resembles the green region spectra of PSI-DPhPG.

The fluorescence spectra were investigated for PSI-AuNP-DPhPG solution at 440 nm, 550 nm and 600 nm excitations and compared with PSI-DPhPG (Figure AIII.4). As discussed in chapter 4, the 440nm and 550 nm excitation resulted in blue shifted fluorescence spectra compared

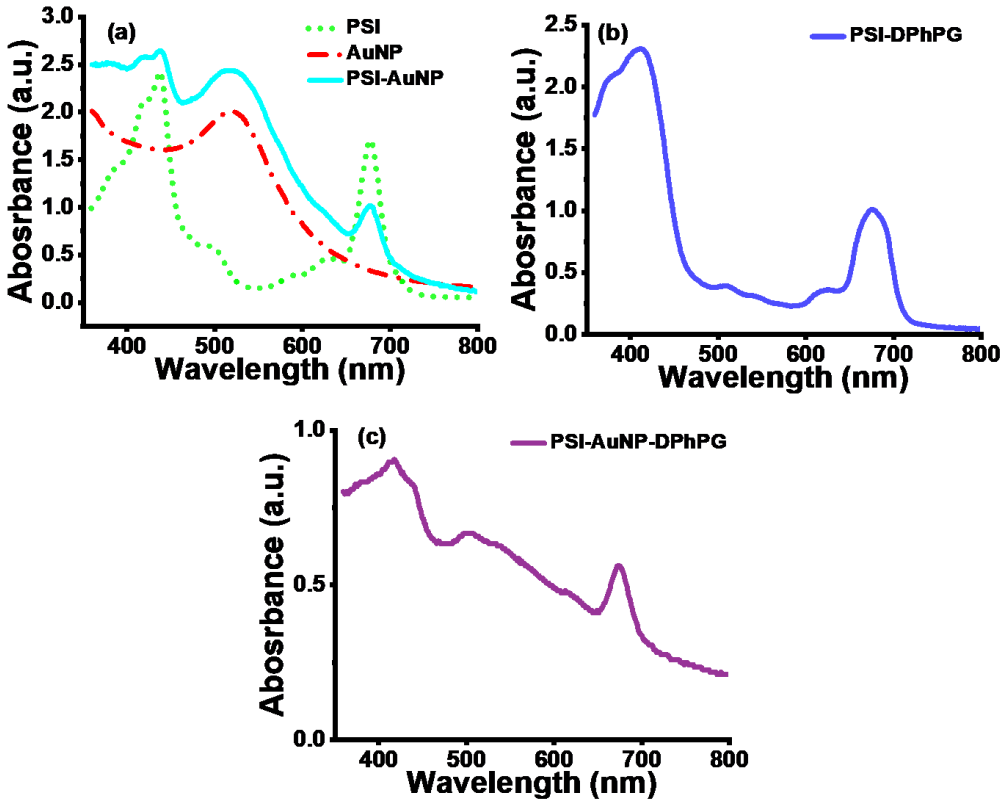

Figure AIII.3 (a) Absorption spectra of PSI (dotted green), AuNP(dash dotted red), PSI-AuNP system (solid cyan), (b) PSI-DPhPG liposome (solid blue) and (c) PSI-AuNP-DPhPG solution (solid purple).

Table AIII.1 Location of the dominant peak positions of Chla in the blue and red region and the shift (Δ) in comparison with the peak positions in bare PSI.

	PSI	PSI-DPhPG	PSI-AuNP-DPhPG
Chla peak position (nm)	439	413 (Δ = 26)	419 (Δ = 20)
	679	678 (Δ = 1)	675 (Δ = 4)

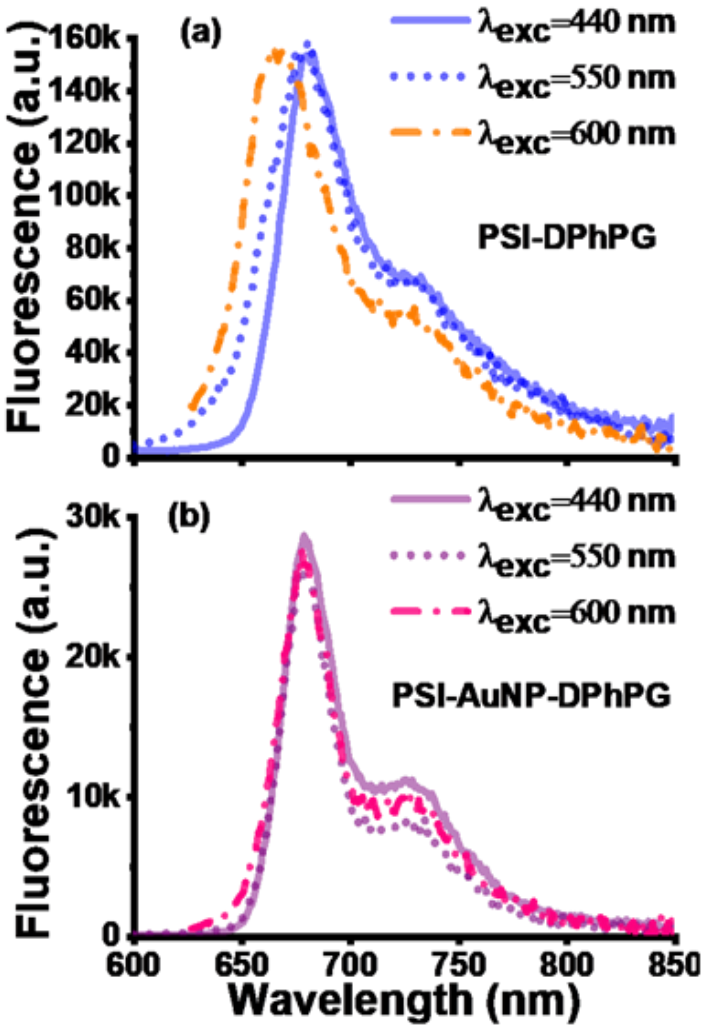

Figure AIII.4 Fluorescence emission spectra obtained for (a) PSI-DPhPG and (b) PSI-AuNP-DPhPG system at the excitation wavelengths of 440 nm (solid), 550 nm (dotted) and 600 nm (dash dotted).

to PSI with an emission peak at 680 nm. Upon increasing the excitation to 600 nm a slight 15 nm blue shift to the 666 nm emission peak is also observed. Similar to the PSI-DPhPG, the characteristic absorption spectra for PSI-AuNP-DPhPG under 440 nm and 500 nm excitations follow the similar blue shifted fluorescence for the emission peak at 680 nm. This is a clear indication of successful reconstitution of PSI-AuNP into the DPhPG lipid membrane. Unlike the PSI-DPhPG at 600 nm excitation, the fluorescence did not deviate from the spectra with 440 nm and 550 nm excitation, indicating unique alterations in emission pathways due to the additional AuNP incorporation into the lipid confinement.

Appendix IV

Qualitative Estimation of PSI in Metal Organic Framework Using Laser Induced Breakdown Spectroscopy

AIV.1 Materials and Methods:

Synthesis of PSI@ZIF-8:

A 50 mM aqueous solution of zinc acetate was prepared by dissolving 0.439 grams of ZnAc in 40 mL of deionized water. Separately, a 2000 mM solution of 2-methylimidazole (Hmim) was prepared by dissolving 6.568 grams of Hmim in 40 mL of deionized water. In a 2 mL microcentrifuge tube, 76.7 µL DI water, 60 µL ZnAc solution, 13.3 µL PSI stock solution, and 150 µL Hmim solution were combined. The final volume was approximately 300 µL with final concentrations being 2.5 µM PSI, 10 mM ZnAc, 1000 mM Hmim. This solution was vortexed for 15 seconds and placed in dark at room temperature for 1 hour. The precipitate was collected by centrifugation at 3000 x g for 5 minutes, then washed and centrifuged in DI water for 3 times.

Synthesis of LiTCNQ

The organic-inorganic salt complex LiTCNQ was prepared using a previously established procedure[171] with slight alterations. A solution of 1000 mL acetonitrile was brought to 80°C under continuous stirring on a hot plate. 100 mL of this was taken out and added to a beaker with 20 grams of LiI. In the remaining 900 mL of the original solution, 10.2 grams of TCNQ was added. Once both solids were completely dissolved, the 100 mL containing 20 grams LiI was added back to the 900 mL containing 10.2 grams TCNQ (the final concentrations were thus 50 mM of TCNQ, 150 mM of LiI), covered, and left stirring at 80°C for 12 hours. The purple precipitate was collected by repeated centrifugation at 5000x g and washed with fresh acetonitrile until the supernatant turned from a bright green to a pale green. The solid was then dried in vacuum and stored in a sealed glass vial.

Conversion of PSI@ZIF-8 into PSI-Zn-H2mim-TCNQ:

A 15 mM aqueous solution of LiTCNQ was prepared by dissolving 0.0317 grams of

LiTCNQ in 10 mL of deionized water, which had been purged with nitrogen gas. A 15 mM aqueous solution of acetic acid was prepared by dissolving 34.35 µL of pure HAc to 40 mL of DI water. After the final centrifugation step of the previously prepared PSI@ZIF-8, 850 µL of LiTCNQ solution was added and vortexed for 1 minute until thoroughly mixed. To this suspension was then added 500 µL of the 15 mM HAc solution which was followed immediately with vortexing for 1 minute. This solution contained approximately 7.5×10^{-4} µmol PSI, 3 µmol ZIF-8, 7.5 µmol HAc, and 12.75 µmol LiTCNQ. After 5 minutes, the precipitate was collected by centrifugation at 3000x g for 5 minutes, then washed and centrifuged in DI water for 3 times. After the final wash, the precipitate was suspended in 1 mL of DI water, and 100 µL was pipetted onto an ITO slide then dried in vacuum for subsequent testing.

LIBS set-up:

Figure AIV.1, illustrates the experimental set-up in this study. The laser-induced plasma is generated on the sample target surface, using a Q-switched Nd-YAG laser, with nominal wavelength 1064 nm operating at maximum 200 mJ/pulse, and a pulse width of 8 ns (Make: Insight Model: 122551-R). The laser, with a repetition rate of 10 Hz, is focused on a 25 mm diameter fused silica lens (focal length = 35 mm). The spot size on the sample is set by the in-built instrument software to 75 µm diameter, which typically creates millimeter-sized plasma. To improve the statistical average of the signal intensity for each analyte of interest, 25 accumulative shots are collected at different spots. The 25 accumulated shots were averaged into one spectrum and used for signal calculations. The samples are placed on glass slide.

To optimize the intensity from the plasma volume, a fiber optic port is mounted at a 45° collection angle and it collects the plasma emissions (Figure AIV.1). The light is transmitted to a Czerny-Turner spectrometer (Make: Andor Technology; Model: Shamrock - SR-303i-A) with 1200 grooves/mm grating (resolution of 0.1 nm at 500 nm) and a nominal dispersion of 2.58 nm/mm. The slit width is fixed at 95 µm for all experiments carried out here, in order to have the optimum spectral line intensity and resolution. The spectrometer is calibrated against Hg emission at 253.65 nm using a mercury lamp (Make: Ocean Optics). A time-gated intensified charge-coupled device (ICCD) detector array (1024 × 1024 CCD) (Make: Andor Technology; Model: DH334T-18U-E3) detects the spectral lines at the spectrometer exit focal plane. In the ICCD camera set-up, the time gating is synchronized with the laser Q-switch through an in-built

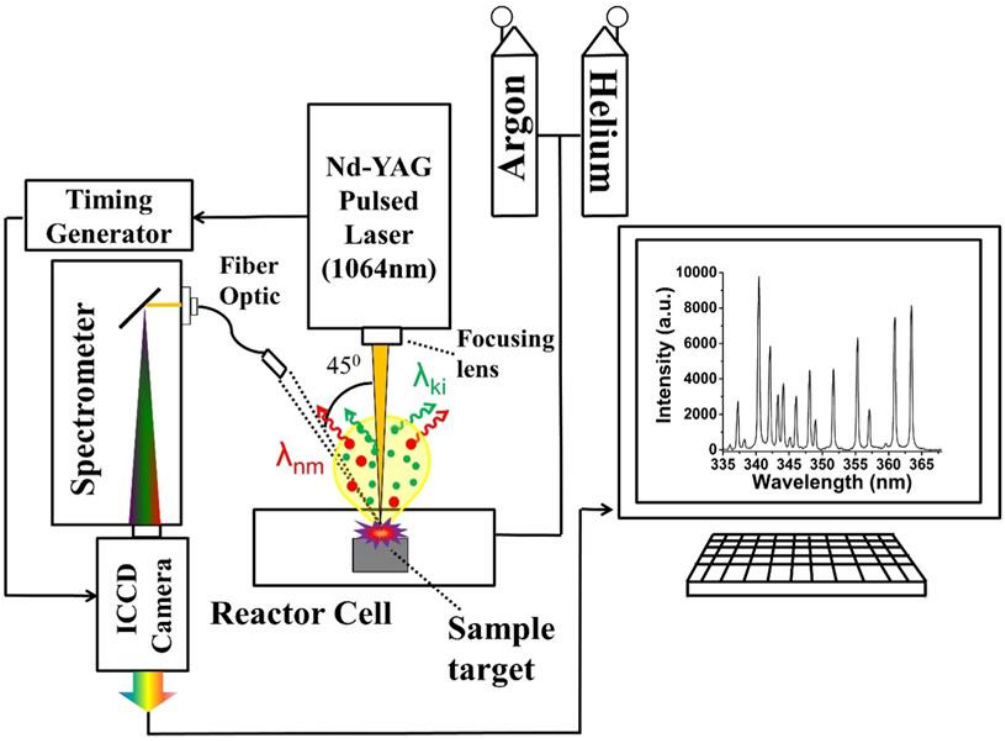

Figure AIV.1 Schematic of LIBS experimental set-up used in this study.

timing generator. The as-prepared lithium battery materials on aluminum foils were placed inside the custom-built chamber. The LIBS shots were taken while the chamber was running with Helium (6.76 lpm) and Argon (2.4 lpm) gases continuously.

AIV.2 Results:

We would expect the ZIF-8 precursor to form stoichiometric amounts of $Zn^{2+}(TCNQ^{-})_2(H_2O)_2$ and $H_2mim^{+}TCNQ^{-}$, the presence of both can best be confirmed by use Laser Induced Breakup Spectroscopy (LIBS) (Figure AIV.2). Based on our earlier LIBS works[172, 173], carbon (C I emission line at 247.86 nm) from 2-methylimidazole and TCNQ, magnesium (Mg I emission line at 285.21 nm) chelated in the porphyrin rings of chlorophyll coordinated in PSI, and finally, zinc (Zn I emission line at 334.50 nm), provides us with 3 strong atomic signature lines that can be systematically evaluated to draw robust qualitative analysis for the complexes formed.

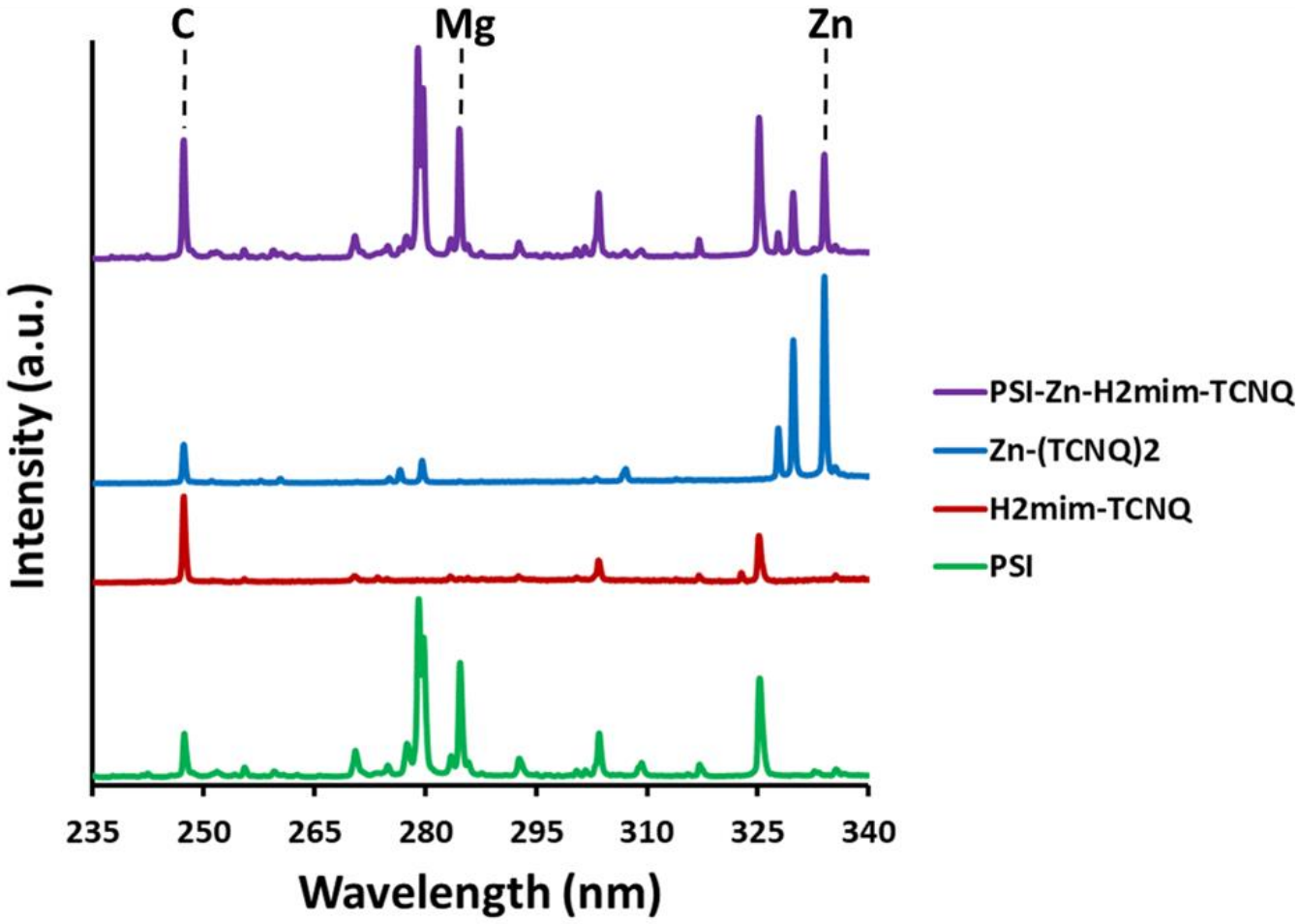

Figure AIV.2 Elemental emissions from laser-induced breakdown spectroscopy. Presence of Mg and Zn signatures confirm both intact chlorophyll and blended TCNQ salts.

Specifically, we can look at the ratios of these background subtracted signals (C:Mg:Zn) in each sample.

Although all four samples contain C, only pure PSI and PSI-Zn-H_2mim-TCNQ can contain Mg. It should be noted that the potential exposure of PSI to significant acetic acid during synthesis could have damaged its structure. The simplest path for this process would involve dechelating the Mg ions from the chlorophyll under acidic conditions, thereby denaturing the PSI and deactivating its absorption and charge transfer properties. However, the consistently high Mg signal from PSI-Zn-H_2mim-TCNQ that is comparable to the emission signals from pure PSI in Figure AIV.2 indicates that very little, if any chlorophyll was dechelated, and the ZIF-8 effectively neutralized all the acid present. Similarly, the presence of both significant Zn signals and highly elevated C signals demonstrate that both the charge transfer complexes ($Zn^{2+}(TCNQ^-)_2(H_2O)_2$ and $H_2mim^+TCNQ^-$) contribute to the blended material. The ratios of the elemental signals in Table AIV.1 affirm the presence of all 3 of the listed materials in the PSI-Zn-H_2mim-TCNQ complex. From these atomic signal ratios and the known elemental compositions of PSI and $Zn^{2+}(TCNQ^-)_2(H_2O)_2$, it can be calculated that the as-formed complex is 41.8% PSI by weight, 42.2% $H_2mim^+TCNQ^-$, and 16.0% $Zn^{2+}(TCNQ^-)_2(H_2O)_2$. These percentages are based on the Mg to C signal ratio in pure PSI and Zn to C signal ratio in pure $Zn^{2+}(TCNQ^-)_2(H_2O)_2$ taken as a reference for estimating the percentage of PSI and $Zn^{2+}(TCNQ^-)_2(H_2O)_2$ in the final PSI-Zn-H_2mim-TCNQ. The molar ratio of imidazole to zinc is therefore 4.3:1, when it should be expected to be 2:1. It may then be assumed that some amount of the zinc complex is lost during the washing procedure, perhaps due to weaker binding with PSI. However, these estimations are in qualitative in nature due to not accounting the matrices effect.

Table AIV.1 The ratios of elemental emission intensities of prepared samples, relative to their carbon emission lines.

Sample material	**LIBS signal ratio (normalized to carbon)**		
	C	**Mg**	**Zn**
PSI	1	2.64	0
$H_2mim^+TCNQ^-$	1	0	0
$Zn^{2+}(TCNQ^-)_2(H_2O)_2$	1	0	5.42
PSI-Zn-H_2mim-TCNQ	1	1.1	0.87

Vita

Ravi Pamu was born in Telangana, India to the parents of Krishnamurthy and Vinoda Pamu. In 2008, He received his bachelor's degree in chemical engineering from Jawaharlal Nehru Technological University, Anantapur, India. In 2010, he received his master's degree in Chemical Engineering from Indian Institute of Technology, Bombay, India. During 2010-2013 he worked as a faculty in Rajiv Gandhi University of Knowledge Technologies, RK Valley, India. Later, he joined research group of Dr. Dibyendu Mukherjee and Dr. Bamin Khomami in 2014 to pursue doctoral degree in Mechanical Engineering. His doctoral research was focused on microenvironmental alterations tuning the photoexcitation pathways of cyanobacterial photosystem I through interfacing with plasmonic nanostructures and lipid membrane that has applications towards photosynthetic protein-based bio-hybrid optoelectronic devices for solar electricity and solar hydrogen production. His doctoral research resulted in 5 published and 3 submitted papers.